

85

LBNL-40763
UC-414



ERNEST ORLANDO LAWRENCE BERKELEY NATIONAL LABORATORY

Measurement of the W and Z Boson Production Cross Sections in $p\bar{p}$ Collisions at $\sqrt{s} = 1.8$ TeV with the D0 Detector

RECEIVED

NOV 06 1997

OSTI

Peter M. Grudberg
Physics Division

January 1997

Ph.D. Thesis

19980528 084

MASTER

DTIC QUALITY INSPECTED 1

DISTRIBUTION OF THIS DOCUMENT IS UNLIMITED

ps

DISCLAIMER

This document was prepared as an account of work sponsored by the United States Government. While this document is believed to contain correct information, neither the United States Government nor any agency thereof, nor The Regents of the University of California, nor any of their employees, makes any warranty, express or implied, or assumes any legal responsibility for the accuracy, completeness, or usefulness of any information, apparatus, product, or process disclosed, or represents that its use would not infringe privately owned rights. Reference herein to any specific commercial product, process, or service by its trade name, trademark, manufacturer, or otherwise, does not necessarily constitute or imply its endorsement, recommendation, or favoring by the United States Government or any agency thereof, or The Regents of the University of California. The views and opinions of authors expressed herein do not necessarily state or reflect those of the United States Government or any agency thereof, or The Regents of the University of California.

Ernest Orlando Lawrence Berkeley National Laboratory
is an equal opportunity employer.

**Measurement of the W and Z Boson Production Cross Sections in $p\bar{p}$
Collisions at $\sqrt{s} = 1.8$ TeV with the D0 Detector¹**

Peter Matthew Grudberg
Ph.D Thesis

Department of Physics
University of California, Berkeley

and

Physics Division
Ernest Orlando Lawrence Berkeley National Laboratory
University of California
Berkeley, CA 94720

Spring 1997

¹This work was supported by the Director, Office of Energy Research, Office of High Energy and Nuclear Physics, Division of High Energy Physics, of the U.S. Department of Energy under Contract DE-AC03-76SF00098.

**Measurement of the W and Z Boson Production
Cross Sections in $p\bar{p}$ Collisions at $\sqrt{s} = 1.8$ TeV
with the DØ Detector.**

by

Peter Matthew Grudberg

B.S. (Yale University) 1984

M.S. (U.C. Berkeley) 1989

A dissertation submitted in partial satisfaction of the
requirements for the degree of

Doctor of Philosophy

in

Physics

in the

GRADUATE DIVISION

of the

UNIVERSITY of CALIFORNIA at BERKELEY

Committee in charge:

Professor Leroy T. Kerth, Cochair

Dr. Stewart C. Loken, Cochair

Professor Kam-Biu Luk

Professor John Rasmussen

Spring 1997

Abstract

Measurement of the W and Z Boson Production Cross Sections in
 $p\bar{p}$ Collisions at $\sqrt{s} = 1.8$ TeV with the DØ Detector.

by

Peter Matthew Grudberg

Doctor of Philosophy in Physics

University of California at Berkeley

Professor Leroy T. Kerth, Cochair

Dr. Stewart C. Loken, Cochair

This thesis reports on the measurement of the W and Z boson inclusive production cross sections (σ_W and σ_Z) times electronic branching ratios ($Br(W \rightarrow e\nu)$ and $Br(Z \rightarrow ee)$) in $p\bar{p}$ collisions at $\sqrt{s} = 1.8$ TeV. The analysis is based on 12.8 pb^{-1} of data taken in the 1992-1993 run by the DØ detector at the Fermilab Tevatron collider; the cross sections were measured to be: $\sigma_W \cdot Br(W \rightarrow e\nu) = 2.36 \pm 0.02 \pm 0.07 \pm 0.13$ nb and $\sigma_Z \cdot Br(Z \rightarrow ee) = 0.218 \pm 0.008 \pm 0.008 \pm 0.012$ nb. The first error is statistical, the second error represents the non-luminosity systematic error, and the third error shows the uncertainty in the luminosity determination. Future prospects for similar measurements based on larger samples of data are discussed.

To Aunt Honor and Grandma Grudberg.

Contents

List of Figures	viii
List of Tables	x
Acknowledgements	xii
1 Introduction and Theory	1
1.1 The Standard Model	2
1.1.1 A Brief History of Weak Interactions	3
1.1.2 Local Gauge Invariance: Quantum Electrodynamics	5
1.1.3 The Electroweak Unification	6
1.1.4 Quantum Chromodynamics	9
1.1.5 Unanswered Questions	11
1.2 W and Z Boson Production and Decay	11
1.2.1 W Boson Production: $p\bar{p} \rightarrow W + X$	12
1.2.2 W Boson Decay: $Br(W \rightarrow e\nu)$	15
1.2.3 Z Boson Production: $p\bar{p} \rightarrow Z + X$	17
1.2.4 Z Boson Decay: $Br(Z \rightarrow ee)$	18
1.3 The Cross Section Measurement	19
2 The Detector	22
2.1 General Overview	22
2.1.1 General Collider Detector Design	22
2.1.2 Tevatron Basics	24
2.1.3 Coordinate System	28
2.2 Central Tracking System	28
2.2.1 Drift Chamber Basics	29
2.2.2 Vertex Detector (VTX)	31
2.2.3 Central Drift Chamber (CDC)	35

2.2.4	Forward Drift Chambers (FDC)	37
2.2.5	Tracking Detector Readout	39
2.3	Calorimeter System	41
2.3.1	Calorimeter Basics	41
2.3.2	Calorimeter Design and Geometry	43
2.3.3	Calorimeter Readout	49
2.3.4	Calorimeter Performance	52
2.4	The DØ Trigger System	52
2.4.1	Level-Ø	53
2.4.2	Level-1 Framework	57
2.4.2.1	Level-1 Calorimeter Trigger	57
2.4.2.2	Main Ring Vetos	60
2.4.3	Level-2	60
2.5	Final Comments	61
3	Event Reconstruction and Particle Identification	62
3.1	Raw Data to Particle Definition: RECO	62
3.1.1	The Raw Data	63
3.1.2	Calibration and Run Condition Monitoring	64
3.1.3	Reconstruction Begins: Vertex Finding	66
3.1.4	Calorimeter Hit-finding	68
3.1.5	\cancel{E}_T Calculation	70
3.1.6	Electron and Photon Definition	71
3.1.7	Tracking in Roads	73
3.1.8	Jet-Finding	75
3.2	Particle Identification	77
3.2.1	Electron identification	77
3.2.1.1	H-matrix chi-squared (χ_{hm}^2)	78
3.2.1.2	Electromagnetic energy fraction (f_{em})	79
3.2.1.3	Track-match significance (S_{trk})	79
3.2.1.4	Isolation fraction (f_{iso})	80
3.2.2	Neutrino Identification (\cancel{E}_T)	81
4	W and Z Data Samples	87
4.1	Event Selection	87
4.1.1	Trigger Requirements	88
4.1.2	Offline Electron Selection	89
4.1.3	W and Z Boson Data Samples	90
4.2	Acceptance	95

4.2.1	Event Generation	96
4.2.2	Detector Response	96
4.2.3	Measured Acceptances and Errors	101
4.3	Efficiency	105
4.3.1	Level- \emptyset Efficiency	105
4.3.2	Electron Selection Efficiency	108
4.3.2.1	Diagnostic Data Sample	108
4.3.2.2	Signal and Background	109
4.3.2.3	Tagging Cuts	110
4.3.2.4	Loose and Tight Selection Efficiencies	112
4.3.3	Overall W and Z Selection Efficiencies	116
4.4	Background	119
4.4.1	Background in the $W \rightarrow e\nu$ Sample	119
4.4.1.1	QCD multi-jet background	120
4.4.1.2	$W \rightarrow \tau\nu$ contamination	124
4.4.1.3	$Z \rightarrow ee$ and $Z \rightarrow \tau\tau$ faking $W \rightarrow e\nu$	125
4.4.2	Background in the $Z \rightarrow ee$ Sample	126
4.4.2.1	QCD Background	126
4.4.2.2	Drell-Yan	131
4.4.2.3	$Z \rightarrow \tau\tau$	133
5	Luminosity	134
5.1	Instantaneous Luminosity	134
5.1.1	Multiple Interaction Correction	135
5.1.2	The Level- \emptyset Monitor Constant $\sigma_{L\emptyset}$	136
5.2	Integrated Luminosity	140
5.2.1	Storing Luminosity Information	141
5.2.2	Live-Time Determination	142
5.2.3	Performing the Integration	145
5.2.4	Alternative: Minimum-bias and Zero-bias events	146
5.3	Luminosity Bookkeeping	147
5.3.1	Production Database	148
5.4	Integrated Luminosity of the Data Samples	149
6	Results and Conclusion	153
6.1	Cross Section Calculations	153
6.1.1	Calculation of $\sigma \cdot Br(p\bar{p} \rightarrow W \rightarrow e\nu)$	153
6.1.2	Calculation of $\sigma \cdot Br(p\bar{p} \rightarrow Z \rightarrow ee)$	156
6.1.3	Statistical Error Calculation	158

6.2	Theoretical Calculations	160
6.3	Cross Section Ratio	167
6.4	Conclusions	168
6.5	Future Prospects	170
Bibliography		174

List of Figures

1.1	W and Z boson production processes.	13
1.2	Parton distributions within the proton at $q^2 = M_W^2$, based on the CTEQ2M structure function.	14
1.3	The $W \rightarrow e\nu$ decay mode.	16
1.4	The $Z \rightarrow ee$ decay mode.	19
2.1	An isometric view of the DØ detector.	25
2.2	A schematic overview of the accelerators used for collider operation at Fermilab.	27
2.3	Plan view of the end of the VTX.	32
2.4	End view ($r - \phi$) of one quadrant of the VTX.	34
2.5	End view ($r - \phi$) of three modules of the CDC.	36
2.6	An isometric view of one FDC chamber, showing two Θ modules surrounding one Φ module.	38
2.7	Schematic view of the unit cell in the liquid argon calorimeter.	44
2.8	Isometric view of the Calorimeter system, identifying the various module types.	45
2.9	Plan view of one quadrant of the calorimetry and central tracking systems, with lines of constant pseudorapidity superimposed.	47
2.10	Diagram showing the distribution of calorimeter cells in depth and rapidity, including the Massless Gaps (MG) and the Inter-Cryostat Detector (ICD).	48
2.11	Schematic block diagram of the DØ trigger and data acquisition systems.	54
2.12	The Level-Ø scintillator array.	56
2.13	A schematic view of the Level-1 trigger framework.	58
3.1	Distribution of the z position of the interaction vertex.	68
3.2	Distributions of residuals between the calorimeter cluster centroid and the projection of the matched Central Detector track.	74

3.3	Distributions of the electron identification variables χ_{hm}^2 , f_{em} , S_{trk} and f_{iso} for a sample of CC electrons with little background.	82
3.4	Distributions of the electron identification variables for a clean sample of EC electrons.	83
3.5	Distributions of the electron identification variables for a sample of CC "electrons" which contains significant background.	84
4.1	Mass plots for the W and Z signal samples.	94
4.2	Distributions of electron p_T and η for the W boson signal sample, compared to the prediction of the fast Monte Carlo.	94
4.3	Distribution of the p_T of the leading electron for the Z boson signal sample, compared to the Monte Carlo prediction.	95
4.4	Level-2 E_T threshold response curves.	100
4.5	\cancel{E}_T spectra for the W signal and QCD background samples.	122
4.6	Electron p_T distribution for $W \rightarrow \tau \rightarrow e$ events	124
4.7	QCD di-jet invariant mass spectrum, with exponential fit superimposed.	128
4.8	The QCD direct photon invariant mass spectrum, with exponential fit superimposed.	128
4.9	Z/γ invariant mass distribution.	129
4.10	Comparison of $Z \rightarrow ee$ data (points) with Monte Carlo plus predicted background.	131
5.1	A schematic diagram illustrating the assumption that $\sigma_{DD}/\sigma_{SD} = \sigma_{SD}/\sigma_{el}$, based on the idea of factorization.	138
6.1	Plot of cross section times branching ratio for inclusive W and Z boson production at $\sqrt{s} = 1.8$ TeV.	165
6.2	Plot of the predicted cross section times branching ratio for inclusive W and Z boson production versus \sqrt{s} , along with the most recent measurements.	166

List of Tables

1.1	Lepton and Quark summary: Electroweak Parameters.	9
1.2	Summary of Z boson decay widths, to first order.	20
2.1	Summary of Central Calorimeter module parameters.	50
2.2	Summary of End-cap Calorimeter module parameters.	50
3.1	Names and typical sizes of the raw data banks for each readout section.	64
3.2	Standard electromagnetic correction factors for each cryostat.	85
4.1	Summary of signal event sample selection and fiducial breakdown.	93
4.2	EM Resolution constant terms and scale correction factors.	97
4.3	Acceptances for W and Z boson events.	101
4.4	Distributions for electrons in $W \rightarrow e\nu$ and $Z \rightarrow ee$ events into the different cryostats	102
4.5	Systematic errors on the W and Z acceptances	102
4.6	Definition of Background Subtraction Prescriptions	111
4.7	Calorimeter electron-identification efficiency: ε_{cal}	114
4.8	Lumped trigger and track-match significance efficiency.	115
4.9	Track-match Efficiency: ε_{match}	116
4.10	Efficiency of tight electron selection cuts.	116
4.11	Overall W electron selection efficiency.	117
4.12	Overall Z electron selection efficiency.	118
4.13	Summary of the W QCD di-jet background calculation.	123
4.14	Summary of the fit results for the $Z \rightarrow ee$ QCD background.	130
5.1	Total elastic, inelastic and single diffractive cross sections at $\sqrt{s} =$ 1.8 TeV.	137
5.2	Double-diffractive cross section calculation.	138
5.3	Level-0 Acceptances.	140
5.4	Calculation of σ_{L0}	140

5.5	Integrated Luminosity Results, using the filter ELE_HIGH	151
6.1	Summary of quantities needed to calculate the $W \rightarrow e\nu$ cross section.	155
6.2	Summary of quantities needed to calculate $Z \rightarrow ee$ cross section.	157
6.3	Calculations of the W and Z boson production cross sections and their ratio for several PDF's.	162
6.4	Calculations of W and Z boson production cross sections and their ratio for values of M_W one standard deviation below and above the world average, using the CTEQ2M PDF.	163
6.5	Calculations of W and Z production cross sections and their ratio for different values of the factorization and renormalization scales.	163
6.6	Summary of estimated errors on the calculated W and Z boson production cross sections and their ratio.	164
6.7	Summary of inputs used to calculate the cross section ratio R	168
6.8	Comparison of the relative errors on the current Run 1A cross section measurement compared with those expected for a 100 pb^{-1} data sample.	171
6.9	Comparison of the relative errors on the current Run 1A measurement of the cross section ratio R with those expected for a 100 pb^{-1} data sample.	172

Acknowledgements

Along the long and sometimes winding path towards the completion of this thesis, I received help from many, many people, and I am grateful. If I tried to list everyone who aided me during my long tenure as a graduate student, these acknowledgements would read like the DØ author list; here, I will offer thanks to those who helped the most. After being here for so many years, I will inevitably forget to mention someone who helped me immensely; I apologize in advance for my oversight.

First, I would like to thank my advisors, Stu Loken and Roy Kerth. I remember when I first talked to Stu about possibly joining DØ, the first thing he promised was that I would have fun. For the most part, that has been true; in fact, some people might say that I had a little bit too much fun, which explains why I have been here for nearly ten years (of course, part of that is Stu's fault; he was instrumental in my becoming interested in cycling). I appreciate the patience shown by both Stu and Roy during my struggle towards completion; I thank them for applying just enough pressure to keep me moving forward. They taught me quite a bit, both about being a physicist and about life in general.

When I joined DØ, I worked on the Vertex Chamber (VTX), which was built here at LBNL (then LBL); as part of that project, I worked with many people, and learned from all of them. I thank Al Clark for the breadth of his knowledge, and for teaching me the value of paying attention to detail. I thank Chris Klopfenstein, who helped get me started, then handed over the reigns when he headed off to Saclay (only to return to DØ two years later with the Stonybrook group). I thank Fred Goozen for his incredible technical prowess, and for always being able to fix whatever I broke. I thank Tom Trippe for getting me started on the VTX software effort (although, in retrospect, maybe he should thank me for taking the VTX software work off of his hands ... just kidding Tom). I thank Ron Madaras for his excellent leadership of the DØ group at LBNL, and for his excellent guidance. I thank Mark Strovink for his physics knowledge, and for his insight into how things really work. I thank Lynn

Stevenson and Orin Dahl for their help along the way.

I would like to specially thank Ed Oltman, who worked harder than anybody to make the VTX run. He and I worked very closely together during the construction, testing and commissioning of the VTX. I will always remember the seven weeks of the test-beam run as some of the toughest in my life; I would not have survived without Ed. I thank Ed for his endless energy and ideas (although I got to dread whenever Ed would say to me "Wouldn't it be nice if ..."); I thank him for teaching me scientific ideals. Most of all, I thank him for being a friend.

I thank Liang-Ping Chen for his help on the VTX, and especially for taking over the software duties, so I could start work towards my physics analysis. I also thank him for his friendship. I thank Danilo Puseljic, Victor Daniel Elvira, Myungyun Pang and Sasha Zinchenko for their help on the VTX. I thank Ian Manning for just plain getting things done during the construction and commissioning of $D\bar{O}$; without him, I doubt $D\bar{O}$ would have been ready on time. I thank Marvin Johnson, Mike Matulik, Mike Utes and Manuel Martin for their help in trying to get the ill-fated VTX cathode pad readout readout working (what cathode pads?); I also thank them for their general technical expertise. I thank Bruno Gobbi for showing me the definition of no-nonsense hard work.

I worked with many people in the process of doing my physics analysis. I got to share the brunt of the workload of the W and Z cross section measurement with Jie Yang, and I thank him. I enjoyed working closely with Hiro Aihara, Tony Spadafora and Natalie Roe here at LBNL, and with Darien Wood, Paul Quintas and Cecilia Gerber at Fermilab. I learned a lot from all of them.

I thank Kam-Biu Luk for making the time to read my thesis, even when he was so busy trying to get his own experiment up and running. I thank John Rasmussen for agreeing at the last minute to read my thesis, and for his encouraging words.

I thank Glenda Fish and Mark Covington for their administrative help here at LBNL. I thank Anne Takizawa and the rest of the gang at the Physics department office for always having the solutions to my problems.

My time at Fermilab was made enjoyable by many friends, including Jim "slow-poke" Cochran, Joey Thompson, Srinu Rajagopalan, Paul Russo, Jaehoon Yu, Scott Snyder, Thorstein Huehn, Paul Rubinov and many others. I thank Roger Dixon for his Sunday morning bicycle rides. I thank Bob Angstadt for being a friend, and for his enthusiasm for cycling.

Many people have made my life here in Berkeley enjoyable. I thank Steve Johnson for his friendship throughout my career here and for sharing my house (putting up with my mess); I thank him in particular for taking even longer to finish than I did. I also thank my other current house-mate Andrew Ryan for his friendship and jokes, as well as my former house-mate Paul Watts for his support and encouragement. I thank Tom Case for his undying enthusiasm. I thank Jeffrey Anderson, Bill Vareka, Bill Kilgore and the rest of my first-year Teaching Assistant colleagues for helping me survive coming back to school. The Cal Cycling Team provided the perfect escape from my work, and kept me in shape. Hilary Price has been the definition of a true friend, and helped me survive my long struggle with my thesis. I thank Cindy Hertzner for her caring and compassion, and for making life fun. I also thank Paul Kwiat, Chad Williams, Sarah Roberts, Shigeki Misawa and Matthew Austern for their friendship.

I would like to specially thank Teri Balser, my soul-mate, for always being there for me. I also thank her for putting up with me while I was finishing my thesis.

Finally, last but definitely not least, I thank my family for their love and support.

Chapter 1

Introduction and Theory

Scientists have always striven to describe the physical world as fundamentally as possible, searching for the one set of indivisible particles that make up all matter. As experiments probed deeper and deeper, many levels of substructure were found: bulk matter is made up of atoms, atoms are made up of a nucleus and surrounding electrons, the nucleus is made up of neutrons and protons, and finally, neutrons and protons are made up of quarks. In our present understanding, all matter is built from two classes of particles, quarks and leptons (electron-like particles); these particles are considered to be fundamental, and there has been no experimental evidence that clearly suggests that there is a further level of substructure.

There are four known forces in nature: gravity, electromagnetism, the strong force and the weak force. All the forces are believed to be based on gauge theories, where the forces operate through the exchange of gauge bosons. Quantum electrodynamics (QED) was developed in the late 1920's [1], brought about largely by Dirac's famous paper on the quantization of the electromagnetic field [2]. The photon is the gauge boson for the electromagnetic force; this theory has proved to reproduce experimental results with unmatched accuracy. The present theory, called the Standard Model, incorporates the strong and weak forces in addition to electromagnetism; gravity is excluded. One of the main features of the Standard Model is that electromagnetism

and the weak force are unified into a single gauge theory. The weak force is carried by a trio of massive gauge bosons, two charged and one neutral. The gauge theory that describes the strong force is called quantum chromodynamics (QCD), in which the force is mediated by an octet of gluons. The discovery of the charged W and neutral Z bosons at CERN in 1983 [3] [4] was very exciting, confirming of the validity of the electroweak theory.

This analysis continues the study of the electroweak theory, based on data taken by the $D\bar{O}$ detector at the Tevatron collider located at the Fermi National Accelerator Laboratory (FNAL or Fermilab). The higher center-of-mass energy and larger integrated luminosities compared to the CERN experiments allowed the collection of much larger W and Z boson samples, which allow precision measurements that test the Standard Model. The cross section measurements described here test the couplings of the weak gauge bosons to both quarks and leptons, as well as probing the quark distributions in the colliding protons and antiprotons. In addition, due to higher order QCD corrections to the production of W and Z bosons, the cross section measurement is sensitive to the quark-gluon coupling as well.

1.1 The Standard Model

The primary goal of particle theory is to develop a simple, unified description of all known forces. The Standard Model is the result of many years of work trying to achieve that goal; it provides a nearly complete theory describing three of the four known fundamental forces based on the principle of local gauge invariance; gravity is excluded, since it is far too weak to affect particle interactions in an appreciable way, and also because there are many technical difficulties presented by the formulation of gravity as a gauge theory. As implied by its name, the Standard Model has proved almost frustratingly successful in describing all observed processes, despite two decades of searching for any indication of a problem with the theory.

A full presentation of the Standard Model is beyond the scope of this thesis;

there are many standard texts that present the material well [5]. Since this analysis concerns the gauge bosons for the weak force, emphasis is placed on the development of weak interaction theory, including a brief history. Electromagnetism and strong interaction theory (QCD) are dealt with briefly. Finally, some questions that remain unanswered by the Standard Model are presented.

1.1.1 A Brief History of Weak Interactions

In order to understand the importance of the study of W and Z gauge bosons, it is instructive to review the history of weak interaction theory and experiment. The first direct experimental observation of a weak decay occurred in 1896, when Henri Becquerel saw evidence for radioactivity in uranium salts [6], while searching for a connection between optical fluorescence and the production of x-rays. In one form of radioactivity, a neutron decays into a proton (or vice versa) within the nucleus and emits a beta particle (an electron or positron). After Becquerel's discovery, a lot of work was done to understand and classify different types of radioactivity, including Marie Curie's landmark work in developing radiochemistry.

In 1914, Chadwick measured a continuous energy spectrum for the beta decay electrons, which was inconsistent with the presumed two-body nature of nuclear beta decay; if energy is conserved, the energy carried off should exactly match the difference in nuclear binding energy between the parent and decay nuclei, which is fixed for a given transition. Furthermore, subsequent calorimetric measurements of beta decay also seemed to defy the conservation of energy. This dilemma was resolved by Pauli, who proposed that beta decay was not a two-body process at all, but rather that there was an additional nearly massless particle produced in the decay, which escapes detection since it reacts at most very weakly with matter. He presented this idea at the Solvay Congress in 1933 [7]; Fermi was in attendance, and was inspired by Pauli's hypothesis.

Fermi developed the first real theory of weak decays [8], in which he used a four

particle point-like interaction to describe neutron decay:

$$n \rightarrow p + e^- + \bar{\nu}_e \quad (1.1)$$

where $\bar{\nu}_e$, an antineutrino, is the extra particle postulated by Pauli. With this three body decay, the continuous energy spectrum of the beta electron is easily understood, as are the calorimetric measurements, since the energy carried off by the neutrino is lost.

As the twentieth century progressed, many new particles were discovered, and new weak interactions were observed. As a result, Fermi's weak Lagrangian had to be expanded. The most important discovery came in 1957, when parity violation was observed in the decay of Cobalt nuclei by Wu *et al.*[9]. Based on this observation and the results of studying several other weak decays, it was established that the weak force only couples to left-handed helicity states. The result of these observations was a generalization of Fermi's theory, named the 'V-A law,' in which the weak force is described by a current-current interaction at a single space point, where the weak current has a polar vector minus axial vector structure ($\gamma_\mu(1 - \gamma_5)$), which picks out the proper left-handed helicity state.

The (V-A) form of Fermi's weak Lagrangian did an excellent job describing all of the observed low energy weak phenomena. However, the theory was known to be flawed, since the calculated matrix elements for several processes violate unitarity at higher energies, even if higher order processes are included. The theory is not renormalizable.

In an attempt to fix the unitarity problems, the point-like interaction of the Fermi theory was modified by the "naïve intermediate boson hypothesis," in which the weak force is mediated by charged bosons, which play a role similar to the photon in quantum electrodynamics. Due to the short range of the weak interactions, these W bosons must be very massive. Unfortunately, though the high energy behavior of the theory was improved, the unitarity problem persisted at sufficiently high energies.

The intermediate vector boson hypothesis was a significant step in the right di-

rection. In time, this piecemeal approach to fixing the problems may have led to a fully renormalizable self-consistent weak interaction theory; however, such an *ad hoc* construction would not carry the same beauty as the current theory, which is cleverly constructed based on the principle of local gauge invariance.

1.1.2 Local Gauge Invariance: Quantum Electrodynamics

In order to gain a basic understanding of local gauge invariance, it is instructive to take quantum electrodynamics as an example. The idea of global gauge invariance is very familiar from electromagnetism, where the vector potential can be modified by the addition of a gradient of a scalar field without affecting the physical fields. Similarly, in QED, the free-particle Lagrangian is invariant under a U(1) rotation of the field operators; this can be related to the conservation of charge using Noether's theorem [10].

For local gauge invariance, the QED Lagrangian must remain unchanged under a position-dependent U(1) rotation:

$$\psi(x) \rightarrow \psi'(x) \equiv e^{i\alpha(x)}\psi(x) \quad (1.2)$$

where $\alpha(x)$ is the phase rotation. Since the free Lagrangian contains a derivative, it is not invariant under such a transformation, due to the non-zero derivative of the phase. However, the invariance can be restored by modifying the derivatives in the Lagrangian:

$$\partial_\mu \rightarrow \mathcal{D}_\mu \equiv \partial_\mu + ieA_\mu \text{ (where } \partial_\mu \equiv \frac{\partial}{\partial x_\mu}) \quad (1.3)$$

where \mathcal{D}_μ is called the covariant derivative, e is the electric charge, and A_μ , the photon field operator, transforms in the following way under the local gauge transformation:

$$A_\mu \rightarrow A'_\mu \equiv A_\mu - (1/e)\partial_\mu\alpha(x) \quad (1.4)$$

When the covariant derivative is substituted into the free Lagrangian, the extra term that results is just the well known QED minimum interaction:

$$\mathcal{L}_I = A_\mu J^\mu \quad (1.5)$$

The form of the basic interaction in QED can be traced directly to the requirement of local gauge invariance; specifically, the force must act through the exchange of the appropriate gauge boson, the photon. This general procedure can be applied to other Lie groups, in order to find the appropriate interaction terms and gauge bosons for other forces.

1.1.3 The Electroweak Unification

A gauge theory combining electromagnetic and weak interactions was first presented by Glashow in 1961 [11]. The finalized electroweak theory was developed independently by Salam [12] and Weinberg [13] in 1967. The Glashow-Salam-Weinberg (GSW) theory is based on the symmetry group $SU(2)_L \times U(1)$, where the L subscript indicates that the weak force only acts on left-handed helicity states, as required by experiment.

The following covariant derivative ensures local gauge invariance with the chosen symmetry:

$$\mathcal{D}_\mu = \partial_\mu + ig\mathbf{T} \cdot \mathbf{W}_\mu + i\frac{g'}{2}YB_\mu \quad (1.6)$$

where \mathbf{W}_μ corresponds to a triplet of gauge fields W_μ^1, W_μ^2 and W_μ^3 corresponding to the $SU(2)$ symmetry, and B_μ corresponds to a single gauge boson corresponding to the $U(1)$ symmetry. The ratio of the strength of the electromagnetic interaction to the strength of the weak interaction defines the Weinberg angle: $\tan \theta_W = g'/g$.

The $SU(2)$ symmetry corresponds to “weak isospin”; the isospin operators T are the well known 2x2 Pauli spin matrices. All left-handed fermions are grouped into weak isospin doublets:

$$\psi = \begin{pmatrix} \nu_e \\ e \end{pmatrix}_L, \begin{pmatrix} \nu_\mu \\ \mu \end{pmatrix}_L, \begin{pmatrix} \nu_\tau \\ \tau \end{pmatrix}_L, \begin{pmatrix} u \\ d' \end{pmatrix}_L, \begin{pmatrix} c \\ s' \end{pmatrix}_L, \begin{pmatrix} t \\ b' \end{pmatrix}_L \quad (1.7)$$

where the primes indicate quark generation mixing. The right-handed helicity states form weak isospin singlets, and do not participate in the weak interaction.

The $U(1)$ symmetry corresponds to “weak hypercharge” Y , and is closely related to the $U(1)$ symmetry of quantum electrodynamics. The electric charge can be related to the weak hypercharge and the third component of the weak isospin by the Gell-Mann–Nishijima relation [14]:

$$Q = T_3 + \frac{Y}{2} \quad (1.8)$$

suggesting that the photon is formed from a combination of the W_μ^3 and B_μ gauge fields.

At this point in the formulation, all the gauge bosons are still massless, which is obviously in violation of experiment. If mass terms are added in by hand, the local gauge invariance is lost, and the theory is no longer renormalizable. One of the essential points of the GSW theory is the method used to give the gauge bosons mass while retaining gauge invariance: spontaneous symmetry breaking and the Higgs mechanism. A complex scalar doublet is introduced, with the corresponding potential such that the vacuum is not the ground state; the symmetry of the vacuum is broken *spontaneously*. The local gauge invariance outlined above is imposed by introducing the $SU(2)_L \times U(1)$ covariant derivatives in the scalar Lagrangian; the result is that three gauge bosons acquire mass terms, while the fourth remains massless. In addition, the Higgs mechanism predicts the existence of a massive neutral scalar particle, the Higgs boson. The Higgs mechanism is also taken to be responsible for the fermion masses, although the mass terms are added in by hand, with one mass parameter for each fermion.

The three massive bosons are the now familiar W^\pm and Z bosons responsible for transmitting the weak force:

$$W_\mu^\pm = \frac{1}{\sqrt{2}}(W_\mu^1 \mp iW_\mu^2) \quad (1.9)$$

$$Z_\mu^0 = (\cos \theta_W W_\mu^3 - \sin \theta_W B_\mu) \quad (1.10)$$

The massless boson is the photon, and is the combination of W_μ^3 and B_μ orthogonal to the Z^0 :

$$A_\mu = (\sin \theta_W W_\mu^3 + \cos \theta_W B_\mu) \quad (1.11)$$

The W and Z masses could be predicted by demanding that the Standard Model reproduce the results based on the Fermi theory; based on the known values of G_F , e and $\sin^2 \theta_W$, the W mass was expected to be roughly $80 \text{ GeV}/c^2$, and the Z boson was expected to be more massive at about $90 \text{ GeV}/c^2$.

The Glashow-Salam-Weinberg theory predicts the existence of neutral weak currents, which had not been observed when the theory was formulated. In 1973, such interactions were finally observed at both CERN [15] and FNAL [16] in neutrino scattering experiments. Furthermore, when the electroweak theory was formulated, only three quarks were thought to exist, and due to Cabibbo mixing [17], there were terms in the Lagrangian coupling the d and s quarks; in order to explain the low observed rate of flavor changing neutral current interactions (such as the decay $K^+ \rightarrow \pi^+ \nu \bar{\nu}$, in which a \bar{s} quark converts into a \bar{d} quark and emits a Z^0), Glashow, Iliopoulos and Maiani [18] predicted the existence of a fourth quark, charm. The first bound state of this quark was first observed in 1974, roughly simultaneously at SLAC [19] and at Brookhaven [20]. Final verification of the GSW theory came in 1983, when the W boson was observed at CERN [3], with the predicted mass. The discovery of the Z boson followed soon thereafter [4].

The question remained as to whether the GSW theory solves the high energy problems inherent to the earlier theories. The answer was yes. The electroweak theory was proved to be renormalizable by 't Hooft in 1971 [21]. One thing to note is that in order for the theory to be anomaly-free, the total electric charge of all particles within a generation must add to zero; this required that each generation have two quarks, one up-type and one down-type, and furthermore, that there be three varieties or *colors* of each quark, an idea which had already been postulated to explain the observed hadron spectroscopy. When the tau lepton was discovered at the Stanford Linear Accelerator Center (SLAC) in 1975 [22], the renormalizability of the theory was threatened, until the discovery of the bottom quark at FNAL [23]; the top quark, bottom's up-type partner, was recently discovered by both FNAL collider experiments [24] [25]. The existence of the third generation had been foreseen by Kabayashi and

Particle	T	T_3	Y	Q
ν_e, ν_μ, ν_τ	1/2	1/2	-1	0
e_L, μ_L, τ_L	1/2	-1/2	-1	-1
e_R, μ_R, τ_R	0	0	-2	-1
u_L, c_L, t_L	1/2	1/2	1/3	2/3
d_L, s_L, b_L	1/2	-1/2	1/3	-1/3
u_R, c_R, t_R	0	0	4/3	2/3
d_R, s_R, b_R	0	0	-2/3	-1/3

Table 1.1: Lepton and Quark summary: Electroweak Parameters. Note that the right handed leptons and quarks do not participate in the weak force, so their weak isospin T is zero; their weak hypercharge Y is determined by the Gell-Mann–Nishijima relation.

Maskawa in 1973 in their study of quark mixing [26], since three generations are necessary to account for the CP violation effects observed in the neutral kaon system. Measurements of the Z boson width at LEP rule out a fourth generation [27], so the quark and lepton spectroscopy is apparently complete; the electroweak properties of the leptons and quarks are summarized in Table 1.1. The only particle remaining to be discovered is the Higgs boson, which has become the focus of the next generation of accelerators and detectors. In summary, the electroweak theory has withstood all experimental tests to date, and counts as one of the premier achievements of theoretical physics.

1.1.4 Quantum Chromodynamics

After the successes of local gauge theories in describing the electromagnetic and weak forces, it was natural to extend the application to the strong force. The current theory of strong interactions, quantum chromodynamics (QCD), is based upon the $SU(3)$ symmetry group, where the symmetry is based upon the three quark colors (hence the ‘chromo’ in the name of the theory). Only quarks participate in strong

interactions, since leptons have no color charge. Local gauge invariance for the $SU(3)$ symmetry requires eight gauge bosons, aptly named gluons. In QCD, the color symmetry is not broken, so the gluons remain massless. QCD is combined with the GSW electroweak theory to form the Standard Model, with an overall gauge symmetry of $SU(3) \times SU(2)_L \times U(1)$.

The main feature that differentiates QCD from the electroweak theory is that the gluons themselves are colored objects, and participate in the strong force. This implies that the color field interacts with itself; that is, the gluons couple to each other as well as to quarks. This has several consequences. First of all, physical particles must be color singlets (no overall color), which explains the absence of free quarks (*quark confinement*), as well as the structure of hadrons: mesons are made of a quark-antiquark color-anticolor pair; baryons (antibaryons) are made up of three quarks (antiquarks), one of each color (anticolor). Next, the gluon-gluon coupling leads to a running strong coupling constant; that is, the coupling strength is strongly dependent on momentum transfer q^2 . At low momentum transfer, the coupling constant is very large and the force is very strong; as q^2 increases, however, the coupling gets continually weaker; this is known as *asymptotic freedom*, since at high enough momentum transfer the quarks behave like free particles.

In general, the agreement between QCD and experiment is excellent, although the comparison is hampered by calculational difficulties. For reactions with little momentum transfer, the coupling is very strong, and perturbation theory cannot be used; difficult and inexact techniques such as gluon resummation must be used instead [28]. At high q^2 , however, the coupling is very weak, and perturbation theory can be used with success; fortunately, the production of W and Z bosons in $p\bar{p}$ collisions falls into this category, so reliable calculations of the production cross sections exist.

1.1.5 Unanswered Questions

Despite the great successes of the Standard Model, there are many issues that are left unanswered. One of the big questions is why there are three generations. Furthermore, the mechanism behind generation mixing is unexplained, although the Cabibbo-Kobayashi-Maskawa matrix provides a phenomenological description [26]. Also included in the CKM matrix is a mechanism for producing CP violation, as observed in the neutral kaon system; the Standard Model provides no real explanation or motivation beyond the mathematical description.

The Higgs boson has not been discovered, so the elegant symmetry breaking mechanism featured in the electroweak theory has not been confirmed. In addition, there is no real explanation of the fermion masses; each mass is inserted by hand into the theory. Why is the top quark so much heavier than the other five quarks?

In the Standard Model, the leptons and quarks are considered to be elementary. With such a large number of elementary particles, it is natural to speculate about the possibility of a further level of substructure; perhaps leptons and quarks are made up of common building blocks. In any case, despite the great success of the Standard Model, the work is far from over.

1.2 W and Z Boson Production and Decay

This experiment measures the product of the W or Z production cross section and the branching ratio for the subsequent decay into the electron channel; experimentally, since only the decay products of the W or Z boson are observed, it is impossible to make separate measurements of the two quantities. In order to make a theoretical prediction to compare to experiment, it is necessary to calculate the production rate and the decay branching ratio separately.

The production mechanism for the weak gauge bosons in $p\bar{p}$ collisions is the weak Drell-Yan process, where a quark and an antiquark annihilate to form an on-shell W

or Z boson, which then decays. Due to the large momentum transfer of the process, the partons within the colliding protons or antiprotons are essentially free, so the spectator model can be used, in which the partons not directly involved in the W or Z boson production subprocess are ignored. The production subprocess is illustrated in Figure 1.1, which shows the lowest order diagrams as well as the next higher order in α_s , in which the produced boson is accompanied by a quark or gluon jet.

1.2.1 W Boson Production: $p\bar{p} \rightarrow W + X$

The subprocess cross section for W^+ production is given by [29]

$$\hat{\sigma}(q\bar{q}' \rightarrow W^+) = 2\pi |V_{q\bar{q}'}|^2 \frac{G_F}{\sqrt{2}} M_W^2 \delta(\hat{s} - M_W^2) \quad (1.12)$$

where q is an up-type quark, \bar{q}' is a down-type antiquark, $V_{q\bar{q}'}$ is the CKM matrix element connecting the two quark flavors, and finally $\hat{s} = (p_q + p_{\bar{q}'})^2$ is the square of the center-of-mass energy of the $q\bar{q}'$ system. The cross section for W^- production is the same, except q is then a down-type quark and \bar{q}' is an up-type antiquark.

In order to obtain the total W production cross section from the subprocess cross section, it is necessary to incorporate the distributions of quarks within the colliding protons and antiprotons. There are two classes of quarks within the proton: the valence quarks (uud in the case of the proton) and the sea quarks, consisting of $q\bar{q}$ pairs that are part of the color field holding the valence quarks together. In addition, roughly half of the proton momentum is carried by the gluons in the color field. The quark and gluon distributions as a function of momentum fraction x at $q^2 = M_W^2$ are shown in Figure 1.2, based on the CTEQ2M structure function[30]. The invariant mass of the subprocess is determined by the W boson mass:

$$\hat{s} = (x_1 p_1 + x_2 p_2)^2 = x_1 x_2 s \equiv M_W^2 \approx 80 \text{ GeV}^2 \quad (1.13)$$

where p_1 and p_2 are the proton and antiproton momenta, respectively, and x_1 and x_2 are the corresponding momentum fractions. At the Tevatron, the center-of-mass

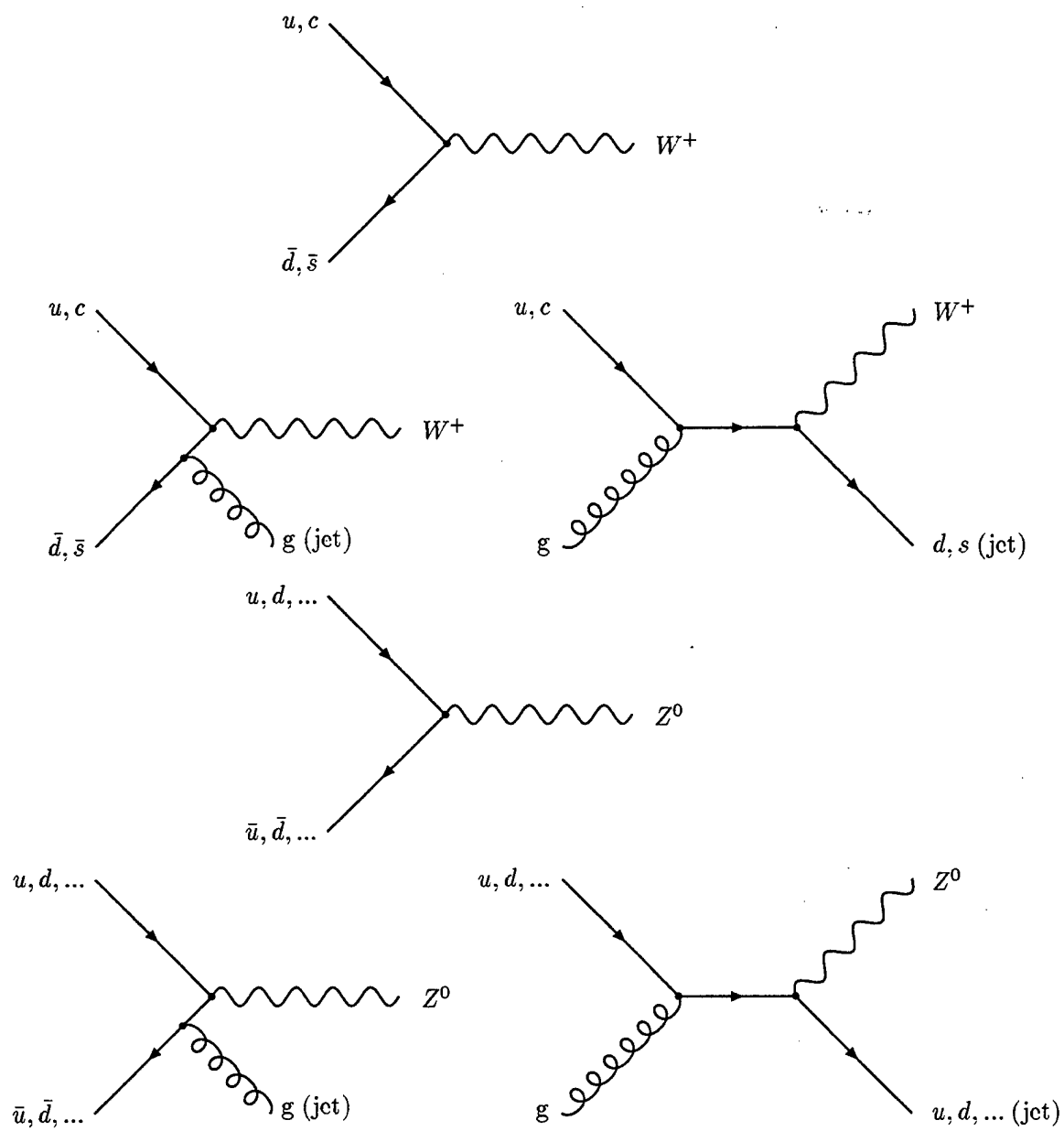


Figure 1.1: W and Z boson production processes

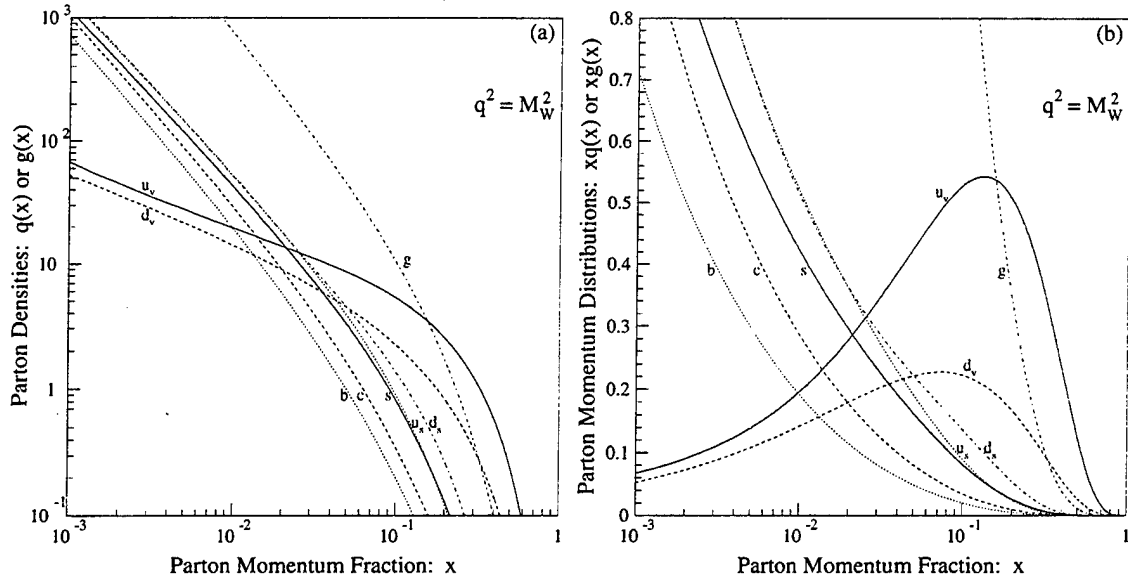


Figure 1.2: Parton distributions within the proton at $q^2 = M_W^2$, based on the CTEQ2M structure function. In Figure (a), the parton densities are shown, where the valence and sea u and d quark distributions are differentiated by a v and s subscript respectively. The normalization is such that $\int_0^1 u_v(x) dx = 2$. Figure (b) shows the momentum distribution for each parton.

energy $\sqrt{s} = 1800$ GeV, so the typical momentum fraction for W boson production is about $x = 0.04$. At such a low x value, the sea quark content of the proton is comparable to the valence quark content, so a significant fraction of the W production cross section comes from collisions involving sea quarks (or even gluons, when higher order processes are included).

The total W boson production cross section can be expressed as follows, where a factor of two has been incorporated to include both W^+ and W^- production, and the factor of $1/3$ comes from the requirement that the quark and antiquark colors cancel to form a colorless W :

$$\sigma(p\bar{p} \rightarrow W + X) = \quad (1.14)$$

$$\frac{2K_W(\alpha_s)}{3} \int_0^1 dx_1 \int_0^1 dx_2 \sum_{(q, \bar{q}')} [q_1(x_1, M_W^2) \bar{q}'_2(x_2, M_W^2) + (q \leftrightarrow \bar{q}')] \hat{\sigma}(q\bar{q}' \rightarrow W^+)$$

where $q(x, M_W^2)$ and $\bar{q}'(x, M_W^2)$ are the quark densities at the specified momentum fraction and scale, the subscripts 1 and 2 refer to the proton and antiproton respectively, and the sum runs over all (q, \bar{q}') pairs that can form a W^+ boson (up-type quark and down-type antiquark). The factor $K_W(\alpha_s)$ incorporates QCD corrections, which have been calculated up to second order by Hamberg, Matsuura and Van Neerven [31]. Note that the antiquark can come from the proton, since the sea quarks play such a large role. The numerical value for the W production cross section will be discussed in detail in Chapter 6, where the experimental results are compared with the theoretical prediction.

1.2.2 W Boson Decay: $Br(W \rightarrow e\nu)$

The $W \rightarrow e\nu$ decay process is illustrated in Figure 1.3. The branching ratio $Br(W \rightarrow e\nu)$ is defined as the ratio of the electronic decay width to the total decay width of the W boson:

$$Br(W \rightarrow e\nu) = \frac{\Gamma(W \rightarrow e\nu)}{\Gamma(W)}. \quad (1.15)$$

The W boson can either decay leptonically into an electron, muon or tau plus the corresponding neutrino, or hadronically into a quark-antiquark pair; the W^+ decays are as follows:

$$\begin{aligned} W^+ &\rightarrow e^+ \nu_e, \mu^+ \nu_\mu, \tau^+ \nu_\tau \\ &\rightarrow u\bar{d}, c\bar{s} \text{ (Cabibbo favored)} \\ &\rightarrow u\bar{s}, c\bar{d} \text{ (Cabibbo suppressed)} \end{aligned} \quad (1.16)$$

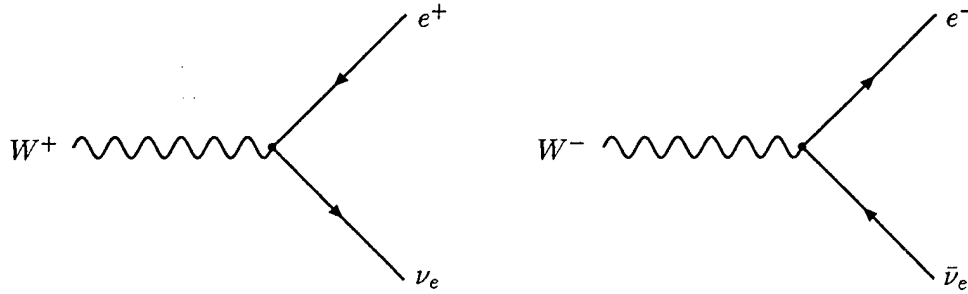


Figure 1.3: The $W \rightarrow e\nu$ decay mode.

The W^- decays are, of course, just the charge conjugates of the above processes. Decays into a top quark are not kinematically allowed, and decays involving the bottom quark have been omitted due to small values of the corresponding elements of the CKM mixing matrix.

To lowest order, the electronic decay width of the W boson is

$$\Gamma(W \rightarrow e\nu) = \frac{G_F M_W^3}{6\pi\sqrt{2}} \equiv \Gamma_W^0 \quad (1.17)$$

where the electron is taken to be massless. The other leptonic decay widths are the same, using the same assumption of massless leptons (the mass corrections are very small, since the lepton masses are much less than the W boson mass). At lowest order, the decay width to a quark-antiquark pair is the same as well, with an additional factor of three to account for the three quark colors, as well as the CKM matrix factor to account for quark generation mixing:

$$\Gamma(W \rightarrow q\bar{q}') = 3|V_{qq'}|^2 \Gamma_W^0 \quad (1.18)$$

Using the Cabibbo model, the total hadronic decay width is $3\Gamma_W^0$ per quark generation, for a total of $6\Gamma_W^0$ since $W \rightarrow t\bar{b}$ is not kinematically allowed. Therefore, to lowest order, the total W boson decay width is $9\Gamma_W^0$, and the electronic branching ratio is simply $1/9$. At higher order, however, the decay widths to quarks and leptons

differ slightly; a more detailed calculation of the W decay rates [32] gives

$$Br(W \rightarrow e\nu) = 0.1084 \pm 0.0002 \quad (1.19)$$

where the error results from the variation of α_s due to the measurement error on the W boson mass.

1.2.3 Z Boson Production: $p\bar{p} \rightarrow Z + X$

The Z boson couples differently to up-type quarks and down-type quarks; the subprocess cross section for Z production in $p\bar{p}$ collisions is [29]

$$\hat{\sigma}(q\bar{q} \rightarrow Z) = \frac{\pi G_F}{\sqrt{2}} (1 - 4|Q_q| \sin^2 \theta_W + 8Q_q^2 \sin^4 \theta_W) M_Z^2 \delta(\hat{s} - M_Z^2) \quad (1.20)$$

where $Q_q = 2/3$ for up-type quarks and $Q_q = -1/3$ for down-type quarks. The total production cross section is obtained by incorporating the parton distribution functions described above; once again, there is a color factor of $1/3$ and a K factor that contains the QCD corrections:

$$\sigma(p\bar{p} \rightarrow Z + X) = \quad (1.21)$$

$$\frac{K_Z(\alpha_s)}{3} \int_0^1 dx_1 \int_0^1 dx_2 \sum_q [q_1(x_1, M_Z^2) \bar{q}_2(x_2, M_Z^2) + (q \leftrightarrow \bar{q})] \hat{\sigma}(q\bar{q} \rightarrow Z)$$

where the variables are as defined above, and the sum runs over all quark flavors. The typical momentum fraction of the partons involved in the Z production is $x = 0.05$, so once again, the sea quarks make a significant contribution, and the antiquark can come either from the proton or the antiproton. The numerical value for the total Z boson production cross section is discussed in Chapter 6.

1.2.4 Z Boson Decay: $Br(Z \rightarrow ee)$

The $Z \rightarrow ee$ decay process is shown in Figure 1.4. The electronic branching ratio of the Z boson is calculated as follows:

$$Br(Z \rightarrow ee) = \frac{\Gamma(Z \rightarrow ee)}{\Gamma(Z)} \quad (1.22)$$

Unlike the case for the W boson, the strength of the coupling to the Z boson (and therefore the decay width itself) depends on the nature of the decay particles. The first order partial decay widths into leptons and quarks are as follows, where the decay products are taken to be massless and the extra factor of three in $\Gamma(Z \rightarrow q\bar{q})$ is a color factor:

$$\Gamma(Z \rightarrow \ell\ell) = 8[(g_V^\ell)^2 + (g_A^\ell)^2]\Gamma_Z^0 \quad (1.23)$$

$$\Gamma(Z \rightarrow q\bar{q}) = 24[(g_V^q)^2 + (g_A^q)^2]\Gamma_Z^0 \quad (1.24)$$

where

$$\Gamma_Z^0 = \frac{G_F M_Z^3}{12\pi\sqrt{2}} \quad (1.25)$$

and g_V and g_A are the vector and axial vector coupling strengths, respectively, which are functions of the weak isospin and electric charge of the fermion:

$$g_V^f = \frac{1}{2}T_3^f - Q^f \sin^2 \theta_W, \quad g_A^f = -\frac{1}{2}T_3^f \quad (1.26)$$

Taking advantage of the fact that $|T_3^f| = 1/2$ for the quarks and leptons that couple to the Z boson,

$$(g_V^f)^2 + (g_A^f)^2 = \frac{1}{8}(1 - 4|Q^f| \sin^2 \theta_W + 8(Q^f)^2 \sin^4 \theta_W) \quad (1.27)$$

Calculation of the partial decay widths for all possible Z boson decays is now straightforward; the results are shown in Table 1.2. Adding up all the possible decays, the total decay width is

$$\Gamma(Z) = \Gamma_Z^0(21 - 40 \sin^2 \theta_W + \frac{160}{3} \sin^4 \theta_W) \quad (1.28)$$

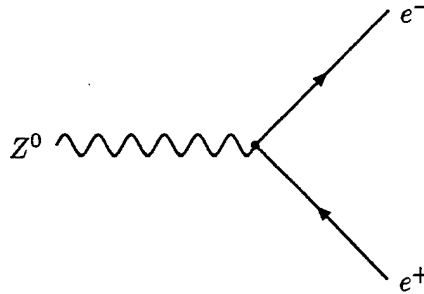


Figure 1.4: The $Z \rightarrow ee$ decay mode.

Using $M_Z = 91.19$ GeV [33], $M_W = 80.23$ GeV [34] and $\sin^2 \theta_W = 1 - M_W^2/M_Z^2 = 0.2259$, the total decay width is $\Gamma(Z) = 2.436$ GeV to first order. The electronic branching ratio is

$$Br(Z \rightarrow ee) = \frac{1 - 4 \sin^2 \theta_W + 8 \sin^4 \theta_W}{21 - 40 \sin^2 \theta_W + \frac{160}{3} \sin^4 \theta_W} = 0.0344 \quad (1.29)$$

Since the higher order corrections for the hadronic decay modes are different than those for the leptonic decays, a more detailed calculation would produce a slightly different value for the branching ratio. However, for this analysis, the LEP precision measurement of $Br(Z \rightarrow \ell\ell)$ [33] is used instead of a higher order calculation when comparing experiment and theoretical prediction:

$$Br(Z \rightarrow \ell\ell)_{LEP} = 0.03367 \pm 0.00006 \quad (1.30)$$

The numerical prediction for $\sigma(p\bar{p} \rightarrow Z) \cdot Br(Z \rightarrow ee)$ is presented in detail in Chapter 6.

1.3 The Cross Section Measurement

The basic principle of the cross section measurement is very simple: just count the number of $W \rightarrow e\nu$ and $Z \rightarrow ee$ events, and divide by the integrated luminosity to get the cross section. This simple statement hides the many details that go into the

Decay	Partial Width ($\Gamma_Z^0 = G_F M_Z^3 / 12\pi\sqrt{2}$)	Value (GeV)
$Z \rightarrow \ell\bar{\ell}; \ell = e, \mu, \tau$	$\Gamma_Z^0(1 - 4\sin^2\theta_W + 8\sin^4\theta_W)$	0.084
$Z \rightarrow \nu_\ell\nu_{\bar{\ell}}; \nu_\ell = \nu_e, \nu_\mu, \nu_\tau$	Γ_Z^0	0.166
$Z \rightarrow U\bar{U}; U = u, c \text{ (not } t)$	$3\Gamma_Z^0(1 - \frac{8}{3}\sin^2\theta_W + \frac{32}{9}\sin^4\theta_W)$	0.288
$Z \rightarrow D\bar{D}; D = d, s, b$	$3\Gamma_Z^0(1 - \frac{4}{3}\sin^2\theta_W + \frac{8}{9}\sin^4\theta_W)$	0.370
Total Width $\Gamma(Z)$	$\Gamma_Z^0(21 - 40\sin^2\theta_W + \frac{160}{3}\sin^4\theta_W)$	2.436

Table 1.2: Summary of Z boson decay widths, to first order. All decay products are assumed massless; the decay $Z \rightarrow t\bar{t}$ is not kinematically allowed, and is not included in the total decay width. The numerical values are based on $M_Z = 91.19$ GeV, $M_W = 80.23$ GeV and $\sin^2\theta_W = 1 - M_W^2/M_Z^2 = 0.2259$.

measurement, such as how the W and Z boson events are identified, the efficiency and acceptance of the selection cuts, and how much background is in the sample; each of these points require detailed analysis. In addition, the measurement of the integrated luminosity involves further detailed analysis.

Despite the relatively small branching ratio, the electronic decay modes provide the best signature for identifying W and Z bosons. Requiring two high transverse momentum leptons (either two electrons for the Z , or one electron and a neutrino for the W , where the neutrino is identified by an imbalance in the transverse energy) keeps the background at a very low level; the hadronic decay modes, on the other hand, despite the large branching ratio, are nearly impossible to separate from the background. Selecting $W \rightarrow e\nu$ and $Z \rightarrow ee$ events takes advantage of the excellent electron identification provided by the DØ detector, as well as the good missing transverse energy resolution due to the compact design of the calorimetry.

Once the raw number of signal events has been determined, the background contamination must then be determined and subtracted from the total, giving the estimated number of real W or Z events in the sample. This number is then corrected for the selection efficiencies and the kinematic and fiducial acceptances to get the total number of $W \rightarrow e\nu$ and $Z \rightarrow ee$ events produced during all active data collection.

To convert the number of W or Z events to a cross section, it is necessary to know the integrated luminosity for the active data-taking. The luminosity is measured using two sets of counters mounted in either endcap region of the detector; all events used in this analysis require both counter arrays to fire in coincidence. The coincidence rate is directly proportional to the instantaneous luminosity (with small corrections at high luminosity for crossings with multiple interactions), so the total number of coincidences in the physics sample, combined with the total $p\bar{p}$ cross section seen by the counters, gives a measure of the total integrated luminosity.

All the details of the cross section analysis are given in the chapters which follow. Chapter 2 describes the DØ detector, which makes the measurement possible. Chapter 3 describes the data reconstruction, which decodes the raw detector data to find physics objects, like electrons and jets. The selection of W and Z events is described in Chapter 4, along with the associated measurements of the acceptance, selection efficiency and background. Chapter 5 presents the details of determining the integrated luminosity. Finally, the cross section results are given in Chapter 6, and compared with theoretical predictions.

Chapter 2

The Detector

A thorough understanding of the detector is necessary in order to do any physics with the data collected at DØ. The DØ detector is a very large, complex system, made up of a large number of sub-detectors which work together to provide an electronic “picture” of the interesting $p\bar{p}$ collisions that occur deep within the apparatus. This chapter presents sufficient detail to understand the analysis presented in subsequent chapters; a more complete description can be found elsewhere [35].

2.1 General Overview

Before getting into the details of the DØ detector, it is instructive to look at the principles that guide the basic design of collider detectors. In addition, a brief overview of the Tevatron accelerator is presented. Finally, there is a description of the coordinate system used to define position within the DØ detector.

2.1.1 General Collider Detector Design

Because of the enormous expense of large-scale collider detectors, they are designed to be general purpose, covering as wide a range of physics topics as possible, instead of being optimized for a single physics search. There is no one detector system that

is capable of fully measuring the wide range of particles produced by the high energy $p\bar{p}$ collisions; instead, several detector subsystems work together to characterize an event.

The design goals are driven by the types of physics to be studied. The collider detectors built to date have concentrated on four basic areas: electroweak physics, heavy quark physics, QCD, and new physics ("beyond the Standard Model"). For such studies, it is necessary to have good particle identification – high transverse momentum leptons for electroweak physics and top searches, soft lepton identification to tag b quark decays within jets, jet identification and reconstruction for QCD physics and top quark mass measurements, and finally identification of non-interacting particles (neutrinos) by measuring an imbalance in the transverse energy for electroweak and top quark physics, as well as for new physics.

Although there is quite a bit of variation between the hadron collider detectors built to date, they are all built within a similar basic theme. The various detector subsystems are nested about the central interaction point. Charged-particle tracking systems are located as close to the interaction point as possible, in order to minimize multiple scattering as well as to maximize the precision for finding the event vertex (or vertices). Often (but not always!), there is a central magnetic field to allow for momentum measurement by measuring curvature of the charged-particle tracks. The calorimetry (or energy measuring) systems are typically located right outside the tracking volume, so that there is as little material in front of them as possible, to minimize particle conversions before they can be measured. The calorimeters cover as much of the solid angle as possible, so as to miss as little energy as possible; in addition, they are designed to incorporate as much material as possible, so that all the energy is contained (and therefore measured). Finally, the muon systems are typically located outside of the calorimeter, taking advantage of the large mass of the calorimeter to filter out all particles but the highly penetrating muons.

The DØ detector follows the general design outlined above. There is no central magnetic field, which allows for a very compact, relatively simple central tracking sys-

tem. Surrounding the tracking, there is a massive, uranium-liquid argon calorimeter, contained in three cryostats. Since there is no central magnetic field (and therefore no magnet), the calorimeter is very compact, minimizing the number of cracks and uninstrumented volume. Finally, outside the calorimeter cryostats, the muon system consists of three measuring planes, with a toroidal magnet between the first and second plane to allow for momentum measurement and charge determination. The parts of the detector used for this analysis are described in more detail in the following sections; notable omissions are the Muon System and the Transition Radiation Detector (part of the Central Detector). An isometric view of the DØ detector is shown in Figure 2.1.

2.1.2 Tevatron Basics

Production of high energy collisions at the center of the collider detectors at FNAL is a very complicated process, involving several different accelerators. A good overview of the Tevatron collider operation can be found elsewhere [36]; only the bare basics are presented here.

The Tevatron itself is at present the highest-energy collider in the world, producing $p\bar{p}$ collisions at a center of mass energy of 1.8 TeV (a 2.0 TeV center of mass energy has been achieved during accelerator testing, but has not been used for any physics running). The Tevatron is a synchrotron based on powerful superconducting magnets, built in a circular tunnel with a radius of approximately 1 kilometer. It was originally used as a source of fixed-target proton beams in 1983, with the first collider engineering run coming in 1985 after the antiproton source was completed. This analysis is based on Run 1A, which lasted roughly a year, starting in May, 1992.

A series of accelerators is used to bring the protons and antiprotons up to the their final energy of nearly 1 TeV; see Figure 2.2 for an overview of the Fermilab accelerators. Negative hydrogen ions are accelerated through a 750 kV potential by an electrostatic column powered by a Cockroft-Walton generator, and then injected

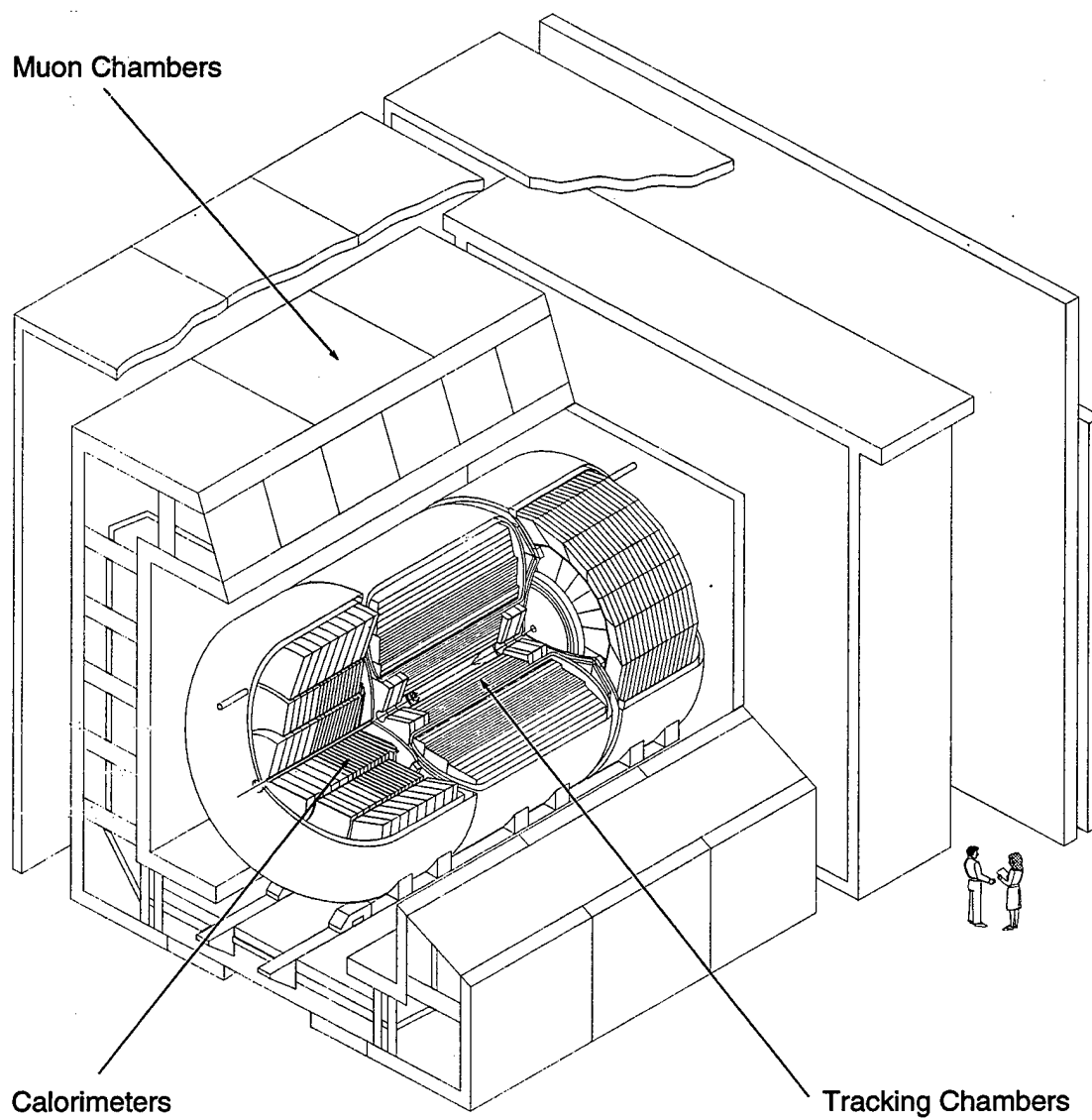


Figure 2.1: An isometric view of the DØ detector.

into the Linac, where they are accelerated to 200 MeV by a series of radio-frequency (RF) cavities, and injected into the Booster synchrotron. The electrons are stripped from the hydrogen ions as part of the injection process, and the bare protons are accelerated to 8 GeV, then injected into the Main Ring.

The Main Ring shares the main tunnel with the Tevatron; it was originally used as a source of 400 GeV protons for fixed-target experiments. For collider operation, it serves two basic purposes. Most of the time, the Main Ring is used as a source of 120 GeV protons for use in antiproton production. In addition, the Main Ring is used to accelerate protons or antiprotons to 150 GeV, prior to injection into the Tevatron.

In order to maximize the potential luminosity, antiprotons are produced nearly all of the time, even during physics running. Protons are accelerated to 120 GeV by the Main Ring, then extracted onto a nickel target. Antiprotons with an energy of 8 GeV are collected from the collision debris and steered into the Debuncher, which is a roughly triangular storage ring adjacent to the Tevatron tunnel. In the Debuncher, the antiprotons are cooled to minimize the momentum spread and the beam size, and the Main Ring bunch structure is removed, so that the antiprotons are in one long bunch, with a small gap to ease extraction. The antiprotons are then extracted into the Accumulator, another storage ring, that shares the tunnel with the Debuncher. The antiprotons are stored in the accumulator until they are needed for injection into the Tevatron; while being stored, additional beam cooling is applied, so as to maximize extraction efficiency.

When a sufficient number of antiprotons have been accumulated, a Tevatron store can be initiated. During collider operation, the Tevatron operates with six proton bunches and six antiproton bunches. To fill the Tevatron, the proton bunches are injected one by one from the Main Ring into the Tevatron at an energy of 150 GeV; then six antiproton bunches are extracted one at a time from the Accumulator into the Main Ring, accelerated to 150 GeV, and then injected into the Tevatron. For Run 1A, each proton bunch contained about 100×10^9 particles, while the antiproton bunches were smaller, with roughly 50×10^9 particles. The bunch length was 50 cm.

Once all the bunches are injected, the energy of the protons and antiprotons is ramped to the operating energy of 900 GeV. Finally, to maximize the luminosity, special low-beta quadrupoles are energized at the two interaction regions to squeeze the lateral beam size to roughly $40\text{ }\mu\text{m}$. At this point, physics data can be taken; during the store, proton and antiproton bunches cross within the DØ detector roughly every $3.5\text{ }\mu\text{sec}$. Barring problems, the store luminosity decays very slowly, typically lasting ten hours or more, during which time the Main Ring is in use making antiprotons for the next store. During Run 1A, when the Tevatron was running at its best, an integrated luminosity of roughly 1 pb^{-1} was delivered to the detectors in one week.

2.1.3 Coordinate System

DØ uses a right handed coordinate system, where the positive z direction is defined by the proton rotation direction (clockwise), the positive x direction points horizontally outward from the center of the ring, and positive y is straight up. Typical definitions for azimuthal and polar angles are used: $\phi = 0$ points along the x -axis, and $\theta = 0$ points in the positive z direction. Instead of using θ to describe a direction within the detector, however, a variable called pseudorapidity (η) is used instead:

$$\eta = -\ln\left(\tan\frac{\theta}{2}\right) \quad (2.1)$$

The benefit of using η to describe the polar angle is that the differential cross section distribution $\partial\sigma/\partial\eta$ is approximately Lorentz invariant, as long as the mass of the system under study is small.

2.2 Central Tracking System

The DØ central tracking system consists of four drift chambers to track charged particles, as well as a transition radiation detector to aid in electron identification. Since there is no central magnetic field and the tracking is not used for momentum

determination (which benefits from a long lever arm), the system can be very compact. In the absence of a magnetic field, the tracks are straight (except for multiple scattering), which eases the job of finding and fitting tracks; track multiplicity can be a problem, however, since low momentum tracks are not swept away by a magnetic field.

There are two drift chambers covering the central rapidity region; the Vertex Chamber (VTX) immediately surrounds the Beryllium beam-pipe, and the Central Drift Chamber (CDC) is located just inside the central calorimeter cryostat. On either end of the central detector volume, Forward Drift Chambers (FDCs) perform the tracking for the forward and backward regions surrounding the beam-pipe. The gap between the VTX and the CDC is filled by the Transition Radiation Detector (TRD), which is not used in this analysis.

2.2.1 Drift Chamber Basics

The standard reference for drift chamber operation is an excellent review article by Sauli [37]; only the basics are presented here. Despite differences in detail, all of the DØ drift chambers work on the same fundamental principles.

The active volume of a drift chamber is filled with gas; the choice of gas plays an important role in the performance of the detector. As a charged particle moves through the drift chamber gas, it creates electron-ion pairs via Coulomb interactions. The number of ionizations depends on the type of gas; for typical drift chamber gases at atmospheric pressure, roughly 100 electron-ion pairs per cm of particle track length are produced. In addition, the amount of ionization depends quadratically on the charge of the traversing particle, so a particle with charge $2e$ would create four times the ionization of a singly-charged particle. More relevantly, two colinear particles each with an absolute charge e would create twice the ionization; this can be used to indicate possible photon to electron pair conversions.

After the electron-ion pairs are created, the electrons are drifted in an electric field

to a set of anode or sense wires. The sense wires are very fine, with typical diameters of 20 to 25 μm ; the electric field surrounding these wires is very strong, causing an avalanche of ionization when the drifted electrons reach the anodes, resulting in a very high gas gain and a clearly detectable signal induced on the wire.

The position of the particle track in the chamber is determined by measuring the drift time of the ionized electron to the sense wire (the difference between the time the particle traversed the chamber and the time the electron reached the sense wire), and converting that time to a drift distance. The time to distance relation depends on both the electrostatic configuration of the chamber (that is, the strength of the electric field as a function of position), and the type of gas used in the chamber. For DØ, the chamber geometry and gas choice was constrained by the 3.5 μsec time interval between bunch crossings; to reliably reconstruct an event, all of the ionized electrons must drift to the sense wires before the next beam crossing.

The drift field itself is created by applying appropriate voltages to a set of electrode wires or strips. The field shaping wires are much thicker than the sense wires, so the surrounding field is not high enough to cause amplification. Of particular importance are the field shaping wires near the anodes, which help focus the field lines onto the sense wires, as well as minimizing cross-talk between adjacent anodes. The electric field in the sensitive volume is made as uniform as possible, to minimize the variation of the drift velocity.

The choice of gas has a large effect on the performance of a drift chamber. In order for the drift chamber to work at all, the gas must not contain any highly electronegative components, or else the ionized electrons would quickly be recaptured before reaching the anode. Most drift chamber gases operate in *saturated* mode, in which the electron drift velocity is largely independent of electric field strength. Typical drift velocities for saturated drift chamber gases at atmospheric pressure range from about 10 to 50 $\mu\text{m}/\text{ns}$. However, some drift chambers, like the VTX, operate using an *unsaturated* gas, in which the drift velocity is roughly directly proportional to the electric field strength. The benefit of this approach is that lower drift velocities and

lower gas diffusion is possible, allowing for better position resolution (the position resolution is primarily determined by the drift time resolution; for a fixed time resolution, the position resolution is better for smaller drift velocities). There are several disadvantages, however. Since the drift velocity depends on the field strength, it is sensitive to any irregularities in the field. Due primarily to the details of the field shape immediately surrounding the sense wires, the time to distance conversion is not purely linear, and usually must be determined empirically. In addition, there can be a fairly large variation in drift time from a given particle track to a given sense wire, depending on where in the sense wire cell the ionization occurs; this can lead to broader pulses, and potentially degrade the two track resolution of the chamber. All in all, the choice of gas is one of the most critical design decisions involved in building a drift chamber. The design specifics for all of the DØ drift chambers are described briefly below.

2.2.2 Vertex Detector (VTX)

The Vertex Detector [38] is the innermost tracking detector, immediately surrounding the Beryllium beam-pipe, extending from an inner radius of about 3 cm to an outer radius of nearly 17 cm. The chamber is separated into three mechanically independent layers, each built on a thin carbon fiber tube which defines the inner radius of that layer. The sense and field shaping wires are strung between G-10 bulkheads; another G-10 bulkhead outside the wire bulkheads forms the gas seal. Titanium tie-rods between the bulkheads transfer the wire tension from the wire bulkhead to the inner radius of the gas bulkhead (and ultimately to the carbon fiber tube). The high voltage distribution system occupies the volume between the bulkheads; the signal preamplifiers are mounted outside the gas bulkhead, but inside the end-plate of the detector. The three layers of the VTX are concentric and mounted one inside the other; the outer wall of the gas volume for a given layer is defined by the inner surface of the carbon fiber tube of the next layer outward. A fourth tube is used to enclose

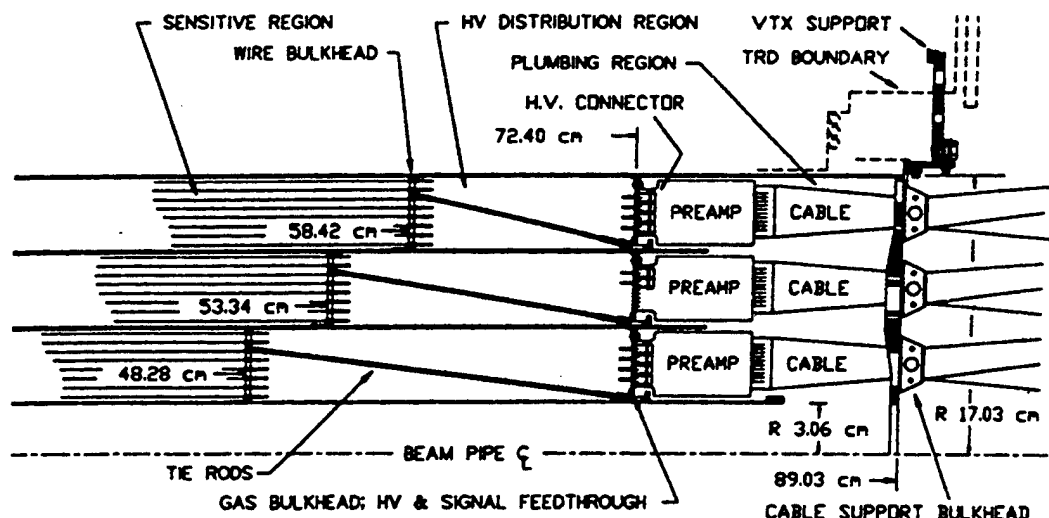


Figure 2.3: Plan view of the end of the VTX, showing the arrangement of the bulkheads separating the active region, the high voltage distribution region, and the plumbing/readout electronics region.

the outermost layer, and defines the outer surface of the entire VTX detector. The active volume for the innermost layer (layer 0) is roughly 97 cm long, positioned symmetrically around the nominal interaction at $z = 0$; the active volume lengths of layers 1 and 2 are roughly 107 cm and 117 cm respectively. A plan view of the VTX is shown in Figure 2.3.

The VTX uses a jet cell geometry for the drift cells, in which the sense wires are arranged in planes parallel to the trajectories of particles coming from the interaction vertex, and the drift direction is azimuthal (so that measuring the drift distance measures the particle track azimuth). The VTX layers are split into individual cells, distributed azimuthally; layer 0 has 16 sectors, while the outer two layers each have 32 sectors. Each sector has eight sense wires; a track passing through all three layers could therefore result in 24 position measurements. The sense wires are staggered

by $\pm 100 \mu\text{m}$ within the cell, to help in resolving the left-right ambiguity (the sense wires are in the middle of the cell; electrons can drift in from either direction). In addition, the sense planes are staggered between layers, to further resolve the left-right ambiguity, as well as to minimize the overlap of the low performance regions surrounding the cathode and sense planes. The sense wires are $25 \mu\text{m}$ NiCoTin [39]. NiCoTin is resistive, with a resistivity of $1.8 \text{ k}\Omega/\text{m}$; signals from both ends of the wires are read out, and the z coordinate of each hit is determined using charge division. The sense wires are operated at positive high voltage; there is a plane of grid wires at ground on either side of the sense plane, which help focus the field lines onto the sense wires. The drift field is created by fine field wires at the inner and outer boundaries of the cell, as well as by a plane of cathode wires which form the boundary between adjacent cells. The grid, fine field and cathode wires are all $152 \mu\text{m}$ gold-plated aluminum. Additional coarse field shaping is provided by aluminum traces on kapton sheets that are laminated to the inner and outer surfaces of the carbon fiber tubes. The layout of the VTX drift cells can be seen in Figure 2.4.

The gas used in the VTX is a mixture of CO_2 (95 %) and ethane (5 %), with a small admixture of water vapor which helps control discharge. As mentioned above, the gas is run in unsaturated mode, allowing very good spatial resolution and pulse-pair separation. The drift velocity in the VTX was about $7.3 \mu\text{m}/\text{ns}$, corresponding to a drift field of roughly $1 \text{ kV}/\text{cm}$. Since the drift velocity varies with field strength, care was taken to determine the proper time to distance relation, which was based on test beam data [40], and corrected for environmental effects (variations in pressure and temperature) based on studies using data from a test cell (the VTX canary) which monitored the gas quality. The gas gain was roughly 4×10^4 ; the pulse amplitudes were also corrected for environmental effects.

Due to the low drift velocity in the unsaturated gas, the spatial resolution in the drift direction is very good, ranging from about $40 \mu\text{m}$ to $60 \mu\text{m}$ for hits in the bulk drift region of the chamber (the resolution degrades in the regions surrounding the anode and cathode wires, where the electric field strength varies rapidly). The hit-

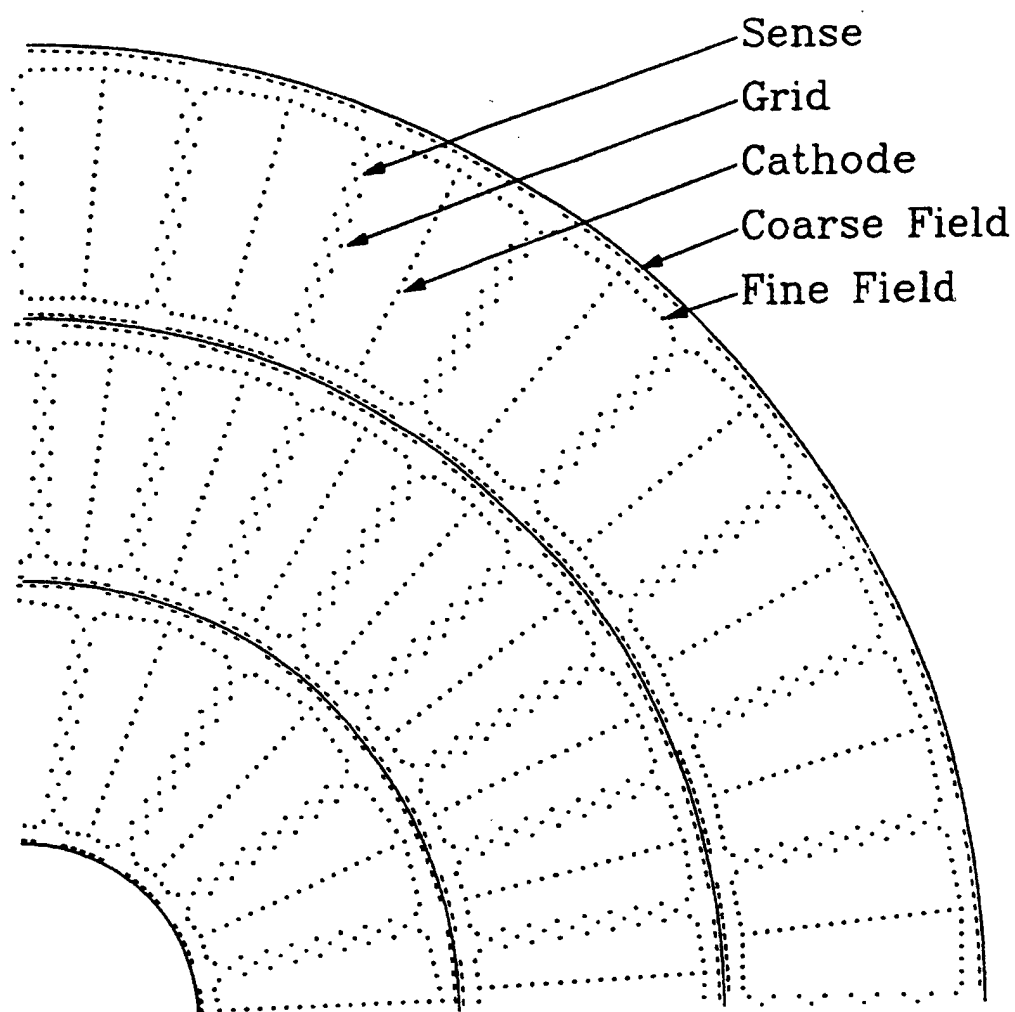


Figure 2.4: End view ($r-\phi$) of one quadrant of the VTX, showing the arrangement of the sense wires and field shaping electrodes.

finding efficiency is about 98 % at the chosen gas gain. Pulse pair resolution is also very good; based on off-line superposition of test beam data, two hits separated by 630 nm (in the drift direction) can be resolved with 90 % efficiency. The spatial resolution along the VTX wires for isolated hits is about 1.5 cm; unfortunately, the high occupancy in the VTX causes a lot of overlapping hits, and the z determination using charge division suffers, both in resolution and in efficiency (many hits are measured well in $r - \phi$ but have no z information). As a result, the three dimensional tracking efficiency is very low, and few Central Detector tracks incorporate VTX information.

2.2.3 Central Drift Chamber (CDC)

The Central Drift Chamber [41] performs the bulk of the tracking duties in the central region of the detector. It is located just inside the inner surface of the central calorimeter, extending in radius from roughly 50 cm to 75 cm. The CDC is 180 cm long, centered around the nominal interaction point, so charged-particle tracking is performed for eta values $|\eta| \leq 1.2$. The chamber is constructed of 32 modules, contained in a cylinder made up of a thin carbon fiber tube at the inner radius and an aluminum cylinder with 0.95 cm walls at the outer radius, which serves as the support for the entire Central Detector. Aluminum end-plates hold the wire tension. The modules are constructed of Rohacell foam, which is covered with epoxy-laden Kevlar and then laminated with a layer of Kapton. The readout electronics and high voltage distribution are mounted on the aluminum end-plates.

Like the VTX, the CDC uses jet cell geometry, with four layers. There are seven $30\text{ }\mu\text{m}$ gold-plated tungsten sense wires per cell, which are staggered in ϕ by $\pm 200\text{ }\mu\text{m}$ in order to resolve the left-right ambiguity. In addition, the cells in alternate layers are rotated by one half cell width, in order to further aid pattern recognition. Grooves are cut into the module walls, radially just inside and outside the sense wire plane to hold inductive delay lines, which provide two z measurements per cell. Signals are induced on the delay lines by the adjacent sense wire; both ends of the

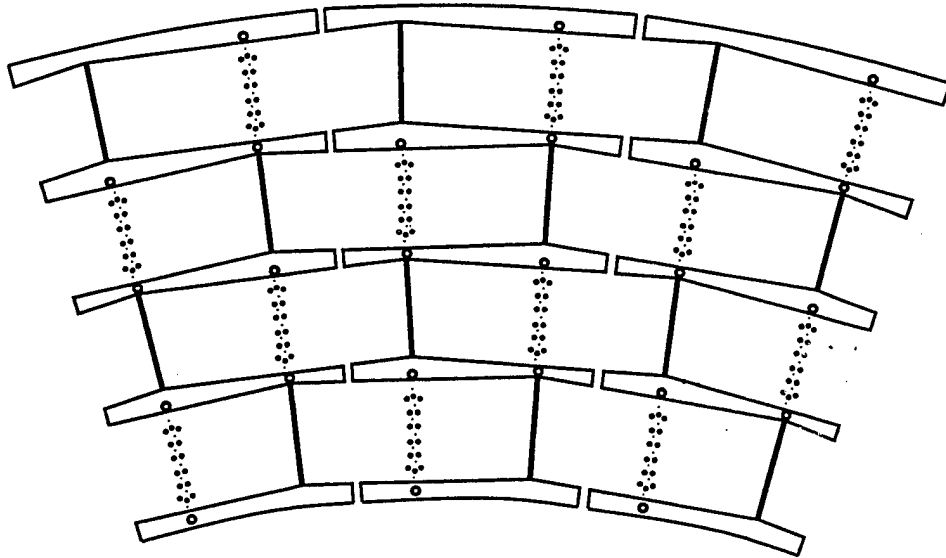


Figure 2.5: End view ($r - \phi$) of three modules of the CDC, showing the sense wires, field shaping wires, delay lines in the cell walls, and the modular construction.

delay line are read out, and the time of the signals compared to the time of the anode signal give the position of the hit along the delay line, using the known propagation velocity along the delay line (about 2.35 mm/ns). The field shaping is performed by resistive ink electrodes silk-screened onto the Kapton module walls. In addition, there are pairs of 125 μm CuBe wires between the inner sense wires that focus the field around the anodes and reduce cross-talk, in order to further reduce cross-talk and minimize the signal induced on the delay lines by inner sense wires. The CDC cell structure is shown in Figure 2.5.

The chamber is operated with a mixture of Ar (92.5 %), CH_4 (4 %), CO_2 (3 %), with a small (0.5 %) fraction of water to help control discharge. The gas is run in saturated mode, with a drift field of 620 V/cm, which corresponds to a drift velocity of 34 $\mu\text{m}/\text{ns}$. The gas gain for the inner sense wires is 2×10^4 ; the outer sense wires are run at a higher gas gain of 6×10^4 , in order to induce larger signals on the delay lines.

The spatial resolution in the drift direction is typically $175\ \mu\text{m}$ for the bulk drift region [42], ranging from less than $150\ \mu\text{m}$ for small drift distances to roughly $200\ \mu\text{m}$ for the maximum drift distance of 7 cm; the resolution degrades significantly very near the anode wires. The hit-finding efficiency at the operating gas gain is greater than 95 %. Along the z direction, the delay lines measure hit positions with a resolution of 3 mm. Since the CDC is well removed from the interaction point, the occupancy rate is reasonable, and a high efficiency of roughly 90 % is attained for isolated charged tracks. Finally, dE/dx information can be used to reject two overlapped charged tracks; rejections of greater than 75 are achieved while retaining 98 % efficiency for single tracks.

2.2.4 Forward Drift Chambers (FDC)

There are two identical Forward Drift Chambers [43], which perform tracking in the high eta regions, covering the eta ranges $-3.1 < \eta < -1.5$ and $1.5 < \eta < 3.1$. The chambers extend in radius from 11 to 61 cm, and in $|z|$ from 105 to 135 cm. Each FDC consists of three separate chambers: one Φ chamber sandwiched between two Θ chambers. The Φ chambers are each separated into 36 azimuthal sectors; the Θ chambers are made up of four independent quadrants, each of which contains six layers, arranged radially. The inner Θ chamber is rotated by $\pi/4$ with respect to the outer chamber to aid in pattern recognition; see Figure 2.6 for a schematic view of one FDC chamber. The Φ chamber construction involves G-10 cell walls and Kevlar-coated Nomex honeycomb for the front and back surfaces. The Θ chambers use cell walls of Nomex honeycomb coated with aluminum foil, with Kevlar-coated Rohacell for the front and back surfaces.

Each of the Φ chamber cells contains sixteen $30\ \mu\text{m}$ gold-plated tungsten sense wires, strung radially. The sense wires are staggered by $\pm 200\ \mu\text{m}$ to help in resolving the left-right ambiguity. There is a single grounded guard wire between each of the sense wires. Like the CDC, the field shaping is done using conductive strips on the

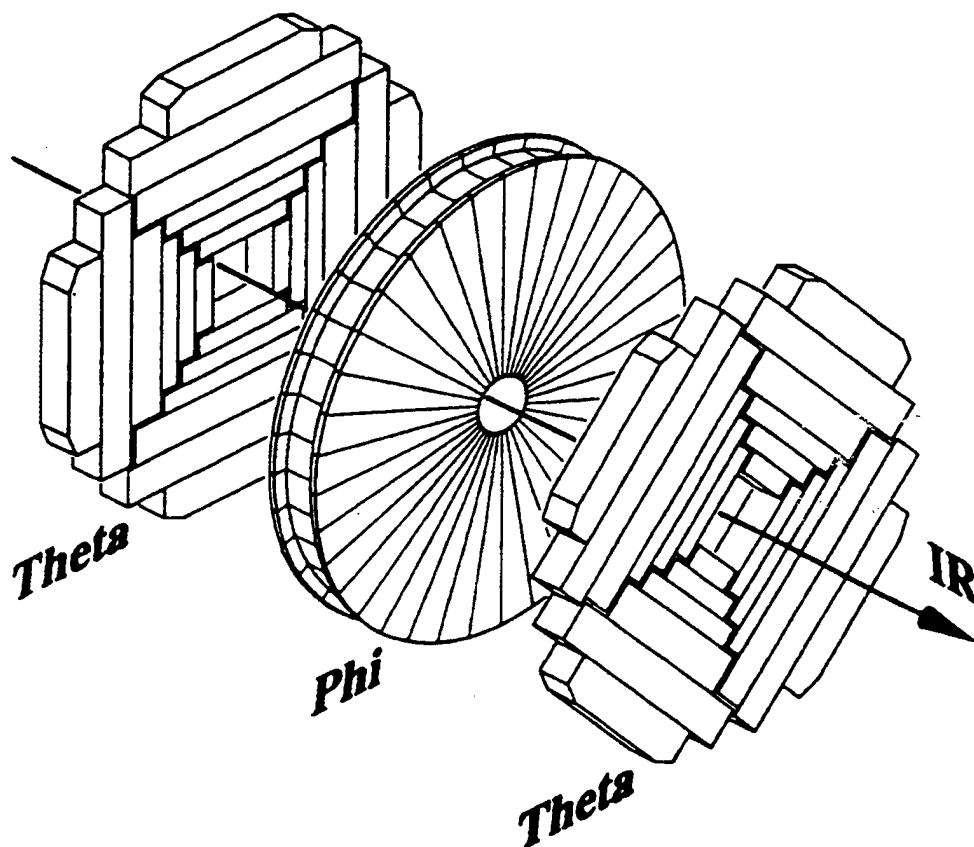


Figure 2.6: An isometric view of one FDC chamber, showing two Θ modules surrounding one Φ module.

cell walls – aluminum strips are etched onto the G-10 cell walls, and Kapton with copper traces is laminated to the front and back surfaces. There is no provision for measuring the track coordinate along the sense wire, so the Φ chamber provides azimuthal information only.

Each of the Θ chamber cells contains eight $30\text{ }\mu\text{m}$ gold-plated tungsten sense wires, staggered by $\pm 200\text{ }\mu\text{m}$. In the three inner cells of each Θ quadrant, the sense wires are located at one edge of the cell, so the electrons drift in only one direction, and there is no left-right ambiguity. There are two grounded guard wires between adjacent anodes. Copper traces on Kapton laminated to the front and back surfaces of the cells are used to shape the drift field. In each Θ cell, there is one delay line (identical to the CDC delay lines) used to measure the track position along the wire (essentially, a measurement of azimuth, which aids in matching the Θ chamber track segments to the Φ chamber segments.).

The FDC chambers use the same gas mixture as the CDC (in fact, the gas comes from the same supply). The drift field is roughly 1 kV/cm , resulting in drift velocities of roughly $37\text{ }\mu\text{m/ns}$ in the Φ cells and $40\text{ }\mu\text{m/ns}$ in the Θ chambers. The maximum drift time is about $1.5\text{ }\mu\text{sec}$, well within the time separating two consecutive bunch crossings.

The drift-distance resolution in the Φ chambers is roughly $200\text{ }\mu\text{m}$ [44]; the corresponding resolution in the Θ chambers is roughly $300\text{ }\mu\text{m}$. The hit-finding efficiency is greater than 95 % for the selected operating conditions. Pulse-pair resolution is good; two hits separated by 2 mm in the drift direction can be resolved with 90 % efficiency. The resolution along the delay lines in the Θ chambers is 4 mm. Finally, the efficiency for finding isolated charged tracks is roughly 85 %.

2.2.5 Tracking Detector Readout

The readout of all the DØ tracking chambers is similar. First, signals from the wires or delay lines are fed into charge-sensitive preamplifiers, mounted on the detector

itself. The output of these amplifiers goes into shaping amplifiers mounted in racks below the detector. The output of the shaping amplifiers is carried on cables over the shielding wall to the counting house, where the signals are digitized, and eventually read into the online computer and stored on tape.

The drift chamber preamplifiers (for both the sense wires and the delay lines) are based on the Fujitsu MB43458 common base preamplifier [45]. This preamplifier has a gain of 0.3 mV/fC, and an input noise of 2300 electrons for a typical detector capacitance of 10 pF. Two four channel surface mount packages are mounted on a ceramic hybrid to make a compact eight channel package, complete with provision for charge injection for calibration and testing.

The output signals of the preamplifiers are carried via coaxial cables to shaping amplifiers mounted in racks in the platform beneath the detector. The shaping amplifier applies frequency dependent gain to the signals, to optimize the hit-finding efficiency and pulse pair resolution, as well as maintaining good resolution for measuring the total charge deposition, for determining dE/dx . The shaping amplifiers also compensate for the effects of the long cables on the detector signals. The components which determine the shaping response are mounted on a separate header (one channel per header), so that the response can easily be tuned for each detector.

The signals from the shapers are carried on coaxial cables over the shielding wall to the Movable Counting House (MCH), where they are digitized. The signals go through three basic stages in the digitization process. First, the signals go through an analog circuit, where gain and pedestal corrections are made, and a bilinear gain is applied, in which the gain for very large signals is about a factor of 8.5 lower than the gain for small signals. This extends the dynamic range of the system by more than a factor of three, and improves the measurement of dE/dx considerably. The output of the bilinear amplifiers are flash-digitized at 106 MHz using a SONY CX20116 Flash Analogue-to-digital converter (FADC), which offers eight-bit resolution; the digitized output is stored in memory, pending a trigger decision. It is impossible to read out all the FADC data, due to the sheer volume; therefore, hardware zero suppression

is applied to the digitized data. The zero suppression is performed by a custom application specific integrated circuit (ASIC), designed at Fermilab [46]. The chip operates at 26.5 MHz on four time slices at a time, so the zero suppression keeps up with the digitization. The raw FADC values and the first differences between consecutive FADC bins are used to identify leading and trailing edges of pulses, based on a few simple and efficient algorithms [47]. The thresholds are determined by programmable registers, so each individual channel can have its own thresholds, which allows for variations in pedestal, gain and noise. The zero-suppressed FADC data are stored in memory, and are transferred to the trigger computers for software trigger processing and event building if all hardware triggers are satisfied.

2.3 Calorimeter System

Calorimetry forms the backbone of the DØ detector, since it provides the only energy measurement for all particles except for muons, and it forms the basis for nearly all particle identification. Since there is no central magnetic field (and therefore no bulky magnet), the calorimeter system could be made very compact, with as few cracks and dead regions as possible. The calorimeter was also designed to have as uniform response as possible over the entire eta coverage.

2.3.1 Calorimeter Basics

A calorimeter measures the energy of incident particles [48]. To do this, the particle is stopped in the calorimeter material, and the energy of the resultant shower is measured. In order to make a good measurement of the energy, there must be enough material in the calorimeter to fully contain the shower, since any energy that escapes the calorimeter is not measured. In addition, there must be some way of actually measuring the deposited energy. In order to build a compact calorimeter with excellent energy containment, DØ chose to use a sampling calorimeter, using

uranium as the primary absorber material.

In a sampling calorimeter, not all the material is active, so not all the energy is actually measured. Very dense material is used to provide the necessary thickness to stop the incident particles; this dense material is not active, however. The active material is sandwiched between dense absorber plates to sample the energy of the particle showers; usually, the energy is measured by means of measuring the ionization produced by the charged particles in the shower. The portion of energy that is actually measured by the calorimeter is called the *sampling fraction*.

The energy measurement clearly depends on how many charged particles are produced in a shower, and how many ionization electrons are produced in the active medium. There is no special reason that all types of particles would produce the same sorts of showers. Aside from neutrinos and muons which interact very little or not at all in the calorimeter, particle showers can be classified into two types: electromagnetic and hadronic.

Electrons and photons produce electromagnetic showers. For high energy electrons, the dominant energy loss is through bremsstrahlung radiation of photons. For energetic photons, electron-positron pair production is the dominant mode of energy loss. In a dense medium such as the calorimeter, the cross section for these interactions is high, and a cascade reaction results in a very compact electromagnetic shower. The energy of the original particle is expected to drop exponentially:

$$E = E_0 e^{-x/X_0} \quad (2.2)$$

where X_0 is known as the radiation length of the material. The radiation length of the uranium used to make up the electromagnetic calorimeters is 3.2 mm [33].

Hadronic showers are very different from electromagnetic showers. Hadrons lose very little energy to bremsstrahlung, due to their large mass; instead, they lose most of their energy through inelastic collisions with nuclei in the absorber material. Some of this energy loss produces ionization, such as energetic charged secondaries, and π^0 mesons, which decay to two photons. The rest of the energy is dissipated through

slow charged secondaries, neutrons and neutrino production, which produce little measurable ionization. Even though the hadronic showers are well contained within the calorimeter, some of the energy is not detected via ionization. In addition, the cross section for inelastic collisions that make up the hadronic showers is much smaller than those for the electromagnetic cascades; as a result, hadronic showers are in general much larger than electromagnetic showers. For hadronic showers, the analog to the radiation length is the nuclear interaction length, λ_0 , which is the mean free path of hadrons between inelastic nuclear collisions. For uranium, the interaction length is 10.5 cm [33]. The difference in shower shape and size is the primary tool that DØ uses to differentiate electromagnetic and hadronic showers.

The signal measured for incident electrons or hadrons of the same energy can be different, since some of the energy from hadronic showers is not detected by ionization. The ratio of the measured signals for electrons and hadrons with equal incident energies is called the intrinsic e/π ratio of the calorimeter; ideally, it is unity.

The energy resolution of a calorimeter is usually parametrized as

$$\frac{\sigma_E}{E} = C + \frac{S}{\sqrt{E}} + \frac{N}{E} \quad (2.3)$$

where C represents the calibration error, S represents the sampling error, and N represents the noise contribution. The sampling term usually dominates; the $1/\sqrt{E}$ nature of the sampling noise can be understood in terms of Poisson statistics being applied to the number of ions produced in a cascade, which is roughly proportional to both the incident energy and the measured signal.

2.3.2 Calorimeter Design and Geometry

DØ uses sampling calorimeters, with metal plates as the absorber material and liquid argon as the active sampling medium. The primary absorber material is uranium; copper and stainless steel are also used in outer parts of the calorimeter where less energy is deposited and the measurement does not need to be as precise. Particle

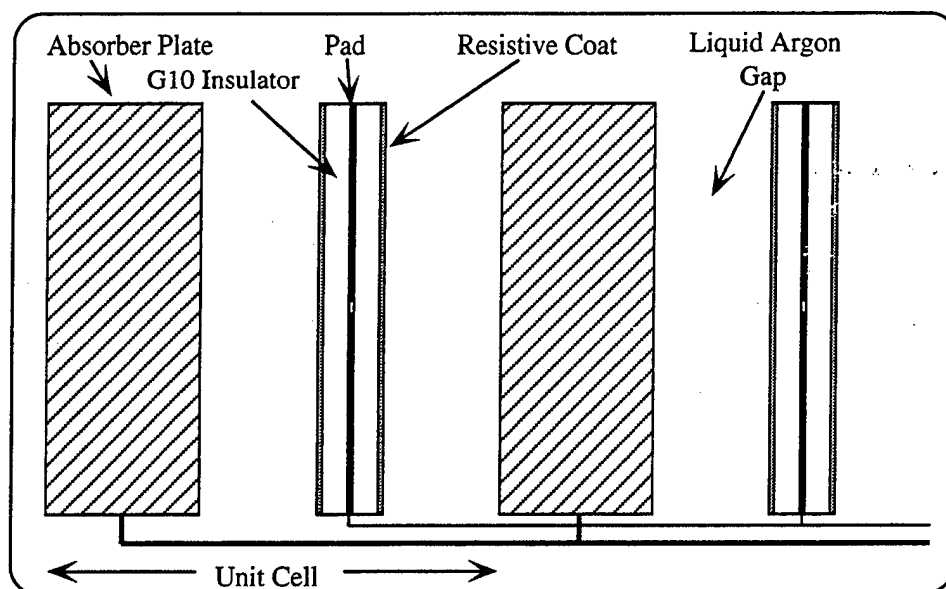


Figure 2.7: Schematic view of the unit cell in the liquid argon calorimeter.

showers are created when high-energy incident particles pass through the absorber material; charged particles from those showers create electron-ion pairs in the liquid argon. The ionized charge is collected using an electrostatic field, which produces a measurable signal. A schematic view of a single cell of the calorimeter is shown in Figure 2.7. A readout board is located midway between two adjacent absorber plates; the liquid argon gap between the absorber surface and the surface of the readout board is 2.3 mm. Typical readout boards consist of copper readout pads sandwiched between two layers of insulating G-10; a layer of resistive epoxy coats each outer surface. Positive high voltage is applied to the resistive coat, while the absorber plates are kept at ground; the typical field strength in the gap is 8.7 kV/cm. As the electrons drift in the liquid argon under the influence of the electric field, a signal is induced on the signal pads. Since there is no charge multiplication, multiple cells are ganged together in depth to produce a larger signal.

The DØ calorimeter was designed to be as hermetic as possible, minimizing the

DØ LIQUID ARGON CALORIMETER

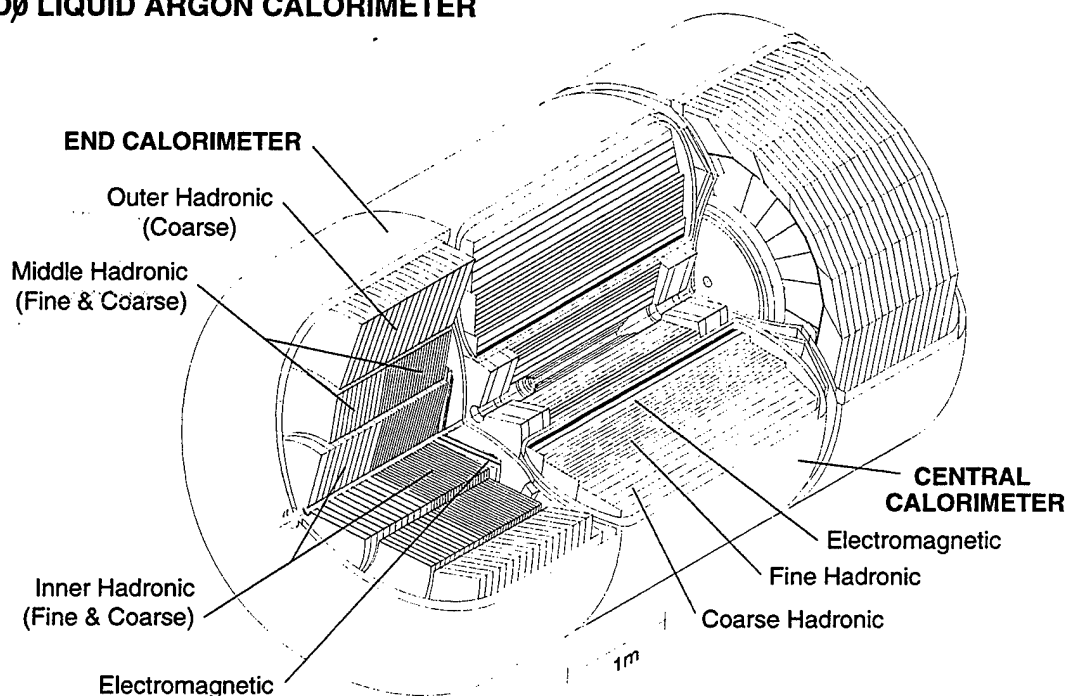


Figure 2.8: Isometric view of the Calorimeter system, identifying the various module types.

cracks and the dead regions. Ideally, the only holes in the calorimeter would be for the Tevatron beam-pipe; unfortunately, the need for access to the central detector required the calorimeter to be made up of more than one piece, with each piece in a separate cryostat (necessary to hold the liquid argon at cryogenic temperatures). In the end, a three piece design was chosen, made up of the central cryostat (CC) covering an eta range of roughly $|\eta| \leq 1$, and two end-cap cryostats (ECN and ECS), positioned symmetrically on either side of the CC, and extending the eta coverage to roughly $|\eta| = 4$. The CC forms a torus around the CD; both ends of the CD are accessible. An isometric view of the calorimeter system is shown in Figure 2.8.

The calorimeter is separated into several sections longitudinally (in depth). Electromagnetic showers develop very quickly, so the EM calorimeter modules are closest

to the interaction point. The EM modules use thin (3 mm in the CC, 4 mm in the EC) uranium absorber plates, to maximize the number of samples and allow longitudinal segmentation appropriate for the quickly developing electromagnetic showers. Directly behind the EM modules are the fine hadronic (FH) modules, which use slightly thicker (6 mm) uranium plates as absorbers. Most of the energy from hadronic showers is deposited in the fine hadronic section; although some will be deposited in the EM section. The longitudinal segmentation of the FH section is optimized for the typical development of hadronic showers. The last layer of the calorimeter is the coarse hadronic (CH) section, which catches whatever energy escapes out of the back of the fine hadronic section. The CH uses thicker stainless steel or copper plates as absorber material.

The transverse segmentation is based on pseudo-projective towers; the centers of the calorimeter readout cells all lie along fixed- η rays originating from the nominal vertex point. However, the readout cell boundaries are perpendicular to the absorber plates, instead of pointing towards the origin. Therefore, all the readout boards that are ganged together to form one layer in the calorimeter are the same, which greatly simplified the construction of the calorimeter by reducing the number of different signal boards to a manageable level. The pseudo-projective segmentation is illustrated in Figure 2.9, which shows a plan view of one quadrant of the Calorimeter and Central Detector. The transverse segmentation of the readout towers is $\Delta\eta = 0.1$ by $\Delta\phi \approx 0.1$ (the full 2π azimuth is split into 64 towers). The segmentation is twice as fine ($\Delta\eta = 0.05$ by $\Delta\phi \approx 0.05$) in the third layer of the electromagnetic section (EM3), where the EM shower development is at maximum; this allows excellent measurement of the shower shape, as well as precise position measurement. Finally, at very large values of pseudorapidity, the η segmentation is coarser in order to keep the physical size of the readout pads reasonable in comparison to the size of the shower. A schematic view of the segmentation of the calorimeter is shown in Figure 2.10.

Despite the best efforts to minimize the amount of dead space in the calorimeter, the transitions between the different cryostats create significant gaps in the coverage

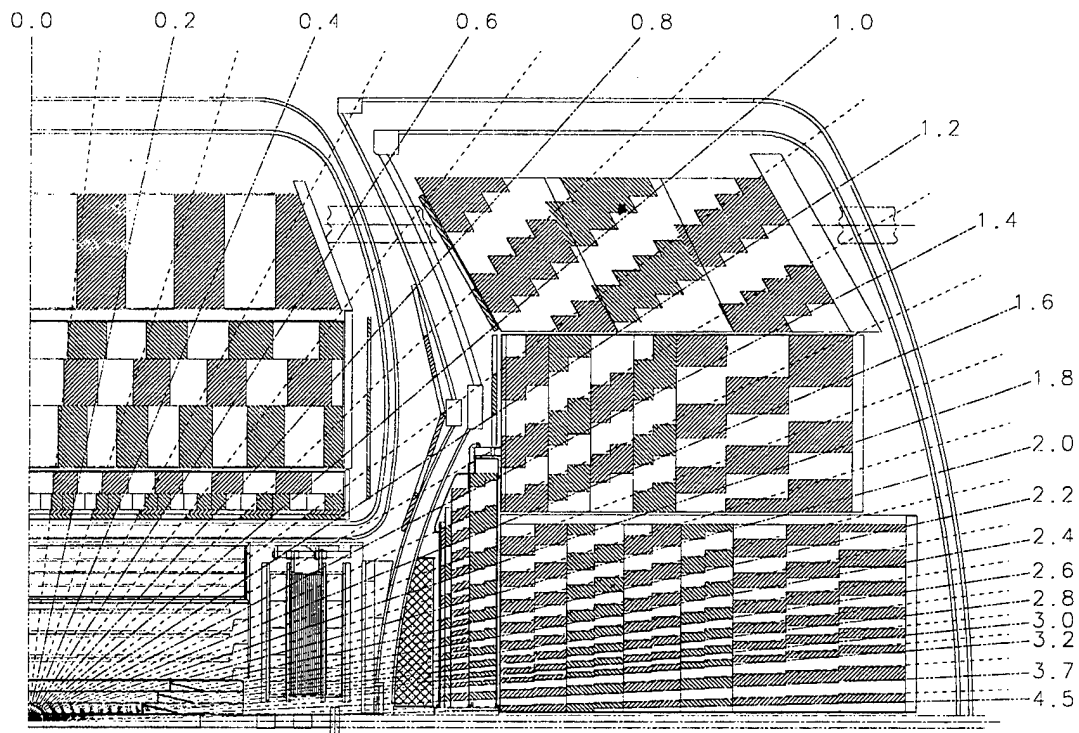


Figure 2.9: Plan view of one quadrant of the calorimetry and central tracking systems, with lines of constant pseudorapidity superimposed. The pseudo-projective tower structure of the calorimeter cells is evident.

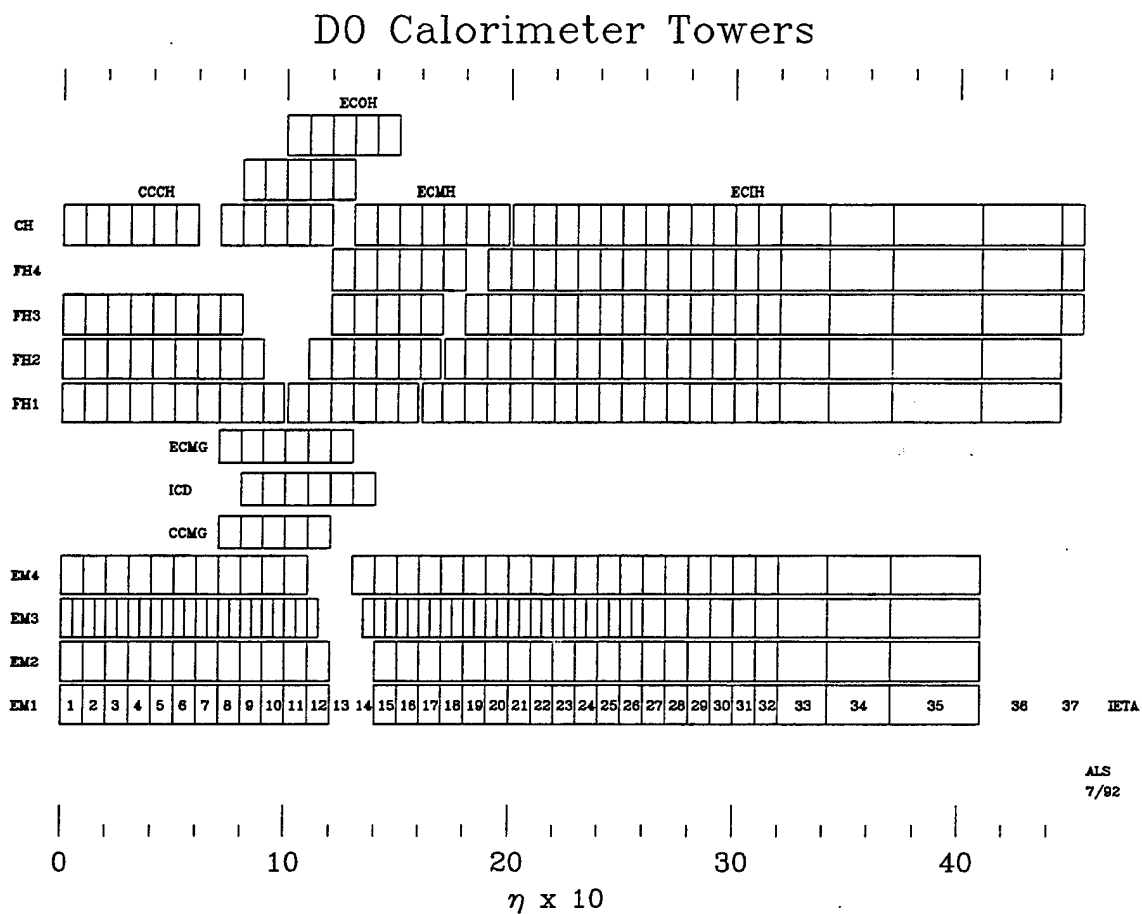


Figure 2.10: Diagram showing the distribution of calorimeter cells in depth and rapidity, including the Massless Gaps (MG) and the Inter-Cryostat Detector (ICD).

in the region $0.8 \leq |\eta| \leq 1.4$. Two systems were developed in order to help measure the energy in this region, the Massless Gaps (MG) and the Inter-Cryostat Detector (ICD); the η coverage of these systems is shown in Figure 2.10. The Massless gaps consist of several layers of readout boards with no absorber plates separating them. These are positioned between the calorimeter modules and the cryostat wall, in both the CC and the EC's. The ICD is a detector system made up of plastic scintillator tiles, which use photomultiplier tubes for readout. The ICD systems (one for each end) are mounted on the inside face of the end cryostats; the segmentation in η and ϕ matches that of the calorimeter. Both the MG and ICD systems are visible in Figure 2.9.

Some relevant parameters for the CC calorimeter modules are summarized in Table 2.1 [42]; the same parameters for the EC modules are given in Table 2.2 [42]. Note that the values for the radiation lengths and nuclear absorption lengths assume normal incidence to the absorber plates, and that the Middle Coarse Hadronic (MCH) and Outer Hadronic (OH) modules share 64 channels, as indicated in the table. Also, for the absorber material, UNb denotes depleted uranium with 1.7 % Niobium alloy, and SS represents stainless steel.

2.3.3 Calorimeter Readout

The readout of the calorimeter is performed in three steps. First, the signals are carried by coaxial cables through the cryostat feed-through ports to the charge-sensitive preamplifiers which are mounted on the outside of the cryostats. The output from the preamplifiers is carried on twisted-pair cables to the baseline subtractor (BLS) circuits mounted in the platform below the detector. Finally, the output of the BLS modules is carried by more twisted-pair cables to the MCH where the signals are digitized.

The calorimeter charge-sensitive preamplifiers are simple circuits, using a single Toshiba 2SK147 j-FET at the input. The circuit was built with two separate gains,

	EM	FH	CH
Number of Modules	32	16	16
Absorber Material	U	UNb	Cu
Absorber Thickness (mm)	3	6	46.5
Argon gap (mm)	2.3	2.3	2.3
Number of Readout Boards	21	50	9
Number of Readout Layers	4	3	1
Cells per Readout Layer	2,2,7,10	20,16,14	9
Total Radiation Lengths (X_0)	20.5	96.0	32.9
Total Interaction Lengths (λ)	0.76	3.2	3.2
Sampling Fraction (%)	11.79	6.79	1.45
Number of Readout Channels	10368	3000	1224

Table 2.1: Summary of Central Calorimeter module parameters.

	EM	IFH	ICH	MFH	MCH	OH
Number of Modules	1	1	1	16	16	16
Absorber Material	U	UNb	SS	UNb	SS	SS
Absorber Thickness (mm)	4	6	6	6	46.5	46.5
Argon gap (mm)	2.3	2.1	2.1	2.2	2.2	2.2
Number of Readout Boards	18	64	12	60	14	24
Number of Readout Layers	4	4	1	4	1	3
Cells per Readout Layer	2,2,6,8	16	14	15	12	8
Total Radiation Lengths (X_0)	20.5	121.8	32.8	115.5	37.9	65.1
Total Interaction Lengths (λ)	0.95	4.9	3.6	4.0	4.1	7.0
Sampling Fraction (%)	11.9	5.7	1.5	6.7	1.6	1.6
Number of Readout Channels	7488	4288	928	1472	384 + 64 + 896	

Table 2.2: Summary of End-cap Calorimeter module parameters (the numbers apply for *each* end-cap).

corresponding to full scale amplitudes of 100 and 200 GeV, to cover the full dynamic range for all cells. For each channel, a calibration signal, injected through a large precision resistor, can be attenuated so that the full dynamic range of the preamplifiers can be tested. The calibration system was carefully designed to feed the same amplitude signal to all channels; the overall precision and stability of the system have been shown to be better than 0.25 %.

The BLS system performs several functions. First of all, at the input to the BLS, a portion of each signal is extracted with a fast rise-time for use in the hardware calorimeter trigger; for this purpose, the signals are summed into trigger towers of $\Delta\eta \times \Delta\phi = 0.2 \times 0.2$. Logical cells that straddle the CC-EC boundary are merged at the input to the BLS. For the data path, the signals are shaped so that the signal reaches its peak roughly 2.2 μsec after the beam crossing. Each signal is sampled twice, once just before the beam crossing and once at 2.2 μsec after the beam crossing; the difference between these samples is a dc voltage proportional to the charge collected. At the output of the BLS, this voltage is amplified by either 1 or 8, depending on the signal size, in order to maximize the range that is attained by the digitization process. The outputs of the BLS are multiplexed sixteen-fold into serial time slices, to reduce the cable and digitization hardware requirements.

The signals from the BLS modules are digitized using 12-bit ADC circuits; along with the x8 amplification for small signals in the BLS, this results in an overall 15-bit dynamic range (the full scale energy for each channel can be measured to one part in 2^{15}). Each signal is digitized in 10 μsec , so the sixteen time slices are digitized in a total of 160 μsec ; since this is much longer than the beam crossing time, digitization is only performed if the requirements of the fast hardware trigger are met. The gains in the system are set so that one least count corresponds to 3.75 MeV of deposited energy. Simple threshold-based zero suppression can be applied at the digitization stage to reduce the size of the data block transferred to the Level-2 trigger system and then possibly to tape.

2.3.4 Calorimeter Performance

The DØ calorimeter is a very complicated device, and a full description of its performance is well beyond the scope of this paper [49]. The calorimeters have been tested in several ways, either by studying a subset of the modules in a test beam program, or by using cosmic rays to study the whole detector *in situ*. Some representative results are presented here.

Based on test beam studies of the ECEM and ECMH modules, the energy response to both electrons and pions was shown to be linear within 0.5 % for beam energies ranging from 10 GeV to 150 GeV. The energy resolution, parametrized as

$$(\sigma_E/E)^2 = C^2 + S^2/E, \quad (2.4)$$

was also measured. For electrons in the ECEM, $C_{ele} = 0.032 \pm 0.004$ and $S_{ele} = 0.157 \pm 0.005 \sqrt{\text{GeV}}$; for pions in the ECMH, $C_\pi = 0.032 \pm 0.004$ and $S_\pi = 0.41 \pm 0.04 \sqrt{\text{GeV}}$.

Position resolution in the EM calorimeters is important for electron identification, which requires a track match. For 100 GeV electrons, the position resolution in the ECEM ranged from 0.8 to 1.2 mm as the impact position varied.

Finally, it should be mentioned that the calorimeter is not perfectly compensating; that is, the response to electrons and pions of the same incident energy is not equal. The e/π response ratio varies from 1.11 at 10 GeV incident energy to 1.04 at 150 GeV.

2.4 The DØ Trigger System

The DØ trigger system is used to select interesting events to be recorded for later analysis, since it is clearly impossible to record detector data for all beam crossings (which occur with a period of 3.5 μsec , or a rate of roughly 285 kHz). Instead of just taking a random sampling of events, the trigger uses detector information to determine whether an event is interesting and should be recorded; the vast majority of the $p\bar{p}$ crossings produce events of little physics interest.

The DØ trigger system is organized into three levels. The Level-Ø trigger uses a set of scintillator counters to indicate the presence of an inelastic collision; at typical luminosities, the event rate out of Level-Ø is around 100 kHz. The Level-1 trigger framework is a hardware trigger, based on detector data from fast trigger pick-offs. The Level-1 system runs with the same period as the accelerator, and most trigger decisions are made within the $3.5 \mu\text{sec}$ time gap between crossings (so they are *dead-time-less*). The event rate out of Level-1 is about 100 Hz. For events that pass the Level-1 trigger requirements, the full detector is digitized, and the data is read into the Level-2 system, which is a farm of VAX computers. The Level-2 trigger is a purely software trigger, allowing for sophisticated algorithms and the use of data from the full detector. Events that pass the Level-2 system are written to tape for later analysis; the event rate out of Level-2 is less than 2 Hz. See Figure 2.11 for a schematic view of the DØ trigger system.

2.4.1 Level-Ø

The Level-Ø system [50] is used to detect inelastic, hard $p\bar{p}$ scattering, and is used as the luminosity monitor for the DØ experiment. As such, it is very important to this cross section analysis, and will be described in some detail. The Level-Ø hardware consists of two scintillation counter arrays mounted on the front surfaces of the two end cryostats, along with the necessary phototubes for readout. The arrays are square, and provide partial coverage of the rapidity range $1.9 < |\eta| < 4.3$; nearly full coverage is provided in the range $2.3 < |\eta| < 3.9$. The acceptance and efficiency of the counter arrays is such that greater than 99 % of the hard-scattering events produce a Level-Ø coincidence (both arrays must be hit).

Each scintillator array consists of two identical planes, rotated 90° with respect to each other. Each plane consists of 10 small scintillator squares ($7 \times 7 \text{ cm}^2$) read out by a single photomultiplier tube, and 4 long scintillator rectangles ($7 \times 65 \text{ cm}^2$) read out on both ends. The small squares cover the very high eta region, while the

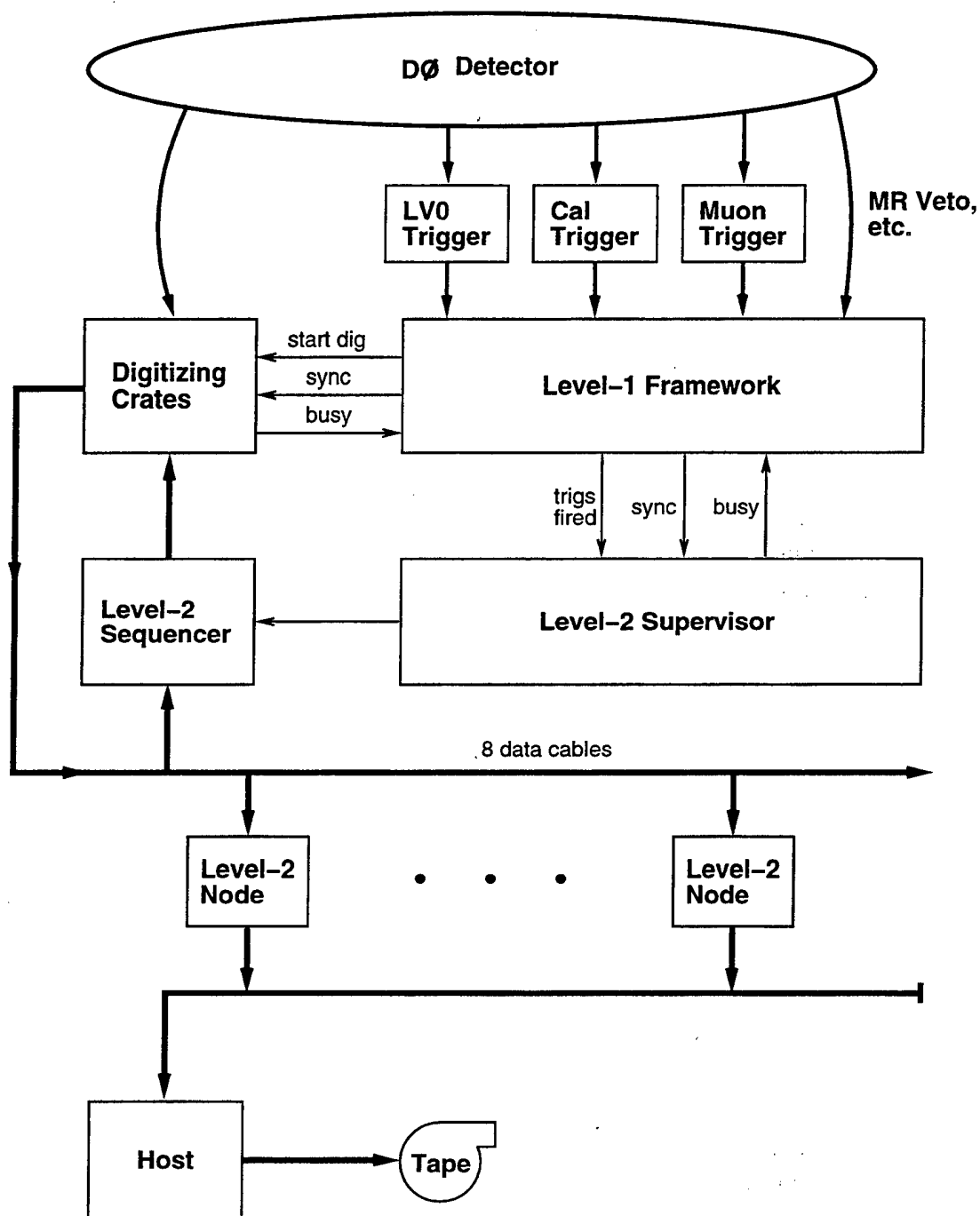


Figure 2.11: Schematic block diagram of the DØ trigger and data acquisition systems.

long strips define the outside of the rectangular array; when the two planes are fit together, there is no overlap between the small tiles, and the long strips only overlap at the corners. The layout of the Level-0 counters is illustrated in Figure 2.12.

An inelastic collision is indicated by a coincidence of hits in both counter arrays, with very little background from diffractive events. At low luminosity, there are very few multiple interaction crossings, and the coincidence rate is almost exactly proportional to the instantaneous luminosity. At higher luminosities, however, the rate of multiple interactions increases, and the coincidence rate starts to saturate (only one coincidence is recorded for a crossing with more than one interaction). With a high rate of multiple interactions, a correction must be applied to the coincidence rate to get the instantaneous luminosity; this is discussed in detail as part of the description of the luminosity determination.

Timing information from the Level-0 counters is used to provide fast z -vertex determination for use in the trigger. Due to the large spread of the vertex distribution ($\sigma_z \approx 30$ cm), a large error in the determination of the transverse energy will result if no correction is made. The time difference between the hits on the two counter arrays is used to determine the z -vertex, which requires very good timing resolution; the Level-0 counters and electronics combine to give a timing resolution ranging from 100 to 150 ps, for both the short counters and the long counters (which take advantage of time averaging of the signals from both ends). To obtain a fast vertex measurement for use in the Level-1 hardware trigger, signals from the small counters are summed, and a fast time-to-digital converter (TDC) is used to measure the time difference and make a rough vertex measurement; this measurement is used by the Level-1 calorimeter trigger to choose the appropriate lookup table for calculating the transverse energy. In addition, signals from the individual counters are processed with all the appropriate calibration corrections, and a slower but more accurate measurement of the z -vertex is made; this measurement is available for use in the Level-2 (software) trigger decisions. The time distribution of the counter hits is used to indicate the likelihood of a multiple event crossing, and a multiple interaction flag is provided to the trigger system.

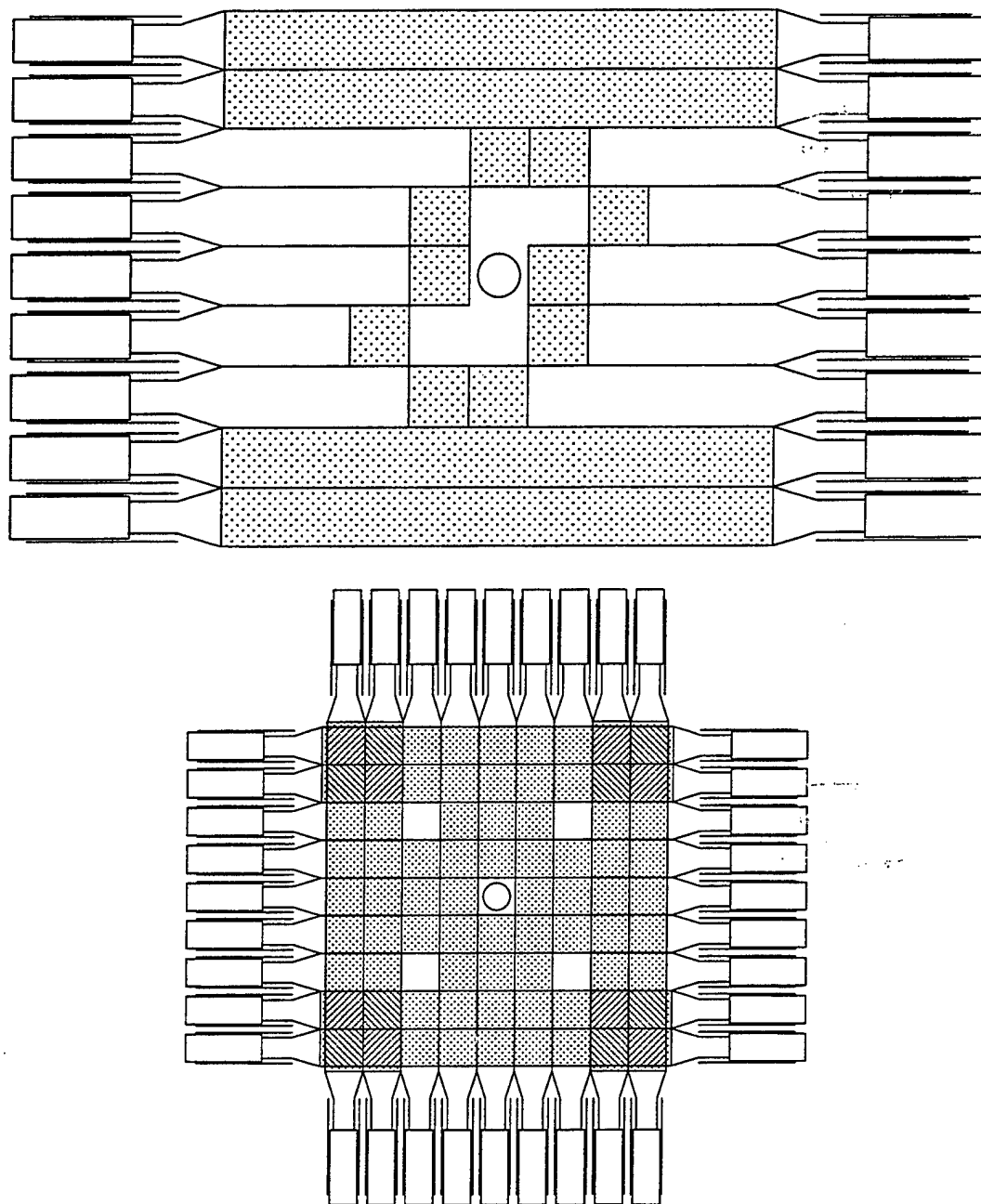


Figure 2.12: The top figure shows a single plane of one Level-Ø array; the shaded regions are scintillator. The bottom figure shows the two overlapping planes of one Level-Ø array.

2.4.2 Level-1 Framework

The Level-1 trigger framework [51] is a very flexible and highly programmable hardware system that collects prompt detector data and makes a very fast trigger decision; see Figure 2.13 for a schematic diagram. The system is synchronized with the beam crossings within the detector; most Level-1 trigger decisions are made within the $3.5 \mu\text{sec}$ time gap between crossings, allowing operation with no dead-time from crossings that do not satisfy the Level-1 trigger requirements. Prompt detector data is available from the calorimeter, muon and Level-0 systems; in addition, the trigger decision can incorporate vetos due to Main Ring activity and apply prescales to reduce the output rate.

The core of the Level-1 framework is a two-dimensional fully programmable AND-OR logic network, incorporating 256 inputs, each of which is a latched bit containing specific detector information (for example, one input line might contain information on whether there was at least one electromagnetic trigger tower with a transverse energy of at least 12 GeV); there are 32 output terms, corresponding to the 32 specific Level-1 triggers. Each of the specific triggers is formed by a logical state of the 256 input terms, requiring each bit in turn to be asserted, negated or ignored, depending on the requirements of the trigger. For the W and Z cross section analyses described here, the Level-1 trigger decision was based solely on calorimeter, Level-0 and Main Ring veto information; the muon trigger was not used, and will not be described here.

2.4.2.1 Level-1 Calorimeter Trigger

As mentioned previously, the fast pick-off signals from the calorimeter BLS modules are summed into towers of $\Delta\eta \times \Delta\phi = 0.2 \times 0.2$ for use in the Level-1 Calorimeter trigger. The trigger extends out to $|\eta| = 4.0$, so there are a total of 1280 trigger towers; each tower is split into electromagnetic and hadronic sections, for a total of 2560 energy measurements. Each energy measurement is analog-weighted in order to convert it to a transverse energy and then digitized using an 8 bit FADC. The corrected

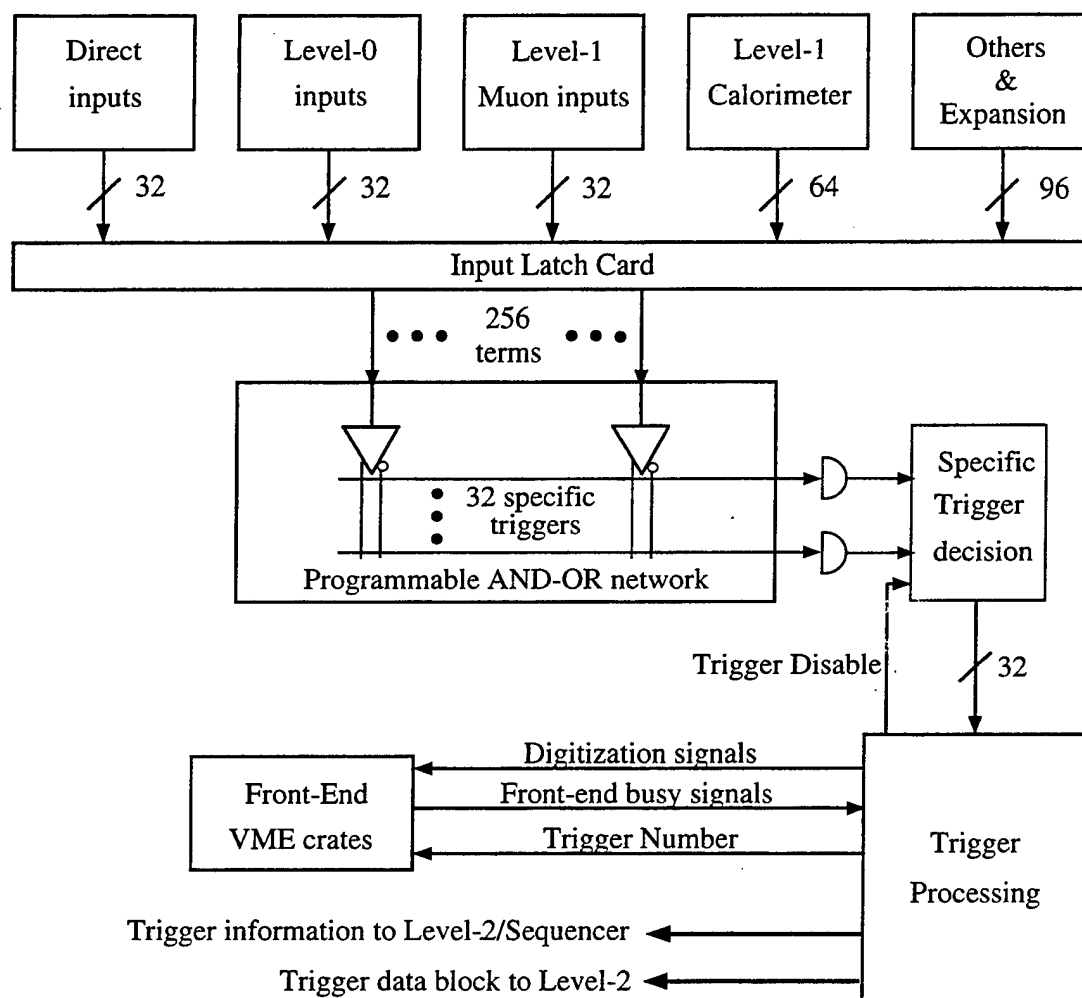


Figure 2.13: A schematic view of the Level-1 trigger framework.

transverse energy is determined by using the digitized energy and three bits from the Level-0 fast z -vertex measurement to address a fast memory lookup table. The x - and y -components of the transverse momentum for a trigger tower, P_x and P_y , are calculated by summing the corrected electromagnetic and hadronic energies for that tower, then using that digital sum as an address for the P_x and P_y memory lookup tables. Finally, seven global energy sums are calculated (a global sum is a sum over all the trigger towers in the detector): electromagnetic, hadronic and total uncorrected E_T , electromagnetic, hadronic and total corrected E_T , and finally the missing transverse energy, \cancel{E}_T , formed from the global sums of the corrected x - and y -components of the transverse momenta.

The trigger decision is very flexible. Each of the seven global sums can be compared to up to 32 different thresholds; the results of each comparison can be used as an input to the Level-1 framework AND-OR network (note that in general practice, few thresholds are actually used, so not many of the AND-OR input lines are used up). In addition to using the global sums, the trigger can be based on the energies in the individual trigger towers. There are four sets of electromagnetic tower thresholds, each with an associated hadronic veto threshold (if the hadronic energy in the tower is above that threshold, the tower is vetoed, even if the electromagnetic energy is above threshold). Each of these threshold pairs is called an EM E_T reference set. In addition, there are also four thresholds used for the total (sum of electromagnetic and hadronic) transverse energy in each tower, known as total E_T reference sets. For each of these eight reference sets, a global count of the number of trigger towers that exceed the thresholds is made; the count is then compared with up to 32 programmable count thresholds, and the results can be used as inputs to the Level-1 AND-OR network (once again, not all the count thresholds are used, so the input terms are not all used up). For example, one of the AND-OR lines from the calorimeter trigger might require there to be at least one trigger tower with at least 10 GeV of electromagnetic energy with no hadronic veto; this formed the basic Level-1 trigger requirement for the cross section analyses described here.

2.4.2.2 Main Ring Vetos

In order to maximize the luminosity, the Main Ring is almost always in use making antiprotons, even when physics data is being taken during a Tevatron store. Unfortunately, parts of the Main Ring operation cycle create unacceptable noise in the DØ detector, especially since the Main Ring beam-pipe passes through the calorimeter itself. In order to avoid writing events taken during these noisy periods, veto signals are produced and incorporated into the Level-1 framework.

There are two types of Main Ring vetos, named Microblank and MRBS_LOSS. The Microblank veto removes events taken when Main Ring bunches are present within ± 800 ns of the beam crossing, which is when the muon chambers are live; this accounts for a dead-time of roughly 8 %. MRBS_LOSS vetoes events taken during Main Ring injection and transition, and accounts for a dead-time of about 17 %. Note that if the Main Ring is not operating, the vetos are disabled.

2.4.3 Level-2

If at least one Level-1 specific trigger is satisfied, the data from the full detector are digitized and read into the Level-2 system, which consists of a farm of Digital Equipment Corporation Vax (Virtual Address eXtension) computers [52]. One processor node is used to apply a partial reconstruction (processing time constraints prevent full reconstruction) and apply the software filters associated with each Level-1 trigger that was satisfied. Full detector data is available, so the calorimeter and muon information is superior to the data available to the Level-1 trigger; in addition, tracking information can be used to provide electron or muon confirmation. If the event is passed by any Level-2 filter, it is transferred to the host computer and written to tape.

The event rate out of the Level-1 trigger is about 100 Hz; the rate out of Level-2 to tape peaks at 2 Hz. The data is divided into two paths. First, all events are written to the ALL stream and stored on tape for later reconstruction. In addition, the

most interesting events (defined by passing one of a few specially chosen filters) are written to the EXPRESS stream and stored on tape; these tapes are then immediately processed, allowing for prompt analysis.

2.5 Final Comments

The description of the detector presented here is incomplete, and is meant only to give enough understanding in order to understand the analysis that follows. Many essential systems have been ignored completely, since they have no direct bearing on the analysis (other than allowing the detector to run!).

Chapter 3

Event Reconstruction and Particle Identification

The process of finding and identifying physical particles out of thousands of channels of raw data is very complicated and difficult; the success of all physics analyses depends on this reconstruction being performed reliably. First, the raw data from each detector are processed to form high-level objects, such as energy clusters in the calorimeter or tracks in the tracking or muon systems. Then these objects are combined to form the description of the particles produced by the $\bar{p}p$ collision: electrons, photons, jets (quarks and gluons), neutrinos (\cancel{E}_T), muons and taus. These particles and their measured properties form the basis for this analysis; therefore, it is essential to fully understand the reconstruction process, as well as know how well the reconstructed particle corresponds to the real physical object.

3.1 Raw Data to Particle Definition: RECO

There are approximately 100,000 electronics channels in the DØ detector. When an event passes the trigger, the data from all these channels (along with the results of the Level-2 filter processing) are written in raw form to an output file on disk,

then copied to tape. In order to make the data usable for physics analysis, the data are processed by the standard reconstruction program, RECO [53]. For each detector system, this program unpacks the raw data, applies all the necessary calibrations and corrections, and applies hit-finding/cluster-finding/track-finding algorithms in order to form higher level reconstructed objects (energy clusters, tracks). Finally, these objects are used to define physics objects, or particles. A full account of the reconstruction process [53] is outside the scope of this paper, so a brief description will be presented, with detail given when it is relevant to this analysis.

3.1.1 The Raw Data

When an event passes the requirements of one or more Level-2 filters, it is written to an output file. The event record contains raw data from all of the detectors, as well as the results of the Level-1 and Level-2 trigger processing. All DØ data are stored in ZEBRA banks, where ZEBRA is a CERN software product [54] which allows dynamic memory allocation and mixing of data types within the restrictive confines of the FORTRAN programming language. In ZEBRA, data banks are arranged in an inverted tree structure; the top level bank in the DØ event record is named HEAD; the raw data banks hang directly from HEAD (that is, there are memory links within the HEAD bank that point to the raw data banks, and vice versa). A full description of the use of ZEBRA by DØ is beyond the scope of this thesis [53].

There are eight raw data banks, each corresponding to a single data cable connecting the front-end digitizing hardware and the Level-2 multi-port memory. There is one cable for each of the central detectors, due to the high volume of data resulting from flash-digitizing each signal – one byte is written for every time slice that passes the zero suppression algorithm. The volume of data stored for the calorimeter and muon systems is much smaller, since a maximum of one word (four bytes) is written per channel; as a result, only two cables are used to carry the calorimeter data, and the muon data are carried by a single cable. Finally, one cable is used to carry in-

Bank Name	Detector	Average Size (kB)
TRGR	Trigger	25
MUD1	Muon System	25
CDD1	Vertex Drift Chamber	120
CDD2	Central Drift Chamber	115
CDD3	Forward Drift Chamber	150
CDD4	Transition Radiation Detector	125
CAD1	Calorimeter (North)	15
CAD2	Calorimeter (south)	15

Table 3.1: Names and typical sizes of the raw data banks for each readout section

formation from the Level-1 trigger framework to the Level-2 system. The names and typical sizes of the raw data banks are listed in Table 3.1.

All of the raw data are available to the Level-2 filter algorithms, including information from the Level-1 trigger framework, which determines which filter algorithms are run, and provides seeds for the simplified online clustering algorithms. The results of all of the Level-2 filters that were run are written to the output file along with the raw detector data.

3.1.2 Calibration and Run Condition Monitoring

In order to accurately reconstruct the data stored for each detector, it is important to carefully monitor the response of each electronics channel, as well as the running conditions at the time of event taking. Electronic calibration data include pedestal, gain and time information; the calibration information can change with time due to long term drift of the electronics, or due to the replacement of faulty or broken electronics modules. In addition to the variation of the electronic calibration, variation of the response due to changing run conditions must also be taken into account. Detector response can depend on many things, including temperature, atmospheric pressure

and instantaneous luminosity. These conditions must be monitored and recorded regularly, so that appropriate corrections can be applied during reconstruction of the raw data.

Calibration data are collected in special runs, taken between collider runs. For all the electronics, pedestal and gain values are measured; for the central tracking electronics, time information can also be measured (essentially, the propagation time of the signal cables is determined). The pedestals are measured by turning off all zero suppression and taking many measurements of each channel with no input signal. For gain or time measurements, a pulser is used to distribute a signal to each channel, and the pulse area or pulse time is measured in order to determine the calibration. After a calibration run, the results are stored in a database, which is used during the reconstruction of the collider data.

In general, the electronics calibration was very stable and changed very little over time. The calibration runs were very useful in identifying bad electronics channels or modules, which could then be fixed or replaced. One important use of the calibration data for all of the detector electronics was the use of the pedestal value and its rms variation to set the thresholds used by the zero suppression algorithms.

The environmental and detector conditions during running are also monitored, and stored in a separate database, which is read during event reconstruction. Some of these conditions directly affect the reconstruction, usually in the form of gain corrections. Some of these conditions include atmospheric pressure, temperature, instantaneous luminosity, and even sense wire voltage in the case of the vertex chamber. Other conditions are monitored in an attempt to ensure the quality of the data, or to detect a problem; examples include liquid argon purity for the calorimeter or drift velocity information for the drift chambers (measured using special "canary chambers", which are small detectors located outside of the collision hall designed to detect problems in the gas mixture for the drift chambers).

3.1.3 Reconstruction Begins: Vertex Finding

The first step of the reconstruction process is the determination of the interaction point (or points, for multiple interactions). For trigger processing, data from the Level-0 system are used to form a rough measurement of the interaction point. For offline processing, central detector data are used to form a more accurate measurement of the vertex position.

The determination of the z position of the vertex is usually performed using data from the Central Drift Chamber (CDC). For each event, full tracking is performed on the CDC data. The tracking process proceeds in three steps: hit-finding, segment-finding, and finally, track-building.

In the hit-finding process, the raw data are unpacked from the CDD2 bank, and a hit-finding algorithm [55] is applied to the unpacked digital signal. For each hit that is found, a time and a pulse area is determined. For anode wires, the time is converted into a drift distance; for delay lines, the time is converted into a position along the delay line (in z), and the hit is associated with a hit on the adjacent anode wire, providing a three-dimensional measurement.

The segment-finding process connects the hits together, within a single layer. Only the $r - \phi$ position of the hits is used to find the segments; the z information is added to the segment afterwards. A road method is used to find the segments. A road is defined by a pair of hits (one from an inner wire and one from an outer wire) that span the sector (or nearly span the sector, to allow for a small hit-finding inefficiency). The roads are straight, since there is no central magnetic field; also, the roads are constrained to be nearly radial, since the tracks originate from the beam-spot at the origin, and there is very little multiple scattering due to the small amount of material in the radial direction. The width of the road is chosen to retain full efficiency while minimizing the number of fake segments; a road width of roughly 5 times the single-hit resolution was used. All hits on intermediate wires within the road are considered for the potential segment. The combination of hits that give the straight-line fit with

the smallest χ^2 is found; if that χ^2 is small enough and enough hits are included in the fit (hits from a minimum of 5 out of the 7 wires in a given sector must be included), a segment is formed. At the segment-building level, the χ^2 cut is fairly loose ($\chi^2/\text{degree-of-freedom} < 10$), in order to find segments with high efficiency. The segment-finding process is applied to all four CDC layers, and all segments that are found are stored for use in building tracks.

The procedure for linking segments into tracks is straightforward. In order to be linked, two segments must fall along the same line: they must point in the same direction, and the distance between their intercepts on the perpendicular bisector between the centers of gravity of the two segments must be small. A final straight line fit is performed using all the hits from the linked segments; if the fit is good enough, a track is formed. In general, a CDC track must include segments from at least three (out of four) layers; in the higher eta regions where the track leaves the end-plate of the CDC, two layer tracks are allowed.

To find the z position of the interaction vertex or vertices, each of the CDC tracks is projected to the beam-line, and the resulting position is stored in a histogram. The histogram is then searched for clusters, where each cluster defines an interaction point. In general, three tracks are required to define a cluster; for a single interaction event, however, a single track is sufficient to define the cluster. For each cluster, a z position is determined by averaging the projections from all the tracks contained in the cluster; a vertex position is recorded for each cluster. For high multiplicity clusters, the resolution of the measured vertex is about 6 mm; for single-track clusters, however, the resolution grows to about 2 cm [56]. For events with more than one vertex, the cluster associated with the highest track multiplicity is used as the primary vertex. The distribution of the vertex z position for the $W \rightarrow e\nu$ sample is shown in Figure 3.1. The distribution is centered at -8.6 cm, with an rms spread of 27 cm.

If the CDC fails to find a vertex, the same procedure is carried out using data from the Forward Drift Chamber (FDC). Finally, if the FDC also fails to find a vertex, the vertex chamber (VTX) is used. Overall, the vertex-finding procedure was 100 %

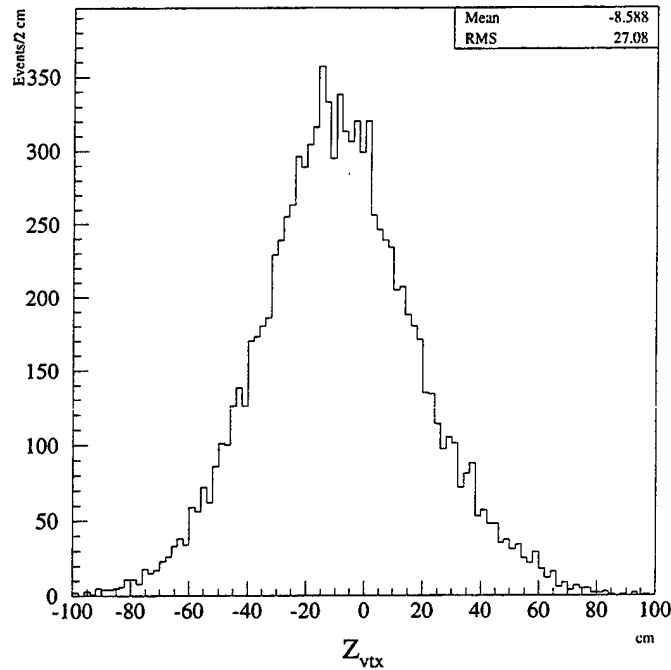


Figure 3.1: Distribution of the z position of the interaction vertex.

efficient for the events used in this analysis. The CDC successfully finds a vertex for roughly 95 % of all processed events; the remaining 5 % is handled by the FDC. The VTX was not used to determine the z vertex for any events used in this analysis.

The transverse (x, y) position of the beam is not measured on an event-by-event basis. The beam spot was monitored on a store-by-store basis using the vertex chamber data; the position of the beam spot was very stable, with few exceptions, and no correction was made to account for the movement. It is worth noting that the beam was not perfectly centered in the detector; the offset was several millimeters. This was noticeable in the detector data, but had negligible effect on the physics analysis.

3.1.4 Calorimeter Hit-finding

After the vertex position is determined, the calorimeter data are processed. First, the raw data are decoded: for each channel that passed the zero suppression, the

address bits are converted to the physical indices in the calorimeter (ieta and iphi identify the calorimeter tower, and ilyr identifies the depth of the calorimeter cell in question), and the digitized energy is expressed in terms of GeV. All appropriate corrections are applied, including run-dependent gain corrections from the calibration described above, absorber thickness corrections and a factor for sampling fraction. This energy conversion can be expressed as follows [57]:

$$E_{cell}(e, p, \ell) = F(m) \cdot SF(e, \ell) \cdot C(e, p, \ell) \cdot G(e, p, \ell) \cdot ADC(e, p, \ell) \quad (3.1)$$

where E_{cell} is the cell energy in GeV, e , p and ℓ are the calorimeter physical indices ieta, iphi and ilyr, respectively. F is an overall conversion constant which is different for each module type m ; it contains the conversion from adc counts to GeV, as well as any needed high voltage correction. SF is the sampling fraction, which provides the proper weighting for each layer of the calorimeter in order to give the best energy measurement. C contains the non-run-dependent (such as absorber thickness) corrections, G contains the run-dependent electronic gain corrections, and finally ADC is the digitized cell energy in adc counts. There are five different module types (m): central calorimeter (CC), end-cap calorimeter (EC), inter-cryostat device (ICD), CC massless gaps (CCMG), and EC massless gaps (ECMG).

Next, the cell energy is broken down into spatial components. The angle θ between the $+z$ axis and the line connecting the cell and the interaction point is calculated using the known position of the calorimeter cell and the z position of the vertex; the azimuthal angle ϕ is calculated just using the x and y positions of the calorimeter cell. Using these angles, it is easy to calculate the individual energy components, as well as the transverse energy:

$$E_x = E \sin \theta \cos \phi \quad E_y = E \sin \theta \sin \phi \quad E_z = E \cos \theta \quad (3.2)$$

$$E_T = E \sin \theta \quad (3.3)$$

The final step of calorimeter hit-finding consists of summing the energies for all

the cells in each (ieta,iphi) tower. This entails summing over the layer index, ilyr, for each pair of tower coordinates. For towers that are near the cryostat boundaries, this sum includes contributions from the massless gaps and the ICD. A separate sum is performed for the total energy and the electromagnetic (EM) energy; the EM energy includes the four layers of the electromagnetic calorimeter as well as the first layer of the fine hadronic (FH) calorimeter just behind it. For the EM calorimeter, the ilyr index runs from 1 through 7 (the finer subdivision in the third EM layer takes up ilyr indices 3 through 6); the first layer of the FH is ilyr 8. The energy sums for a given calorimeter tower (ieta,iphi) are then:

$$E_{tower}^{TOT}(e, p) = \sum_{\ell=1}^{17} E_{cell}(e, p, \ell) \quad (3.4)$$

$$E_{tower}^{EM}(e, p) = \sum_{\ell=1}^8 E_{cell}(e, p, \ell) \quad (3.5)$$

The energy and all of its spatial components (including the transverse energy) is stored for each tower sum. These tower energies form the basis for all cluster-finding algorithms.

3.1.5 \cancel{E}_T Calculation

Missing E_T is used to indicate the presence of a neutrino, or another similarly non-interacting particle. Due to the hermeticity and cylindrical symmetry of the DØ detector, conservation of momentum dictates that all transverse momenta should balance out, within the measurement resolution. A transverse momentum imbalance implies the presence of a non-interacting particle.

The $\vec{\cancel{E}}_T$ vector is defined so that it exactly cancels out the total transverse energy vector measured in the calorimeter. The calculation is done using the spatial x and y components of the calorimeter energies; the individual cell energies form the basis for the sums:

$$\cancel{E}_x = - \sum_{e,p,\ell} E_x(e,p,\ell) \quad (3.6)$$

$$\cancel{E}_y = - \sum_{e,p,\ell} E_y(e,p,\ell) \quad (3.7)$$

$$\vec{\cancel{E}}_T = \hat{n}_x \cancel{E}_x + \hat{n}_y \cancel{E}_y \equiv \begin{pmatrix} \cancel{E}_x \\ \cancel{E}_y \end{pmatrix} \quad (3.8)$$

where e , p and ℓ are the physical calorimeter indices ieta, iphi and ilyr as before, and \hat{n}_x and \hat{n}_y are unit vectors in the x and y directions respectively. The scalar quantity \cancel{E}_T is just the magnitude of this vector; another useful quantity is the azimuthal direction of $\vec{\cancel{E}}_T$:

$$\phi_{\cancel{E}_T} = \arctan \left(\frac{\cancel{E}_y}{\cancel{E}_x} \right) \quad (3.9)$$

Three different versions of the \cancel{E}_T are calculated. The first version forms the transverse energy sum of the calorimeter cells only. The second version includes corrections from the massless gaps and the ICD. Finally, after the muon reconstruction has been performed, a third version of the \cancel{E}_T is calculated which includes the muon momenta in the momentum balance. The calculated data for each version of the \cancel{E}_T are stored in a ZEBRA bank named PNUT (the names for all “particle”-type ZEBRA banks start with ‘P’).

3.1.6 Electron and Photon Definition

Both electrons and photons are characterized by narrow concentrated clusters of energy in the calorimeter, where nearly all of the energy is deposited in the electromagnetic section, which is closest to the interaction point. In addition, the charged electron has a particle track pointing from the interaction point to the energy cluster; the neutral photon leaves no trace in the tracking chambers.

The identification of electrons and photons starts with locating clusters of energy in the calorimeter. A nearest-neighbor (NN) cluster-finding algorithm is used [58], based

on the energy (not E_T) in the electromagnetic towers. In the NN algorithm, each tower is connected to the neighboring tower with the highest energy, if that energy is above a threshold, which is typically 50 MeV; only the eight towers immediately surrounding the tower are considered. The set of two-tower connections, taken as a whole, define clusters of mutually linked towers within the calorimeter; unlike some other algorithms (such as the cone algorithm, described later with respect to jet finding), there is no sharing of towers between clusters: a tower is included in one and only one cluster.

Once all the electromagnetic energy clusters have been found, their properties are used to determine whether they form the basis of either electrons or photons. First of all, the energy of the clusters must be greater than 1.5 GeV. Next, at least 90 % of the cluster energy must be electromagnetic (contained in EM layers 1-4 and FH layer 1). Finally, the transverse profile in the η direction must be such that at least 40 % of the cluster energy is contained within towers with the same ieta index as the hottest tower. If a cluster passes all these criteria, it will form the basis for either a photon or an electron. For these clusters, the cluster centroid is calculated by forming a weighted mean of the coordinates of the EM3 cells contained in the cluster [59]:

$$\vec{x}_{clus} = \frac{\sum_i w_i \vec{x}_i}{\sum_i w_i} \quad (3.10)$$

where \vec{x}_i is the position of the center of cell i . The weights w_i are based on the logarithm of the cell energy E_i :

$$w_i = \max\left(0, w_0 + \ln\left(\frac{E_i}{E_{clus}}\right)\right) \quad (3.11)$$

where w_0 is chosen to optimize the position resolution. The logarithmic weighting scheme is motivated by the exponential profile of the shower.

The cluster energies and angles are also calculated:

$$E_i^{clus} = \sum_{k=1}^{ncells} E_i^k \text{ where } E_i = E, E_x, E_y, E_z \quad (3.12)$$

$$E_T^{clus} = \sqrt{\left(\sum_k E_x^k\right)^2 + \left(\sum_k E_y^k\right)^2} = \sqrt{(E_x^{clus})^2 + (E_y^{clus})^2} \quad (3.13)$$

$$\phi^{clus} = \arctan\left(\frac{E_y^{clus}}{E_x^{clus}}\right) \quad (3.14)$$

$$\theta^{clus} = \arccos\left(\frac{E_z^{clus}}{\sqrt{(E_x^{clus})^2 + (E_y^{clus})^2 + (E_z^{clus})^2}}\right) \quad (3.15)$$

$$\eta^{clus} = -\ln \tan\left(\frac{\theta^{clus}}{2}\right) \quad (3.16)$$

For the cluster to be considered an electron, there must be a track in the central detector in the road defined by the cluster position and the primary vertex position. The azimuthal road size is ± 0.1 radians; the road size in θ is determined as follows:

$$\tan \theta_{\pm} = \min(r_{clus}/(z_{clus} - z_{vtx} \pm 5\delta z), 0.1) \quad (3.17)$$

where $r_{clus} = \sqrt{x_{clus}^2 + y_{clus}^2}$, x_{clus} , y_{clus} and z_{clus} are the cluster coordinates, and z_{vtx} is the z coordinate of the primary vertex, and δz is the error on the vertex measurement. There is some photon background in the electron sample, due to fake track matches; the contamination before any further quality cuts on the electrons is $3.1 \pm 0.8\%$ in the CC and $17.4 \pm 1.6\%$ in the EC [60]. Distributions of the residuals of the match between the calorimeter cluster centroid and the projected track are shown in Figure 3.2.

The calculated data for “photon” clusters are stored in PPHO banks; similarly, the calculated data for “electron” clusters are stored in PELC banks, which includes pointers to all matching central detector tracks in the road corresponding to the cluster.

3.1.7 Tracking in Roads

Due to processing time constraints, full tracking is not done for all of the central detector drift chambers. This limitation usually only applies to the FDC and the VTX reconstruction, since full tracking is done in the CDC in order to determine z_{vtx}

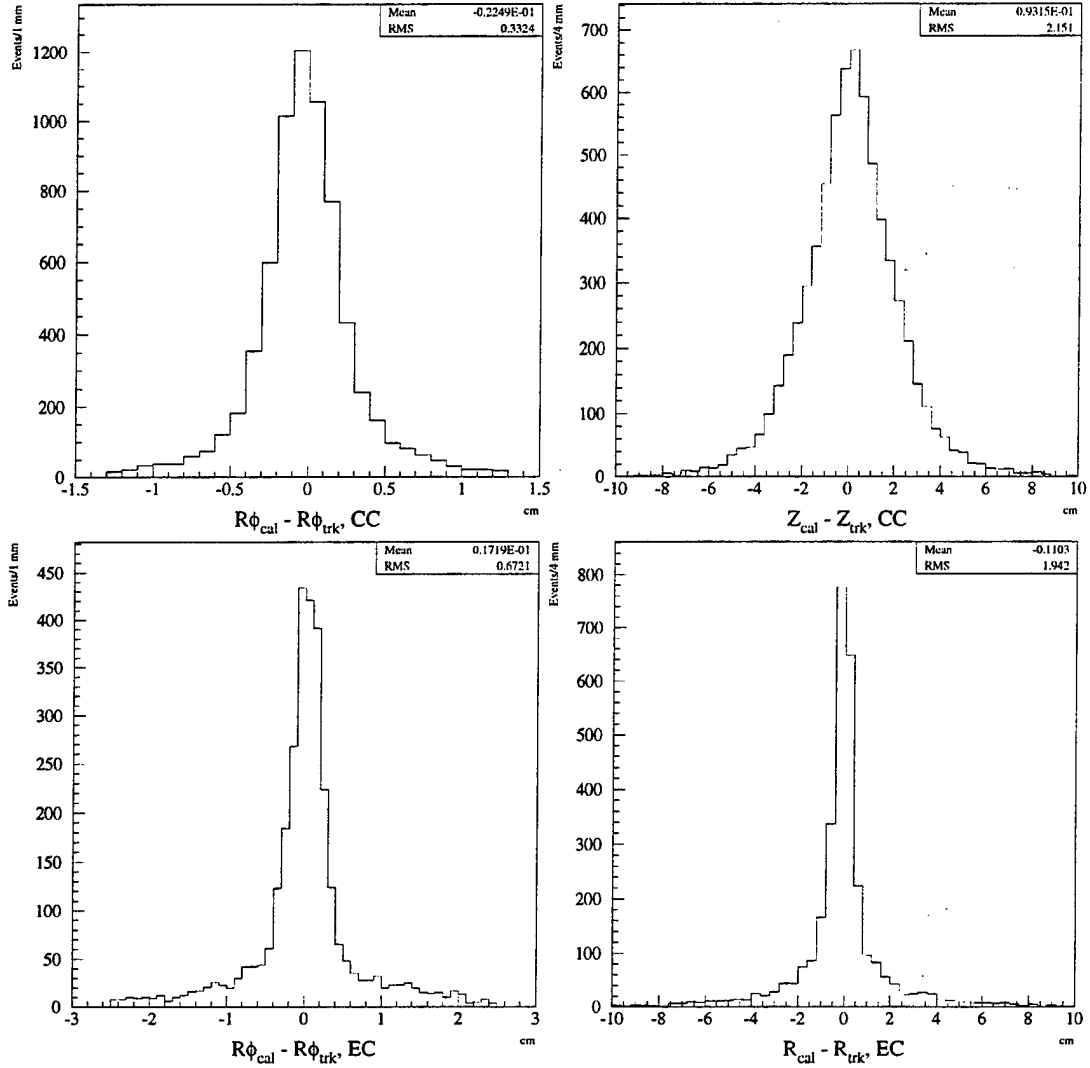


Figure 3.2: Distributions of residuals between the calorimeter cluster centroid and the projection of the matched Central Detector track. In the CC (which has barrel geometry), the residuals are in $R\Delta\phi$ (where R is constant) and Δz ; in the EC (which is a flat disk at constant z), the residuals are in $r\Delta\phi$ (r varies) and Δr .

(full tracking is also done in the FDC for the small fraction of events in which the CDC fails to provide the vertex information).

For tracking in roads, a road in ϕ and θ is defined during the particle identification process for electrons or other charged particles. This road is passed to the tracking software for each sub-detector, which identifies what sectors or modules of the detector are within the road; the normal tracking process (described in detail above with respect to vertex determination) is applied to those sectors or modules. Finally, tracks in the individual sub-detectors are linked (analogously to the linking of sectors) to form overall central detector tracks within the specified road. For each track, a global fit is performed using the coordinates of all the hits on the track. If a track is found within the specified road that meets the criteria of the particle algorithm which defined the road, then a pointer to the track information is stored as part of the particle description.

3.1.8 Jet-Finding

Any final state quarks or gluons produced by the physical interaction hadronize to form colorless jets of energy. The process of jet identification involves both finding these jets within the calorimeter, as well as relating the measured jet properties to the original parton.

Since the cross section analyses being described here are inclusive (any number of jets can accompany the W or Z production), the specifics of the algorithm used for finding jets do not have a direct effect on the results. However, the calculation of the final \cancel{E}_T (described later) involves jet energy corrections, so a brief description of the jet definitions is presented.

Several jet-finding algorithms are implemented in the $D\bar{O}$ reconstruction. One jet definition uses a nearest-neighbor algorithm similar to that used to find electrons and photons to identify the jets. In addition, there are three jet definitions based on a fixed-cone algorithm for finding the jets. These definitions differ only in the cone size

used; the three cone sizes, in \mathcal{R} space (where $\mathcal{R} = \sqrt{(\Delta\eta)^2 + (\Delta\phi)^2}$, and $\Delta\eta$ and $\Delta\phi$ are measured from the shower centroid), are 0.3, 0.5 and 0.7. The jet definition used for this analysis is based on the 0.7 cone size.

The cone algorithm is based on the total tower energies, not just the electromagnetic energy as in the case of finding electrons. The algorithm starts with a list of towers ordered from the highest to the lowest in E_T ; any tower with transverse energy greater than 1.0 GeV can be used as a jet seed. Preclusters are formed from the seed towers, where all the contiguous towers are connected, up to a maximum size of ± 0.3 units in η and ϕ around the tower in the cluster with the highest E_T . The preclustering continues until all of the seed towers are used; in some cases, a precluster will contain only a single tower. Then for each precluster (beginning with the precluster with the highest transverse energy), the centroid in (η, ϕ) is calculated, weighting each tower by its transverse energy; the jet axis is defined by the interaction vertex and this centroid. All towers within a radius \mathcal{R} of the centroid are identified, and included in the jet. Then a new centroid is calculated, and the process is iterated until the centroid is stable.

After the jet for each precluster is found (except for the first jet), the jet axis is compared to the jet axes of all the previously found jets. Often, the same jet is found from more than one precluster; if the jet axis of the newly found jet coincides with a previously found jet (within 0.01 units in $\eta \times \phi$), then the new jet is discarded. If the new jet shares energy with a previously found jet, then the two jets are either merged or split, depending on how much energy is shared. If the shared energy is greater than half of the energy of the less energetic jet, the two jets are merged, and a new jet axis is calculated. Otherwise, the shared calorimeter cells are split on the basis of distance to each jet axis; once again, the centroids are recalculated after the splitting process is complete. Once the clustering process is complete, the kinematic properties of the jet are determined by summing over the towers contained within the jet, and the jet axis is then calculated using the energy components. The energy components are calculated in an analogous manner to the electromagnetic cluster energies, with

the exception of the transverse energy. For the jets, whose showers are in general much larger than the compact electron or photon showers, the transverse energy is the sum of the transverse energies calculated separately for each tower in the jet; recall that for the electromagnetic clusters, the transverse energy is calculated based on the summed component energies. Specifically,

$$E_T^{jet} = \sum_{k=1}^{ntowers} E_T^k = \sum_{k=1}^{ntowers} \sqrt{(E_x^k)^2 + (E_y^k)^2} \neq \sqrt{\left(\sum_k E_x^k\right)^2 + \left(\sum_k E_y^k\right)^2} \quad (3.18)$$

3.2 Particle Identification

The algorithms used in the reconstruction process to identify physical particles are tuned to perform with high efficiency, necessarily allowing a fair amount of background or fakes. Further cuts are applied as part of the analysis in order to reduce the number of fakes, while maintaining as high efficiency as possible. The W and Z bosons used for this cross section analysis decay into a pair of leptons, either two electrons or one electron and a neutrino. The methods used to identify these electrons and neutrinos (\cancel{E}_T) are described here.

3.2.1 Electron identification

Electrons and photons create a very compact shower in the calorimeter, with almost all of the energy concentrated in the electromagnetic section of the calorimeter (which is closest to the interaction point). The definition of an electron (or photon) employed by the reconstruction process takes advantage of this unique signature to some extent; in order to reduce the number of fake electrons, more stringent cuts are applied during the analysis that take into account more of the available calorimeter information. Furthermore, the quality of the track-match (for electrons) can be used to further reduce the background. Finally, due to the large momentum transfer in the W and Z events, the decay electrons tend to be very isolated (very little energy deposit close to the electron); this fact is used to reduce the background even further.

There are four variables that are used to cut down the background in the electron sample: H-matrix chi-squared (χ_{hm}^2), electromagnetic energy fraction (f_{em}), track-match significance (S_{trk}) and isolation fraction (f_{iso}). The definition of these variables is detailed below.

3.2.1.1 H-matrix chi-squared (χ_{hm}^2)

The shower caused by an electron moving through the calorimeter has a unique shape, both longitudinally (depth profile) and laterally. Electromagnetic showers in the DØ calorimeter have been studied extensively, using both test beam data and careful Monte Carlo simulation. The fractional energy deposit in each calorimeter cell in the shower depends on many things, including the electron energy, the depth of the shower maximum, and the impact position within the hit cell. The H-matrix chi-squared is designed to measure how closely an electromagnetic cluster resembles a true electron cluster, taking into account all correlations.

To take into account all possible correlations, a covariance matrix M is built from 41 observables: the energy fraction in EM layers 1, 2 and 4 of the hit cell, the energy fraction in each cell of a 6x6 grid in EM layer 3 centered on the most energetic cell, the logarithm of the cluster energy (in order to take into account the energy dependence) and finally the z position of the interaction vertex (to take into account the dependence on the angle of incidence). Since the detector geometry (transverse cell size) changes as a function of η , there are 37 different matrices M , one for each pseudorapidity tower in half the detector (the same matrix is used for the corresponding positive and negative η towers, with care taken to handle the vertex z position correctly).

The matrices are calculated using a large sample of Monte Carlo electrons. Each component of the covariance matrix is calculated in the following way for the sample of N reference electrons:

$$M_{ij} = \frac{1}{N} \sum_{n=1}^N (x_i^n - \bar{x}_i)(x_j^n - \bar{x}_j) \quad (3.19)$$

where x_i^n is the value of the i th observable for the n th reference electron and \bar{x}_i is the average value of the i th variable for the entire reference set. The reference electrons have energies in the range 10 to 150 GeV, as well as a wide range in z_{vtx} . These matrices were tested on test beam electrons in order to ensure that the Monte Carlo reference electrons adequately described real data.

The H-matrix is the inverse of the covariance matrix; $H = M^{-1}$. For a candidate electron, the H-matrix chi-squared is calculated:

$$\chi_{hm}^2 = \sum_{i,j=1}^{41} (x_i^c - \bar{x}_i) H_{ij} (x_j^c - \bar{x}_j) \quad (3.20)$$

where x_i^c is the value of the i th observable for the candidate electron. The value of χ_{hm}^2 indicates how closely the cluster shape of the candidate electron resembles that of an electron; a clean well-measured electron has a very low χ_{hm}^2 . Note that the distributions for the observables x_i^c are in general non-Gaussian, so χ_{hm}^2 does not follow a 'true' χ^2 distribution; nevertheless, the H-matrix parameter offers strong rejection against electron background.

3.2.1.2 Electromagnetic energy fraction (f_{em})

The standard definition for both an electron and a photon demands that at least 90 % of the cluster energy must be contained within the electromagnetic section of the calorimeter. For electrons such as those in the W and Z events under study, that requirement is very loose. A significant amount of added rejection is obtained by cutting more tightly on f_{em} .

3.2.1.3 Track-match significance (S_{trk})

As mentioned previously, the definition of an electron requires the existence of a central detector track within a road defined by the vertex position and the cluster centroid. Due to high occupancy in the tracking chambers, it is possible that a track within the road might not be related to the electromagnetic cluster. As a result, it is

possible for an uncharged photon (possibly originating from a converted π^0) to fake an electron. In order to reduce this background source, a cut is made on the quality of the match between the track and the cluster centroid.

The variable used to judge the quality of the track-cluster match is the track-match significance, S_{trk} . To calculate S_{trk} , the track is projected into the calorimeter, and the distance between the projection and the cluster centroid is determined in both directions (Δz and $\Delta\phi$ in the CC, Δr and $\Delta\phi$ in the EC; note that $\Delta\phi$ is the spatial distance, not the angular discrepancy). The track match significance in the central calorimeter is then

$$S_{trk}^{CC} = \sqrt{\left(\frac{\Delta\phi}{\sigma_\phi}\right)^2 + \left(\frac{\Delta z}{\sigma_z}\right)^2} \quad (3.21)$$

where $\Delta\phi$ is the mismatch in the azimuthal direction, Δz is the mismatch along the beam, and σ_ϕ and σ_z are the corresponding measurement resolutions. Similarly for the end-cap calorimeter,

$$S_{trk}^{EC} = \sqrt{\left(\frac{\Delta\phi}{\sigma_\phi}\right)^2 + \left(\frac{\Delta r}{\sigma_r}\right)^2} \quad (3.22)$$

where $\Delta\phi$ is the azimuthal mismatch, Δr is the radial mismatch, and σ_ϕ and σ_r are the resolutions. The measurement resolutions include both the calorimeter position resolution and the track resolution (including extrapolation error).

3.2.1.4 Isolation fraction(f_{iso})

The cut on isolation fraction is more of an event topology selection than an electron identification cut. Electrons from the decay of W and Z bosons are expected to be isolated, since they are not produced in association with any other particles. Electrons from other physics processes are usually produced along with other particles nearby in η - ϕ space; for example, electrons from heavy quark leptonic decay are part of the QCD jet associated with that heavy quark. The isolation cut is really a selection on the *source* of the electrons; requiring the electrons to be isolated selects W and Z events with high efficiency, while rejecting other sources of real electrons.

The isolation cut requires that the energy contained within the annular region surrounding the core of the electromagnetic cluster be small compared to the electromagnetic energy within the core. The core cone size used is $\mathcal{R} = 0.2$; the surrounding isolation cone size is $\mathcal{R} = 0.4$. Specifically, the following definition is used for the isolation variable:

$$f_{iso} = \frac{E_{tot}(0.4) - E_{em}(0.2)}{E_{em}(0.2)} \quad (3.23)$$

where $E_{tot}(\mathcal{R})$ is the total energy within a radius \mathcal{R} from the cluster center, and similarly for $E_{em}(\mathcal{R})$.

Distributions of the electron identification variables χ_{hm}^2 , f_{em} , S_{trk} and f_{iso} are shown in Figure 3.3 for a clean sample of CC electrons, and in Figure 3.4 for a clean sample of EC electrons. Similar distributions for a background-rich sample are shown in Figure 3.5.

3.2.2 Neutrino Identification (\cancel{E}_T)

In addition to having a clean electron, the W boson events have a neutrino which must be inferred from an imbalance in the transverse energy deposited in the calorimeter. The magnitude of this imbalance, \cancel{E}_T , is taken to be the p_T of the neutrino.

The cell-by-cell calculation of the \cancel{E}_T has already been described. As part of many analyses, energy corrections are applied to various physics objects, such as electrons or jets. These corrections must be incorporated into the calculation of the \cancel{E}_T . For any analysis that uses \cancel{E}_T as a selection criteria, it is important to clearly define the energy corrections applied and how they are incorporated into the \cancel{E}_T calculation. The W cross section analysis described here incorporates corrections to both the signal electron as well as any additional jets.

The standard electromagnetic correction is applied to the signal electron only; any other electrons or photons are part of the underlying event and are corrected as jets. The electromagnetic correction is determined by studying a clean sample of $Z \rightarrow ee$ events, and comparing the fitted Z boson mass with the precise LEP value;

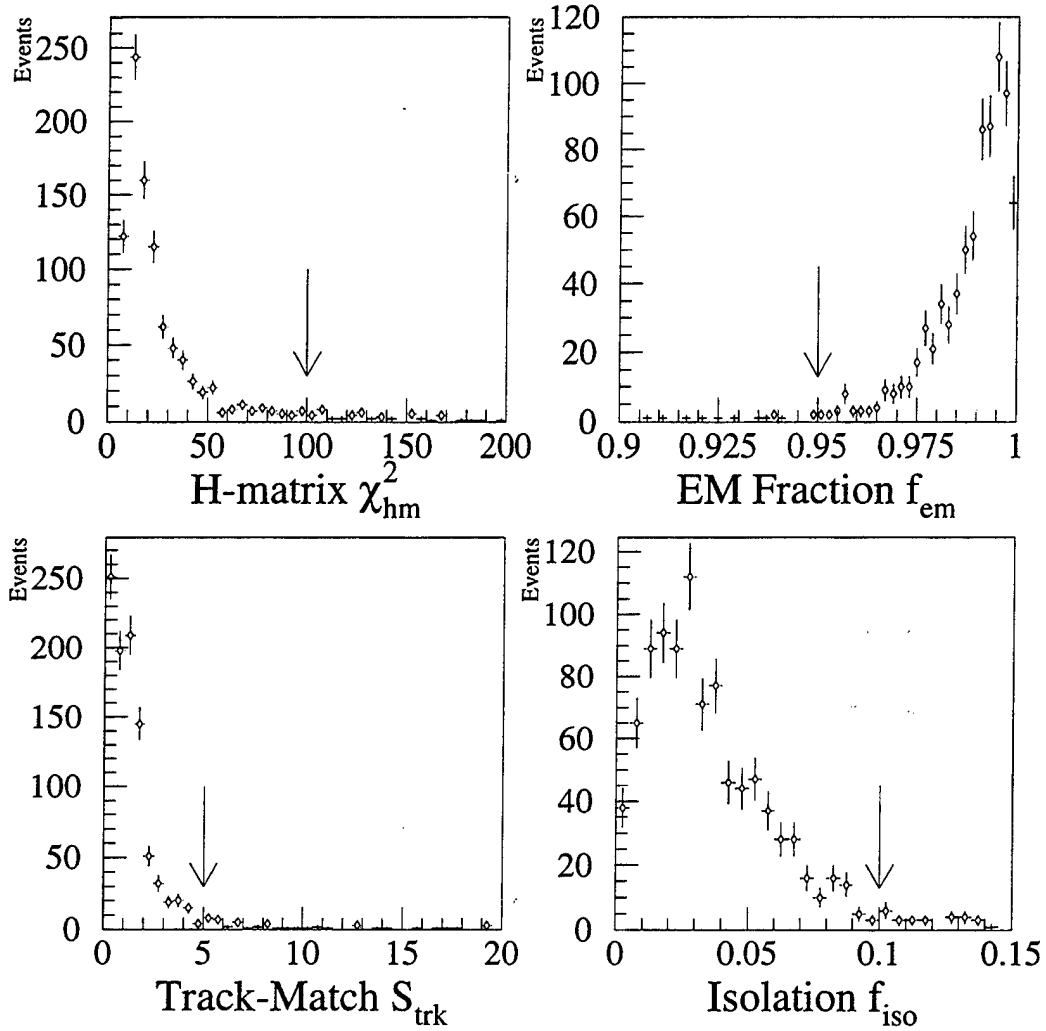


Figure 3.3: Distributions of the electron identification variables χ^2_{hm} , f_{em} , S_{trk} and f_{iso} for a sample of CC electrons with little background, obtained by selecting the “second” electron of a diagnostic sample of $Z \rightarrow ee$ events. Tight cuts are made on the primary electron, so no electron identification cuts are made on the secondary electron; if both electrons pass the tight cuts, the event is used twice in the sample above. These plots only include events in the invariant mass range 86 to 96 GeV centered on the Z boson mass, in order to minimize the background fraction in the sample. The arrows indicate the values used to cut on each variable.

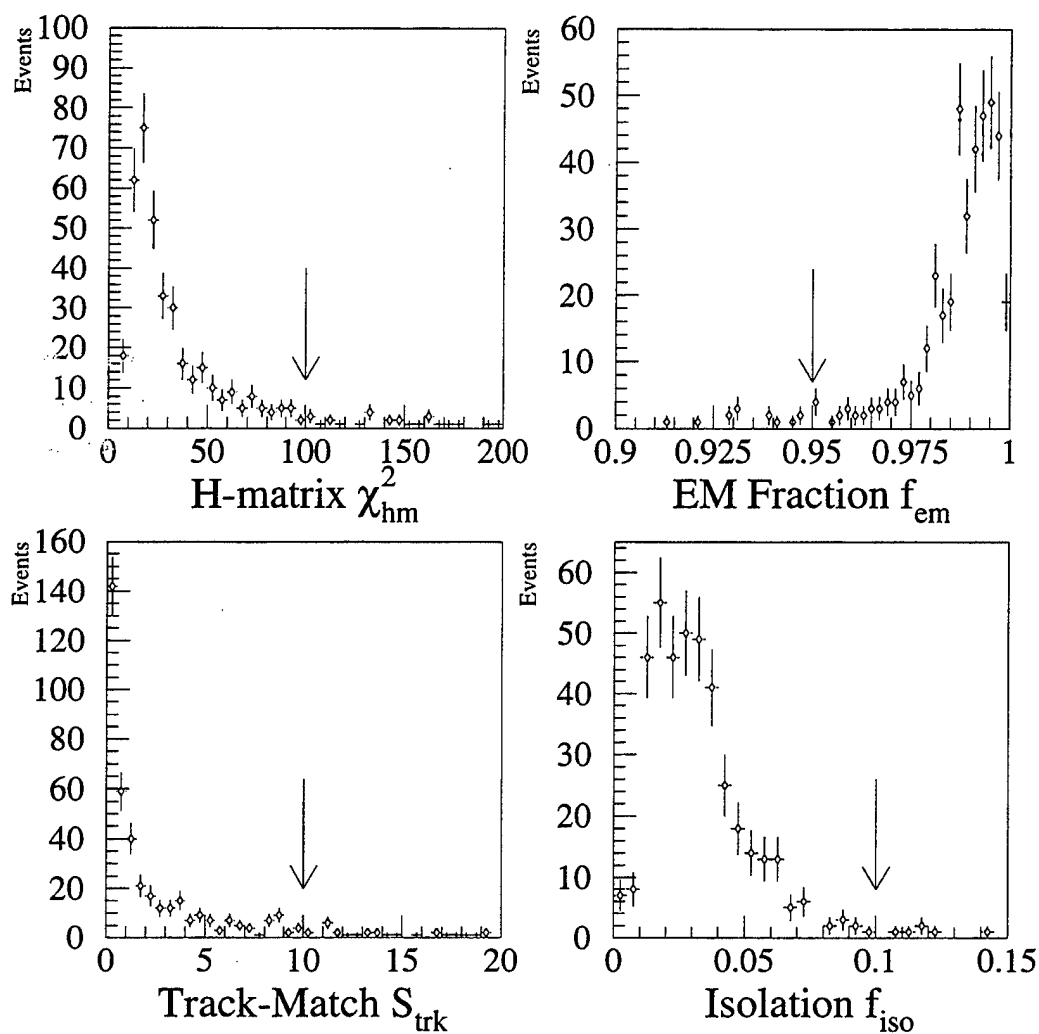


Figure 3.4: Distributions of the electron identification variables for a clean sample of EC electrons; the same method was used to select the sample as described in the caption of Figure 3.3. The arrows indicate the values used to cut on each variable.

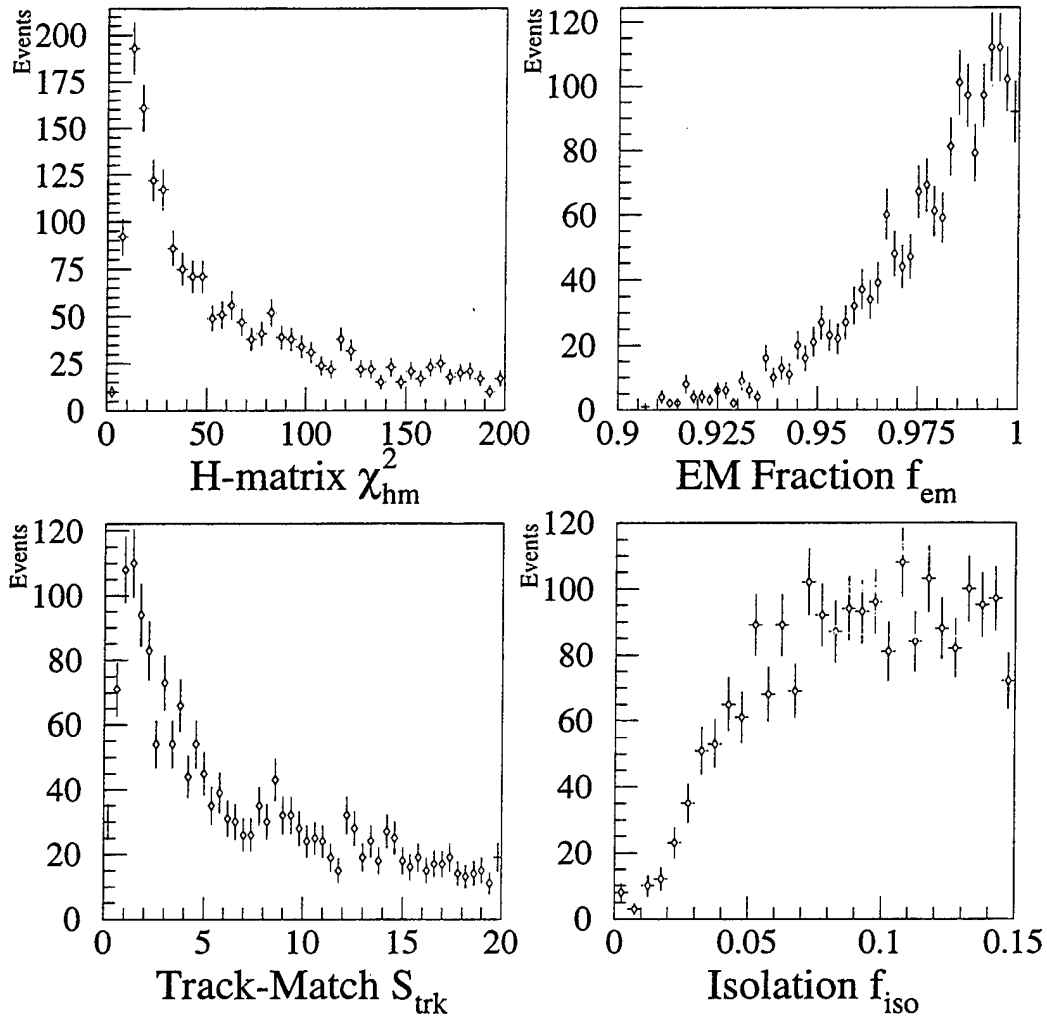


Figure 3.5: Distributions of the electron identification variables for a sample of CC “electrons” which contains significant background. Electrons in this sample were only required to pass a loose set of Level-2 filter cuts and meet the requirements to form a PELC bank (including a track-match).

Cryostat	Correction Factor
CC	1.072
EC South	1.012
EC North	1.025

Table 3.2: Standard electromagnetic correction factors for each cryostat

by sorting the diagnostic events by cryostat combinations, a separate correction value is obtained for each of the three cryostats. The correction values used are summarized in Table 3.2; the underlying reasons for this miscalibration are discussed elsewhere [61].

Next, the jet energies are corrected, using cone-algorithm jets with a radius of 0.7 in $\Delta\eta - \Delta\phi$ space; the jet corresponding to the signal electron is excluded. The standard default correction (as defined by QCD-JET-CORRECTION [62] version 4.0) was applied.

The calculation of the missing transverse energy starts with the calorimeter-based \cancel{E}_T , including ICD and massless gap corrections (version 2 of the PNUT bank, described above). The scalar quantity \cancel{E}_T and the azimuthal angle $\phi_{\cancel{E}_T}$ are used to calculate the x and y components of the missing transverse energy. As each energy correction is calculated, the transverse components of the correction are also calculated, and subtracted from the components of the \cancel{E}_T (recall that $\vec{\cancel{E}}_T = -\vec{E}_T^{tot}$). The corrected components of the missing transverse energy incorporate all the energy corrections applied to the electron and jets:

$$\cancel{E}'_x = \cancel{E}_x + \sum_i \Delta E_x^i \quad (3.24)$$

$$\cancel{E}'_y = \cancel{E}_y + \sum_i \Delta E_y^i \quad (3.25)$$

$$\cancel{E}'_T = \sqrt{(\cancel{E}'_x)^2 + (\cancel{E}'_y)^2} \quad (3.26)$$

$$\phi'_{\cancel{E}_T} = \arctan\left(\frac{\cancel{E}'_y}{\cancel{E}'_x}\right) \quad (3.27)$$

where \cancel{E}'_x , \cancel{E}'_y , \cancel{E}'_T and $\phi'_{\cancel{E}_T}$ are the corrected quantities related to the missing transverse energy, and the sums run over all the applied energy corrections. The W selection applies a cut to the scalar \cancel{E}'_T in order to identify the presence of a neutrino.

Chapter 4

W and Z Data Samples

This analysis is based on data from the first run at DØ, known as Run 1A. The first $p\bar{p}$ collisions at DØ were observed in May, 1992; Run 1A ended in May of 1993. DØ used the first three months of collider operation as an engineering run in order to become proficient at running the detector; in general, the luminosities were very low during this period. Data taking for physics began in earnest after a brief shutdown in August 1992; a total of approximately 15 pb^{-1} of data was taken between that time and the end of the run in 1993.

Nearly all of the physics data was used for the W and Z cross section analyses; a small amount of early data was left out due to a high Level-1 trigger threshold. In this chapter, the event selection is described, including the trigger requirements. The efficiency and the acceptance of the selection criteria are also presented. Finally, the types and amount of background for the W and Z events are studied.

4.1 Event Selection

The events used for these cross section analyses are selected on the basis of having two leptons, either two electrons for the $Z \rightarrow ee$ events or one electron and a neutrino for the $W \rightarrow e\nu$ events. The selection is made in two stages: trigger and offline. Fairly

loose cuts are made at the trigger level, which reduce the volume of data written to tape to an acceptable level; the use of a specific trigger also makes the integrated luminosity used for the analysis easily calculable. The offline selection is used to optimize the signal to background ratio, so that the final data sample is as large as possible to minimize the statistical errors while still retaining an acceptably small (and reliably measurable) level of background contamination.

4.1.1 Trigger Requirements

The same single-electron trigger is used for both the W and Z events; no requirements are made for a second lepton at the triggering stage. In addition to the universal Level-0 minimum bias trigger requirement (which just requires both Level-0 counter arrays to be hit), the selection requirements focus on identifying events with at least one isolated, high p_T electron.

For most of the run, the Level-1 specific trigger used to select the W and Z events required $E_T^{em} > 10$ GeV for at least one trigger tower; for a small amount of early data, the trigger threshold was 12 GeV. For the offline E_T cut of 25 GeV used in the analysis, both the 10 and 12 GeV cuts are fully efficient so there is no loss of acceptance; the acceptance of the offline cut is discussed later in this chapter. A small amount of very early data used a threshold of 14 GeV; these runs were excluded from the analysis. This trigger was very rarely prescaled.

The Level-2 filter used as the basis for the events used in this analysis was named ELE.HIGH. The filter required an electromagnetic energy cluster with $E_T^{em} > 20$ GeV, based on the simplified clustering schemes used in the Level-2 system. In addition, loose shower shape cuts were applied to the cluster, requiring the cluster to look like an electron in both the longitudinal and lateral directions. Finally, an isolation cut was applied to the candidate cluster:

$$f_{iso} = \frac{E_{tot}(\mathcal{R}_{iso}) - E_{em}(\mathcal{R}_{core})}{E_{em}(\mathcal{R}_{core})} < 0.15 \quad (4.1)$$

where \mathcal{R}_{iso} and \mathcal{R}_{core} are the isolation and core cone sizes, respectively, in the $\eta - \phi$ space. Both cones center on the EM3 cell with the highest energy; the core cone size was $\mathcal{R}_{core} = 0.2$. Two different isolation cone sizes were used during the run (the cone sizes were changed in order to control the bandwidth coming out of Level-2); roughly half of the data used $\mathcal{R}_{iso} = 0.4$, and the other half used $\mathcal{R}_{iso} = 0.6$ (note that the larger isolation cone size corresponds to a tighter cut).

4.1.2 Offline Electron Selection

The events that passed the Level-2 filter were written to tape, and then processed through RECO, which processes the data and identifies electrons, photons, muons and jets. This analysis uses two subsequent sets of cuts to define the signal electrons, a loose selection and a tight selection, where the loose cuts form a subset of the tight cuts. The fiducial regions used to select the electrons was chosen to eliminate regions where the detector response is poor; these include the inter-cryostat region, the very-forward regions surrounding the beam-pipe, and the cracks between the 32 CC EM modules. The same fiducial region was used for the tight and loose selections:

- Central Calorimeter: $|\eta_{ele}| \leq 1.1$, $|\phi_{ele} - \phi_{crack}| > 0.01$. Note that for electrons (PELC banks), the ϕ of the associated track is used to make the crack cut; for photons (PPHO banks), the calorimeter ϕ is used. The crack cut represents a 10 % loss in acceptance in the CC region.
- End-cap Calorimeters: $1.5 \leq |\eta_{ele}| \leq 2.5$

The loose electron selection uses only calorimeter data; no track-match is required (so both PELC banks and PPHO banks are accepted). This avoids the significant loss of efficiency caused by requiring a matching track, at the expense of a significant increase in background. The cuts used to define the loose selection are summarized below; note that the actual cuts applied to the calorimeter-based electron-identification variables are the same as used in the tight selection:

- PELC or PPHO bank
- $\chi_{hm}^2 < 100$ (both CC and EC)
- $f_{em} > 0.95$
- $f_{iso} < 0.10$

For the tight selection, tracking and trigger information is used to cut down the background and provide a clean sample of electrons. The cuts that define the tight selection are listed below:

- PELC banks only (no PPHO banks – track-match *is* required)
- Same calorimeter electron-identification as loose selection
- Good track-match: $S_{trk} < 5.(10.)$ in the CC(EC)
- Corresponds to EM energy cluster that passed the ELE_HIGH Level-2 filter

4.1.3 W and Z Boson Data Samples

The selection of the W and Z boson data samples took place in several steps. The overall parent sample, roughly 13 million events, was the nearly complete set of Run 1A data reprocessed using version 11 of RECO. In order to create a data sample of manageable size, the ALL stream events were filtered to create an ELF (filtered electron) stream; an event was included in the ELF stream if it met any of the following criteria (note that for these selections, the energy scale corrections described previously are not yet applied):

- Loose W selection: 1 PELC (electron bank) or PPHO (photon bank) with $E_T > 15$ GeV, $\cancel{E}_T > 15$ GeV (based on version 2 of PNUT, which includes ICD and Massless Gap corrections, but no correction for muons)

- Loose Z selection: 2 PELCs or PPHOs (any combination) with $E_T > 10$ GeV. The looser kinematic cuts relative to the loose W selection were possible due to the relatively low background obtained by requiring two electromagnetic objects.
- Diagnostic events: any event that passed the ELE_MEDIUM Level-2 filter, which was a looser version of the ELE_HIGH filter used for this analysis (no isolation cut was made by the ELE_MEDIUM filter, and the transverse energy threshold is 16 GeV instead of 20 GeV).

Events from known bad runs were excluded from the ELF stream.

As defined above, the ELF stream contains about 470,000 events. This is still a large sample, too large to fit on disk (about 9 Gb). One more level of selection was applied to create a manageable sample which could be used repeatedly; at this point, the data was split into W and Z parent samples. The following cuts were used to select the $W \rightarrow e\nu$ parent sample (WEV stream):

- passed ELE_HIGH filter
- 1 PELC or PPHO with $E_T > 20$ GeV, no further electron-identification cuts
- $\cancel{E}_T > 15$ GeV (same as ELF requirement)

A total of 62,727 events passed these cuts.

The following cuts were used to select the $Z \rightarrow ee$ parent sample (ZEE stream); note that these cuts were chosen to be loose enough so the events could be used as a diagnostic sample:

- passed ELE_HIGH or ELE_2_MAX filter (which requires two clusters that pass the ELE_HIGH requirements)
- 2 PELCs or PPHOs (any combination) with $E_T > 20$ GeV

These cuts selected 14,244 events from the parent ELF sample.

The final W and Z boson samples were selected from the WEV and ZEE streams, respectively. For both selections, only data with run number 55217 or greater (trigger version 6.1 or greater) are used, since the Level-1 E_T threshold for earlier data was 14 GeV, which is not fully efficient for the offline E_T cut used. Less than 1 pb^{-1} of data are lost by cutting out the early runs. As mentioned above, known bad runs are also removed from the sample (as part of the ELF streaming); the luminosity lost is negligible.

The following cuts were used to select the final $W \rightarrow e\nu$ sample from the WEV stream (note that some cuts are repeated in order to list the entire set of cuts that define the W sample):

- Passed ELE_HIGH filter
- At least one z vertex found
- One tight electron with scale-corrected $E_T > 25 \text{ GeV}$ in the good fiducial region described earlier
- Corrected $\cancel{E}_T > 25 \text{ GeV}$
- Events with a second high p_T electron are excluded to minimize background from $Z \rightarrow ee$ events with mismeasured \cancel{E}_T

A total of 10,338 events passed these cuts; the selection is summarized in Table 4.1. The transverse mass distribution for the $W \rightarrow e\nu$ signal sample is shown in Figure 4.1. Distributions of p_T and η of the signal electron are shown in Figure 4.2, compared to the Monte Carlo prediction.

The cuts used to select the final $Z \rightarrow ee$ sample are detailed below:

- Passed ELE_HIGH filter
- At least one z vertex found
- One tight electron with $E_T > 25 \text{ GeV}$ in good fiducial region

$W \rightarrow e\nu$ Selection		$Z \rightarrow ee$ Selection	
Cut	Events Left	Cut	Events Left
WEV stream	62727	ZEE stream	14244
Run ≥ 55217	57545	Run ≥ 55217	12986
ELE_HIGH	57545	ELE_HIGH	12498
≥ 1 z vertex	57429	Tight electron, $p_t > 25$	3024
1 Tight electron, $p_t > 25$	13915	Loose electron, $p_t > 25$	907
$\cancel{E}_T > 25$ GeV	10338	$75 < M_{ee} < 105$ GeV	775
$W \rightarrow e\nu$ Signal Events	10338	$Z \rightarrow ee$ Signal Events	775
CC	7284	CC-CC	402
EC South	1440	CC-EC	296
EC North	1614	EC-EC	77

Table 4.1: Summary of signal event sample selection and fiducial breakdown

- One loose electron with $E_T > 25$ GeV in good fiducial region
- Invariant mass window: $75 < M_{ee} < 105$ GeV

The cut on invariant mass is used to reduce the amount of background in the sample, while keeping nearly all of the signal (the Drell-Yan background is much more significant at lower invariant mass). As long as the window limits are in the tails of the Z invariant mass peak, the effect of the cut is relatively insensitive to the specific values chosen, so the round numbers above were chosen for convenience.

These cuts select 775 events from the ZEE stream; without the invariant mass cut, 907 events pass. The event selection is summarized in Table 4.1; the invariant mass distribution is shown in Figure 4.1. The distribution of the p_T of the leading electron is shown in Figure 4.3 compare to the Monte Carlo prediction.

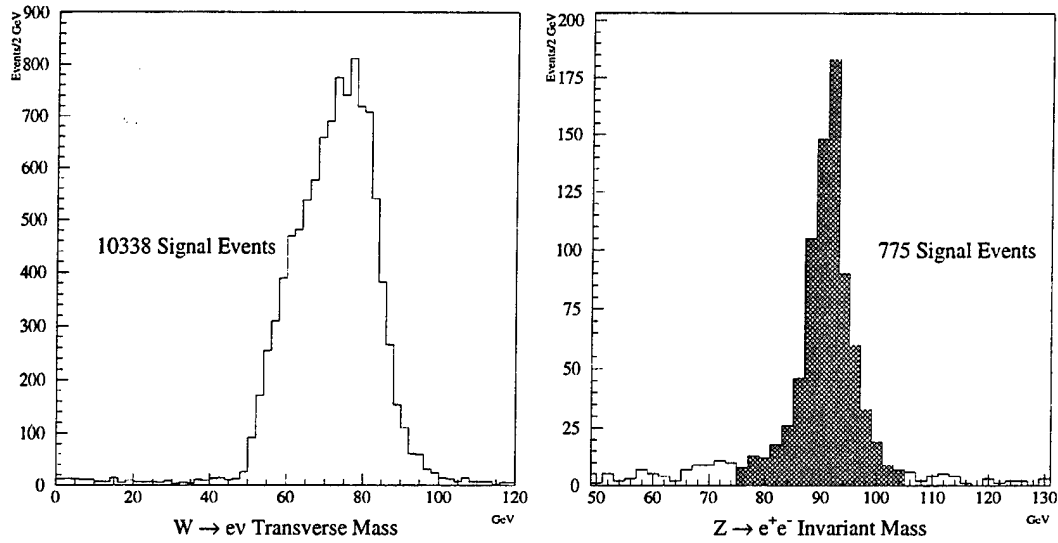


Figure 4.1: Mass plots for the W and Z signal samples.

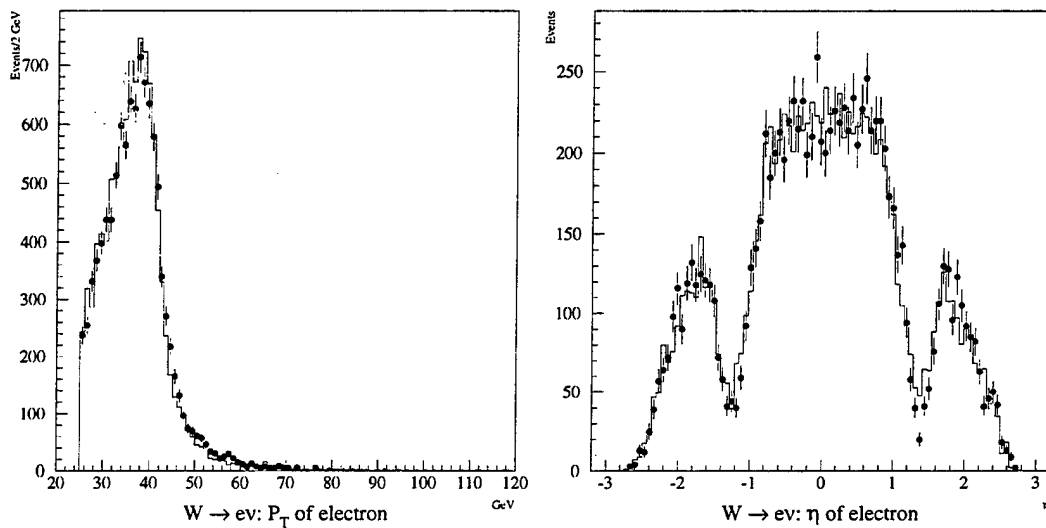


Figure 4.2: Distributions of electron p_T and η for the W boson signal sample, compared to the prediction of the fast Monte Carlo (see Section 4.2).

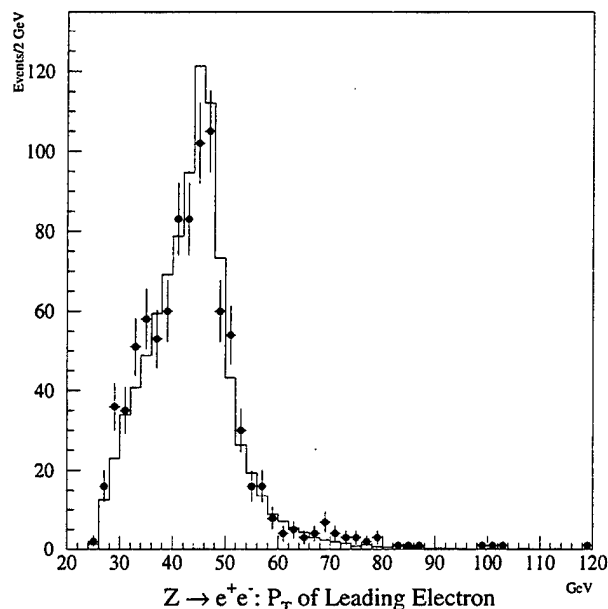


Figure 4.3: Distribution of the p_T of the leading electron for the Z boson signal sample, compared to the Monte Carlo prediction (see Section 4.2).

4.2 Acceptance

In order to translate the number of observed signal events into a cross section, it is essential to understand what fraction of W or Z boson events would be detected, given the detector geometry and the fiducial and kinematic cuts used to select the signal. Some fraction of the electrons produced in the W or Z boson events will enter the detector in regions that are either excluded from the analysis, or uninstrumented altogether. Furthermore, not all of the leptons produced by the W and Z decays have the transverse momentum necessary to satisfy the selection criteria. The acceptance is the fraction of all W or Z boson events that pass the fiducial and kinematic requirements.

To measure the acceptance, a large sample of simulated W or Z boson events was generated, and then detector effects were applied using a fast Monte Carlo program. The acceptance is given by the fraction of those events that satisfy the fiducial and

kinematic selection criteria.

4.2.1 Event Generation

The W and Z events were generated based on the lowest order weak Drell-Yan process, where the boson is generated through $q\bar{q}$ annihilation. The longitudinal momentum of the generated boson is determined by the momentum imbalance between the incoming quarks, whose momentum is determined according to the parton distribution functions used. At the lowest level, the generated boson has no transverse momentum; higher level QCD effects are necessary to add transverse momentum. As an alternative to incorporating the higher order processes into the boson generation itself, the generated W or Z bosons are given transverse momentum according to a second-order theoretical calculation of $d^2\sigma/dp_T d\eta$ by Arnold and Kauffman [63]. For high p_T , perturbative methods are used; for low p_T , a resummation scheme is used. A matching scheme is used to connect the two p_T regimes. Once the transverse and longitudinal momenta are known, the W or Z boson is decayed into leptons in its rest frame, then the leptons are boosted into the laboratory frame. A total of one million events of each type (W or Z boson) were generated for use in calculating the acceptance. At this point, the detector effects are added.

4.2.2 Detector Response

In order to get an accurate measurement of the acceptance, all relevant detector effects must be included, as well as other effects such as overlapping events and radiative decay. Also, any further effect of the signal selection cuts must be calculated; specifically, the acceptance of the invariant mass cut in the Z boson selection must be determined.

To properly model the fiducial acceptance, the z vertex distribution for the generated events was chosen to match that of the Run 1A data. A Gaussian distribution was used, with a width of 30 cm, centered at -8 cm.

Cryostat	C	Scale Factor
CC	0.0212 ± 0.006	1.072 ± 0.002
ECN	0.0316 ± 0.009	1.025 ± 0.005
ECS	0.043 ± 0.01	1.012 ± 0.007

Table 4.2: EM Resolution constant terms and scale correction factors

To properly measure the effect of the kinematic cuts on the electrons, the energy resolution of the calorimeters must be taken into account. The following parametrization was used to characterize the resolution of the EM calorimeters:

$$\left(\frac{\sigma}{E}\right)^2 = C^2 + \left(\frac{S}{\sqrt{E}}\right)^2 \quad (4.2)$$

where σ is the energy resolution in GeV (assumed Gaussian), E is the cluster energy in GeV, C (unit-less) is the constant term resulting from systematic errors such as channel-to-channel gain variation (after calibration), and S (in $\sqrt{\text{GeV}}$) is due to the statistical error in sampling. Using test-beam data, a value of $S = 0.157 \pm 0.005 \sqrt{\text{GeV}}$ was obtained for the North ECEM; this value was used for all three cryostats in the acceptance calculation, since the energy resolution for all three EM calorimeters is very similar, due to the similarity of construction. The values used for the constant term C are listed in Table 4.2. The electron energy also includes a scale-correction factor, determined by demanding that the mass based on $Z \rightarrow ee$ events match M_Z from LEP; any error in the correction factors leads to an error in the calculated acceptance. The correction factors are also listed in Table 4.2.

The resolution must be taken into account when calculating the acceptance of the \cancel{E}_T cut as well. Since the neutrino and electron momenta must add to the momentum of the parent W boson, the vector $\vec{\cancel{E}}_T$ is calculated in the generated events in the following way:

$$\vec{\cancel{E}}_T = \vec{p}_T(W) - \vec{p}_T(e) \quad (4.3)$$

The \cancel{E}_T resolution is determined by the resolutions for measuring the momentums of the electron and of the W boson. The detector resolution for $\vec{p}_T(e)$ is described above. The transverse momentum of the W is the result of initial state QCD radiation, usually resulting in soft recoiling jets; therefore, $\vec{p}_T(W)$ must be smeared using the hadronic energy resolution, as well as corrected for the hadronic energy scale. For the acceptance studies, a hadronic resolution of $50\%/\sqrt{E}$ was used [64]. To investigate the hadronic energy scale, the transverse momentum of the Z in $Z \rightarrow ee$ events was calculated both by using the soft hadronic recoiling energy and by using the two decay electrons; on average, the hadronic measurement of $p_T(Z)$ was smaller than the direct measurement using the electrons (although due to the poor hadronic energy resolution, there were cases where the hadronic $p_T(Z)$ was larger). In order to get the two measurements to agree, the direct measurement had to be corrected by the factor 0.83 ± 0.06 [65]; this factor was applied to the smeared soft hadronic energy in the generated W events, so that the momentum balance was modelled correctly. Finally, the effects of the underlying event are added in, based on a study of energy flow in minimum-bias events [64]. On average, about 4 GeV of hadronic transverse energy is added to the event, in a random direction in ϕ .

Next, the effect of the Level-2 E_T cut must be determined. Despite the fact that the cut threshold is 5 GeV lower than the offline threshold, the fast clustering algorithm used by the Level-2 filters does lead to a slight additional loss in acceptance. To study the turn-on effect of the 20 GeV threshold used by the ELE_HIGH filter, a sample of diagnostic events selected by the ELE_MEDIUM filter were used (these events were included in the ELF_WZ stream mentioned earlier); the E_T threshold for ELE_MEDIUM was 16 GeV. The steepness of the turn-on depended on the cryostat (CC versus EC), as well as whether the slow z vertex information from Level-0 was used in the Level-2 E_T calculation. The threshold response is shown in Figure 4.4. The turn-on data were fit with error functions; the fits were used in the detector simulation to determine whether an electron passed the Level-2 E_T cut. The overall loss of acceptance due to the Level-2 cut is very small, roughly 2%. The slow z

vertex was used for most (78%) of the signal data; for the remainder of the data, a nominal value of $z = 0$ was used to calculate the Level-2 E_T . The acceptance differed by about 0.5% for the two conditions; for the final acceptances, the results are combined, weighted by the integrated luminosities for the two conditions (see Table 4.3).

The kinematic acceptance of the electron E_T cut was corrected for radiation effects. If the electron radiates a photon, there is a potential lowering of the energy measured for the electron, depending on the separation of the electron and the radiated photon. The acceptance is calculated separately for $W\gamma$ and $Z\gamma$ events, analogously to the calculations for the pure W and Z events, except for the treatment of the electron energy. In the radiative events, the energies of the photon and associated electron are combined if the separation $\mathcal{R} = \sqrt{\Delta\eta^2 + \Delta\phi^2}$ is less than 0.3; otherwise, the E_T cut is applied to the electron energy alone (and the energy carried by the photon is lost). Approximately 35 % of $W \rightarrow e\nu$ events and 74 % of $Z \rightarrow ee$ events involve a radiative decay with $E_\gamma > 20$ MeV [66]; these fractions are used to combine the results of the radiative $W\gamma$ or $Z\gamma$ events with the pure W and Z events, leading to a 0.6 % correction to the W acceptance and a 1.6 % correction to the Z acceptance.

Finally, for the Z acceptance, the effect of the invariant mass cut must be calculated. The 75 to 105 GeV mass window contains 97.74% of the generated events. However, the events were generated within a separate window of 65 to 115 GeV in invariant mass, so some of the Breit-Wigner tails were cut off and a further correction was needed. Based on a calculation using a relativistic Breit-Wigner shape, the generated invariant mass range includes 97.7 % of all Z 's [64]; this leads to a value of 95.5 % for the acceptance of the invariance mass window cut.

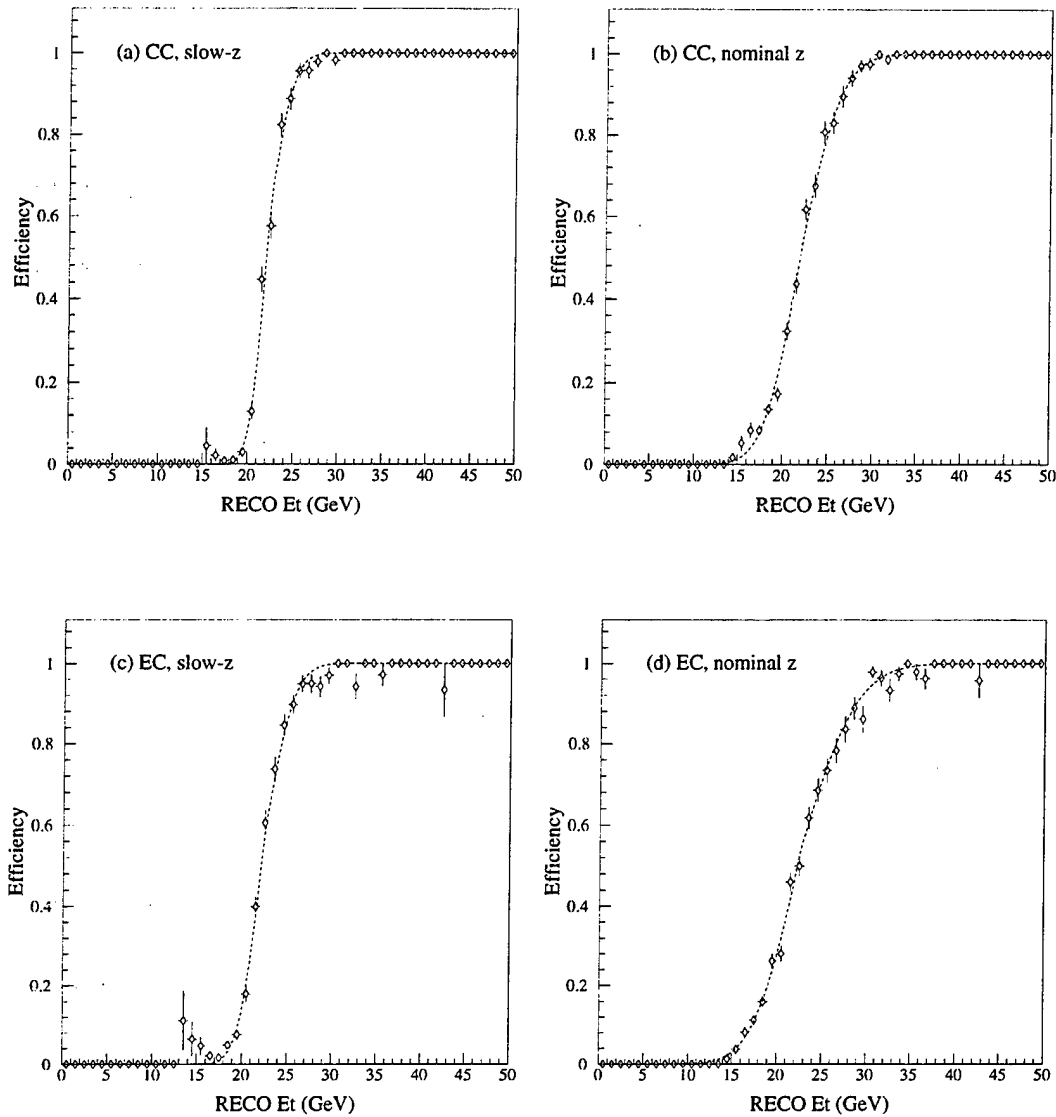


Figure 4.4: Level-2 E_T threshold response curves for the a) CC using the Level-0 slow z vertex, b) CC using a nominal vertex $z = 0$, c) EC using slow z and d) EC using $z = 0$. The fits shown are error functions.

Vertex used for Level-2 E_T	\mathcal{A}_W	\mathcal{A}_Z
Nominal ($z = 0$) (21.6%)	0.4559	-
Level-0 slow z (78.4%)	0.4612	-
Weighted Average	0.4601 ± 0.0060	0.3631 ± 0.0036

Table 4.3: Acceptances for W and Z boson events

4.2.3 Measured Acceptances and Errors

The nominal values of the acceptances were calculated with the following values of the W and Z masses and widths:

$$M_W = 80.21 \text{ GeV}, \Gamma_W = 2.12 \text{ GeV} \quad (4.4)$$

$$M_Z = 91.18 \text{ GeV}, \Gamma_Z = 2.487 \text{ GeV} \quad (4.5)$$

where M_W is an average of UA2, CDF and DØ results [34], Γ_W is the PDG world average [33], and the Z boson values come from the overall LEP average [33]. The corrected version of CTEQ2M [30] was used as the nominal structure function (in PDFLIB [67], this structure function is named CTEQ2pM to differentiate it from the original CTEQ2M which was retracted and replaced). The acceptances based on these values are summarized in Table 4.3; for \mathcal{A}_W , the acceptance depended on whether the Level-2 E_T was calculated using the nominal $z = 0$ or using the Level-0 slow z vertex measurement. The errors on the acceptances are discussed below. The distributions of the acceptances into the different cryostats is shown in Table 4.4.

Errors on the acceptances result from both the event generation (choice of structure function, p_T spectrum, choice of mass and width values) and the detector simulation (energy resolutions, z vertex distribution). The errors on the acceptance are summarized in Table 4.5; note that the percentages in the table are relative to the acceptance values.

$W \rightarrow e\nu$	
CC	$69.3 \pm 0.5\%$
EC	$30.7 \pm 0.5\%$
$Z \rightarrow ee$	
CC-CC	$49.5 \pm 0.5\%$
CC-EC	$40.5 \pm 0.3\%$
EC-EC	$10.0 \pm 0.4\%$

Table 4.4: Distributions for electrons in $W \rightarrow e\nu$ and $Z \rightarrow ee$ events into the different cryostats

Error Source	$\delta\mathcal{A}_W/\mathcal{A}_W(\%)$	$\delta\mathcal{A}_Z/\mathcal{A}_Z(\%)$
p_T spectrum	0.3	0.2
Structure function	0.4	0.6
Radiative corrections	0.3	0.4
δM_W	0.7	-
$\delta\Gamma_W$	< 0.2	-
Turn-on curves	0.3	< 0.1
Vertex distribution	0.4	0.4
EM energy resolution	0.1	0.3
EM energy scale	0.3	0.3
\cancel{E}_T resolution	0.6	-
Invariant mass cut	-	0.3
Total	1.3%	1.0%

Table 4.5: Systematic errors on the W and Z acceptances

The largest uncertainty in the W or Z p_T spectrum is in the soft, non-perturbative region, where resummation techniques are used to generate the spectrum of the soft gluon radiation. The differential cross section for the W or Z can be expressed as follows [63]:

$$\frac{d\sigma}{dp_T^2 dy} = \frac{4\pi^3 \alpha_W}{3s} e^2 \int \frac{d^2 b}{(2\pi)^2} e^{i\mathbf{b} \cdot \mathbf{p}_T} W(b_*) e^{-S_{np}(b)} \quad (4.6)$$

where b is an impact parameter (conjugate to p_T), $W(b_*)$ is a complicated function of p_T and α_s , and b_* incorporates a cutoff b_{max} to handle a divergence at high- b :

$$b_* = \frac{b}{\sqrt{1 + b^2/b_{max}^2}} \quad (4.7)$$

The function $S_{np}(b)$ incorporates the non-perturbative effects at high- b ; Davies et al. [68] use the following parametrization:

$$S_{np}(b) = b^2 [g_1 + g_2 \ln(b_{max} Q/2)] \quad (4.8)$$

where Q is the mass of the relevant gauge boson. The parameters g_1 and g_2 are determined by fitting available Drell-Yan data; b_{max} is set to 2 GeV^{-1} , the lowest scale where structure functions were available. For $Q = M_W$, The value favored by the fit is

$$S_{np} = (1.36 \text{ GeV}^2) b^2; \quad b_{max} = (2 \text{ GeV})^{-1} \quad (4.9)$$

and the following range of values is allowed:

$$(0.8 \text{ GeV}^2) b^2 < S_{np} < (1.8 \text{ GeV}^2) b^2 \quad (4.10)$$

The favored value for S_{np} corresponds to values $g_1 = 0.15 \text{ GeV}^2$ and $g_2 = 0.4 \text{ GeV}^2$. In order to estimate the error on the acceptance due to the p_T spectrum, the values $g_1 = 0.09 \text{ GeV}^2$ and $g_2 = 0.25 \text{ GeV}^2$ were used, which corresponds to $S_{np} = 0.84b^2$, very close to the lower extreme value. Using these values leads to a 0.3% change in the $W \rightarrow e\nu$ acceptance and a 0.2% change in the $Z \rightarrow ee$ acceptance, as indicated in Table 4.5.

In order to estimate the error due to the structure functions, the acceptance was calculated using a total of six different sets of structure functions: CTEQ2M [30] (updated version; used for central value of acceptance), CTEQ2M (old version), CTEQ2MS, MRSD0' [69], MRSD- and GRV [70]. The largest difference was used to estimate the error of 0.4% for the W acceptance and 0.6% for the Z acceptance.

The error due to including radiative corrections is estimated by varying the cone size used to decide whether the radiated energy is included in the electron cluster.

The world-average M_W quoted above has an error of 180 MeV; varying M_W by this amount leads to a 0.7% change in the W acceptance. Similarly, varying Γ_W by 500 MeV leads to a very small effect on \mathcal{A}_W , less than 0.2%. No errors are quoted for the Z acceptance due to δM_Z or $\delta \Gamma_Z$, since these quantities are known extremely accurately.

The sharpness of the Level-2 E_T turn-on curves depends on how well the z -vertex is known, as is evident from the difference between the curves based on using the Level-0 slow z and the ones based on using the nominal $z = 0$. The accuracy of the Level-0 slow z is significantly degraded if there is more than one interaction. No cuts were made on the number of vertices to make the curves used to calculate the acceptance central values; in order to estimate the error on the acceptance, the acceptance was calculated using curves based only on single-vertex events as well as curves based only on multi-vertex events; the result is a 0.3% variation in the W acceptance and a negligible effect on the Z acceptance.

The Gaussian width used to generate the z vertex distribution was varied from 25 to 35 cm to estimate the effect of any difference between the data vertex distribution and that used to generate the events. This resulted in a 0.4% change in both the W and Z acceptances.

The electron energy resolution terms and scale factors were varied within their measured errors. The effect on the acceptances was small.

The error on the W acceptance due to \cancel{E}_T resolution results from both variation in the hadronic energy resolution and variation in the correction factor used. The

effect of the variation of the correction factor dominates; a 1-sigma variation in that factor leads to a 0.6% shift in the W acceptance.

Finally, the error on the Z acceptance due to the cut on invariant mass is estimated by varying the line shape by using different structure functions, as well as comparing the effect of using the smeared or unsmeared masses. The overall contribution to the Z acceptance error is 0.3%, which is dominated by the shape variation (the difference between using smeared and unsmeared masses is only about 0.1%).

4.3 Efficiency

In order to measure the $W \rightarrow e\nu$ and $Z \rightarrow ee$ cross sections, it is essential to have a good understanding of the efficiency of the event selection. For this analysis, the selection efficiency incorporates two factors: the efficiency of the Level- \emptyset system for detecting W or Z boson events, and the efficiency for detecting the high p_T electrons produced in the decays of the bosons (this includes both trigger efficiencies and offline identification efficiencies). First, consider the Level- \emptyset efficiency.

4.3.1 Level- \emptyset Efficiency

During Run 1A, all events (except for the highly prescaled zero-bias events) had to satisfy the hardware Level- \emptyset trigger. The requirements are simple: both Level- \emptyset counter arrays must be hit, and the fast- z calculated from the hit times must be consistent with an interaction with $|z_{vtx}| < 96.875$ cm during the most recent crossing (in order to eliminate events from satellite crossings).

There are, in principle, two ways to measure the efficiency of the Level- \emptyset system for detecting W and Z boson effects: either use a data sample taken without the Level- \emptyset requirement (but with the Level- \emptyset information saved along with the event), or use a Monte Carlo sample of events along with a detailed detector simulation. Both methods can be troublesome. In order to use real data to measure the efficiency, there

must be a large sample of W and Z events taken without the Level-0 requirement. On the other hand, in order to use the Monte Carlo sample and believe the results, the underlying event must be extremely well understood and simulated. Furthermore, care must be taken to properly handle multiple vertex events. For these reasons, it is preferable to base the efficiency data on real data; however, in Run 1A, almost no data were written to tape that did not pass the Level-0 trigger. Fortunately, this deficiency has been addressed in Run 1B, where a considerable amount of data was taken without the Level-0 requirement.

Using the signal selection cuts described previously, a sample of W events was chosen from data from the EM1.EISTRKCC_MS Level-2 filter, which (for trigger versions 10.0 and later) does not require Level-0 to fire. This filter applies cuts similar to the ELE_HIGH filter, and also applies several other cuts in order to cut down the trigger bandwidth used: a new hardware Level-1.5 trigger, a tracking cut in the CC region in Level-2, and a cut on \cancel{E}_T in Level-2 as well. The additional cuts do not significantly change the quality of the data after the offline cuts have been applied, and so should have no effect on the results. Due to lack of statistics, the Level-0 efficiency based on this W sample is used for both the W and Z cross section calculations; this is not a significant problem since the underlying events for the two event types are essentially identical.

Many of the signal events contain more than one interaction; the additional interaction increases the probability that the Level-0 requirements will be satisfied. This must be properly taken into account; the overall Level-0 efficiency can be expressed as follows [71]:

$$\varepsilon_{L0}(W) = \sum_{n=0}^{\infty} \varepsilon_{L0}(W+n) \cdot P(n) \quad (4.11)$$

where $\varepsilon_{L0}(W)$ is the overall Level-0 efficiency for the W events, $\varepsilon_{L0}(W+n)$ is the Level-0 efficiency for a W event combined with n minimum bias events, and $P(n)$ is the probability of having n minimum bias events accompanying the W event. With each additional event, the probability of Level-0 firing increases, quickly approaching

unity. Taking $\varepsilon_{L\emptyset}(W + n) = 1$. for $n \geq 2$ and applying $\sum_n P(n) = 1$. leads to

$$\varepsilon_{L\emptyset}(W) = \varepsilon_{L\emptyset}(W + 0) \cdot P(0) + \varepsilon_{L\emptyset}(W + 1) \cdot P(1) + (1. - P(0) - P(1)) \quad (4.12)$$

For simplicity, the number of vertices found by the central tracking system was used as a measure of the number of interactions. Based on the W signal sample,

$$P(0) = 0.772 \pm 0.004; \quad P(1) = 0.214 \pm 0.004 \quad (4.13)$$

The Run 1B data without the Level- \emptyset requirements is used to determine $\varepsilon_{L\emptyset}(W + n)$ [72]. Of 6399 events with a single vertex, 207 events do not pass Level- \emptyset . A study of the W events [73] that fail Level- \emptyset reveals that $28 \pm 10\%$ are halo events, and should be removed from both the numerator and denominator of the efficiency ratio. This leads to

$$\varepsilon_{L\emptyset}(W + 0) = 1. - \frac{149. \pm 21.}{6341. \pm 21.} = 0.977 \pm 0.004 \quad (4.14)$$

where the quoted error combines the binomial statistical error with the halo classification error and a small error assigned for any possible variation due to event selection differences. Similarly, for events with two tracking vertices, there are 23 events out of 3261 that fail Level- \emptyset . This gives

$$\varepsilon_{L\emptyset}(W + 1) = 1. - \frac{16.6 \pm 2.3}{3254.6 \pm 2.3} = 0.995 \pm 0.002 \quad (4.15)$$

Plugging all the numbers into the expression for the overall W Level- \emptyset efficiency gives

$$\varepsilon_{L\emptyset}(W) = 0.981 \pm 0.003 \quad (4.16)$$

Any change in the Level- \emptyset system between Run 1A and Run 1B would result in an error in the measured efficiency. There was some work done to the Level- \emptyset counters and electronics between runs; the overall efficiency was unchanged, however [73]. This was determined by looking at the relative rates compared to CDF before and after the changes; a conservative error of 1% was assigned to this assertion. This error applies directly to the measured Level- \emptyset efficiency, and becomes the dominant error. The final W and Z Level- \emptyset efficiencies are therefore

$$\varepsilon_{L\emptyset} \equiv \varepsilon_{L\emptyset}(W) = \varepsilon_{L\emptyset}(Z) = 0.98 \pm 0.01 \quad (4.17)$$

4.3.2 Electron Selection Efficiency

The efficiency for detecting the high p_T electrons produced in the W and Z boson decays contains several factors: trigger, reconstruction of electromagnetic energy clusters as electrons or photons, track-match, and electron-identification. To measure the efficiency of all the components of the selection, it is essential to have a clean sample of unbiased electrons. The sample used for this study makes use of the “second” electrons from $Z \rightarrow ee$ events.

4.3.2.1 Diagnostic Data Sample

The sample of diagnostic Z events, like the signal sample, is taken from the ELF_WZ sample. The selection procedure is as follows. First, the diagnostic events must pass the single electron filter ELE_HIGH (these events will be used to study the trigger efficiency, so no trigger requirement is applied to the second electron at this point). Next, the diagnostic events must have two PELC banks with $E_T > 25$ GeV in the standard fiducial region. Furthermore, a set of tight tagging cuts is applied to one of the electrons; part of these tagging cuts is the requirement that the tagged electron passed the ELE_HIGH filter, guaranteeing that the second electron is unbiased by any trigger requirement. Finally, cuts are applied to the second electron in order to obtain a properly biased sample; for example, if the efficiency of the offline electron-identification cuts for triggered electrons is being studied, the second electron is required to pass ELE_HIGH. Note that if both electrons in a $Z \rightarrow ee$ event pass the tagging cuts, the event is used twice in the efficiency studies. The standard electromagnetic scale correction is applied before making any E_T cuts. As in the signal selection, only events with run numbers 55217 or greater are used; this ensures that all variations of the trigger and filter with run number are properly taken into account (only the bulk efficiencies are measured; low statistics prevents separate measurements of the efficiencies for all conditions).

4.3.2.2 Signal and Background

Since most of the real $Z \rightarrow ee$ events have an invariant mass very close to M_Z and the background is relatively flat, the purest sample of real electrons is obtained by using events in the invariant mass region around the Z peak. In this analysis, the signal region is defined by events having an invariant mass in the range $86 < M_{ee} < 96$ GeV.

The background in the $Z \rightarrow ee$ sample (either the diagnostic sample or the signal sample) comes mainly from two sources: QCD di-jet events (where the jets fake electrons) and Drell-Yan events (which produce two electrons, like the Z signal events). The combined background spectrum falls roughly linearly with invariant mass. This fact can be used to estimate the amount of background in the signal region; three different methods have been used. Each method uses one or more sideband regions in order to estimate the efficiency for selecting background events. The three methods are detailed below:

- Method 1: Two sideband regions are used, $61 < M_{ee} < 71$ GeV and $111 < M_{ee} < 121$ GeV. Since these regions are symmetric around the signal region and cover the same range in invariant mass, the number of background events in the signal region is just taken to be the average of the number of events in the two sideband regions (this assumes that all the events in the sideband regions are background).
- Method 2: The invariant mass spectrum of the diagnostic Z sample is fit to a relativistic Breit-Wigner convoluted with a Gaussian and added to a linear background. The linear background fit is used to estimate the number of background events in the signal region as a fraction of the number of events in the sideband region $60 < M_{ee} < 70$ GeV.
- Method 3: The same fit is used directly to estimate the number of background events in the signal region (the number of background events is just the area

under the linear background between 86 and 96 GeV). Dual sideband regions are used: $M_{ee} < 70$ GeV and $M_{ee} > 110$ GeV.

The background fraction (f_b) is defined as the ratio of the number of background events in the signal region to the total number of events in the signal region.

The goal of the efficiency measurement is to determine the efficiency of a given cut (or set of cuts) on a true electron. To do this, it is necessary to remove the effect of the background in the signal sample, that is, calculate a background-subtracted efficiency. The background subtracted efficiency is given by

$$\varepsilon = \frac{\varepsilon_s - \varepsilon_b f_b}{1 - f_b} \quad (4.18)$$

where ε is the background subtracted efficiency, ε_s is the efficiency measured in the signal region, ε_b is the efficiency measured in the background (sideband) region, and f_b is the background fraction described above. Note that it is possible to obtain a background subtracted efficiency greater than 1 (in which case measurement error should make the result consistent with 100% efficiency).

4.3.2.3 Tagging Cuts

In order to control the amount of background in the diagnostic data sample, while keeping the sample of diagnostic electrons unbiased, a set of tight cuts is applied to one of the two electrons in the sample. In this analysis, two different sets of tagging cuts are used (labelled Standard and Tight). Combined with the three different background estimation methods, six different prescriptions were used to determine the background-subtracted efficiencies detailed below. These six methods are detailed in Table 4.6. The differences in the results produced by the different methods is used as a measure of the systematic uncertainty due to the background subtraction process.

The two sets of tagging cuts are detailed below; in both cases the tagged electron is a PELC with $E_T > 25$ GeV in the good fiducial region of the detector.

Background Subtraction Prescriptions		
Prescription	Background Method	Tagging Cuts
1	1	Standard
2	1	Tight
3	2	Standard
4	2	Tight
5	3	Standard
6	3	Tight

Table 4.6: Definition of Background Subtraction Prescriptions

- Standard Tagging Cuts:
 - Tagged PELC passed ELE_HIGH
 - $\chi_{hm}^2 < 100.(200.)$ in the CC(EC)
 - $f_{iso} < 0.15$
 - $f_{em} > 0.9$ (standard PELC requirement)
 - $S_{trk} < 10.$
- Tight Tagging Cuts:
 - Tagged PELC passed ELE_HIGH
 - $\chi_{hm}^2 < 100.$ (both CC and EC)
 - $f_{iso} < 0.10$
 - $f_{em} > 0.95$
 - $S_{trk} < 5.(10.)$ in the CC(EC)

Note once again that if both PELCs in a diagnostic Z event pass the tagging cuts, the event is used twice in the efficiency analysis.

4.3.2.4 Loose and Tight Selection Efficiencies

Two different electron selections are used for this analysis. “Tight” selection cuts are used for the selection of both W and Z bosons; a second “loose” set of cuts is used to identify the second electron in $Z \rightarrow ee$ events. Since the loose cuts are a subset of the tight cuts, the tight electron selection efficiency can be expressed as follows:

$$\varepsilon_{ele}^w = \varepsilon_\ell \cdot \varepsilon_t \quad (4.19)$$

where ε_{ele}^w is the overall tight electron selection efficiency (equivalent to the W electron selection efficiency), ε_ℓ is the efficiency of the loose cuts, and ε_t is the efficiency of the additional cuts used to make up the tight selection. The loose selection cuts include identifying an electromagnetic energy cluster as an electron or photon and applying calorimeter-based electron-identification cuts; the tight selection further requires a track-match, applies a cut on the quality of that match, and requires that the electron passed the chosen trigger. Thus,

$$\varepsilon_{ele}^w = \underbrace{\varepsilon_{reco} \cdot \varepsilon_{cal}}_{\varepsilon_\ell} \cdot \underbrace{\varepsilon_{trig} \cdot \varepsilon_{trk} \cdot \varepsilon_{match}}_{\varepsilon_t} \quad (4.20)$$

where, for a real electron, ε_{reco} is the efficiency for forming an electron or photon bank during reconstruction, ε_{cal} is the efficiency of the calorimeter electron-identification cuts, ε_{trig} is the trigger efficiency, ε_{match} is the efficiency for finding a track-match in the central detector, and ε_{trk} is the efficiency of the track match quality cut (track-match significance).

For true high- p_T electrons in the good fiducial region of the detector used for this analysis, the reconstruction efficiency should be 100%. Unfortunately, a bug in the CAPHEL package (the part of the reconstruction that searches CALorimeter data to find PHotons and ELections) resulted in a small inefficiency. For a small fraction of the electromagnetic clusters, the routine that determines the position (CM3POS) calculated the ϕ position incorrectly (it was rotated by π). This bug was measured to cause a 0.7% loss of efficiency [74] (with negligible error), so $\varepsilon_{reco} = 0.993$.

The efficiency of the calorimeter electron-identification cuts ε_{cal} is measured using the diagnostic $Z \rightarrow ee$ sample described above. The only requirement placed on the diagnostic electron is that it is a PELC bank with $E_T > 25$ GeV. Note that by requiring a PELC, a track-match is required; for the calorimeter cuts that make up the loose selection, this requirement does not bias the results, and the amount of background in the diagnostic sample is greatly reduced, allowing a more precise measurement.

For this efficiency measurement, there are four data samples: CC or EC diagnostic electron, combined with Standard or Tight tagging cuts. For each sample, three background estimation schemes are used, for a total of twelve background-subtracted efficiency measurements (six each for the CC and EC). The basic scheme for measuring the background subtracted efficiency is as follows:

- Measure the efficiency ε_s in the signal region: what fraction of diagnostic electrons with $86 < M_{ee} < 96$ GeV pass the calorimeter electron-id cuts?
- Measure the efficiency ε_b in the background region: what fraction of events in the sideband region(s) pass the same cuts?
- Measure the background fraction f_b : divide the number of background events in the signal region (as predicted by the background method in use) by the total number of events in the signal region.
- Combine these three quantities to get the background subtracted efficiency using Equation 4.18.

The results for the calorimeter electron-identification efficiency are listed in Table 4.7; the quoted errors are statistical only. To obtain the overall loose selection efficiency, multiply by the reconstruction efficiency $\varepsilon_{reco} = 0.993$.

The efficiency of the additional cuts used by the tight selection are calculated in a similar manner. There are three additional requirements: trigger, track match,

Calorimeter Id efficiency ε_{cal}		
Prescription	CC	EC
1	0.884 ± 0.016	0.898 ± 0.026
2	0.887 ± 0.015	0.880 ± 0.024
3	0.880 ± 0.016	0.918 ± 0.027
4	0.885 ± 0.015	0.889 ± 0.024
5	0.886 ± 0.016	0.902 ± 0.026
6	0.887 ± 0.015	0.890 ± 0.024

Table 4.7: Calorimeter electron-identification efficiency: ε_{cal} . To calculate the loose selection efficiency ε_ℓ , multiply both the value and its error by the reconstruction efficiency $\varepsilon_{reco} = 0.993$.

and track-match significance. The trigger and track-match significance efficiencies are measured and lumped together, in order to reduce the total error:

$$\varepsilon_{lump} = \varepsilon_{trig} \cdot \varepsilon_{trk}; \quad \varepsilon_t = \varepsilon_{lump} \cdot \varepsilon_{match} \quad (4.21)$$

To measure the lumped efficiency, the diagnostic electrons are required to be PELC banks with $E_T > 25$ GeV; in addition, they must pass all the loose selection cuts (so that the sample is properly biased). In addition, any diagnostic electron that failed the 20 GeV Level-2 E_T cut is eliminated from the sample, since the turn-on effect is already accounted for in the acceptance. The lumped efficiency is calculated analogously to the loose efficiency (except now the fraction of diagnostic electrons that pass the trigger and track-match significance cuts is calculated); the results are listed in Table 4.8.

The tight electron selection also requires a PELC (electron) bank; PPHO (photon) banks are not accepted. A PELC bank requires a central detector track in a road centered around the calorimeter cluster position. The track-match efficiency ε_{trk} is a measure of how well the central detector finds the tracks associated with a real electron; here, it is taken to be the ratio of the number of diagnostic $Z \rightarrow ee$ electrons that appear as PELC banks to the number found as either PELC or PPHO banks

Lumped efficiency ε_{lump}		
Prescription	CC	EC
1	0.951 ± 0.009	0.926 ± 0.019
2	0.951 ± 0.009	0.930 ± 0.018
3	0.953 ± 0.009	0.921 ± 0.018
4	0.952 ± 0.009	0.924 ± 0.018
5	0.950 ± 0.009	0.921 ± 0.018
6	0.948 ± 0.009	0.927 ± 0.018

Table 4.8: Lumped trigger and track-match significance efficiency: $\varepsilon_{lump} = \varepsilon_{trig} \cdot \varepsilon_{trk}$

(since the only difference is the track-match requirement).

The cuts used to define the diagnostic sample used to measure the track-match efficiency are slightly different than those used above. To increase statistics, the E_T cut on both the tag and diagnostic electrons is lowered from 25 to 20 GeV. The same fiducial cuts are used. The tagging cuts are the same, except the cut on track-match significance is not applied. The following cuts are applied to the diagnostic electrons:

- PELC or PPHO, $E_T > 20$ GeV, good fiducial region
- passed ELE_HIGH
- $\chi_{hm}^2 < 100.$, $f_{iso} < 0.15$

These cuts are applied to keep the amount of background in the sample at a reasonable level (since accepting PPHO banks significantly increases the background). Different sets of cuts were tried with little effect on the results, so the results are taken to be unbiased by the application of these cuts.

The background-subtracted efficiencies are calculated exactly as described above, where now the efficiency ratio is the number of PELCs divided by the total number of electrons (PELCs plus PPHOs). The track-match efficiencies are listed in Table 4.9.

Track-match efficiency ε_{match}		
Prescription	CC	EC
1	0.873 ± 0.013	0.832 ± 0.021
2	0.875 ± 0.013	0.838 ± 0.021
3	0.879 ± 0.013	0.829 ± 0.021
4	0.882 ± 0.013	0.835 ± 0.021
5	0.874 ± 0.012	0.838 ± 0.020
6	0.876 ± 0.012	0.843 ± 0.020

Table 4.9: Track-match efficiency: ε_{match}

Tight efficiency ε_t		
Prescription	CC	EC
1	0.830 ± 0.015	0.770 ± 0.025
2	0.832 ± 0.015	0.779 ± 0.025
3	0.837 ± 0.015	0.764 ± 0.024
4	0.839 ± 0.015	0.772 ± 0.025
5	0.830 ± 0.014	0.772 ± 0.024
6	0.830 ± 0.014	0.781 ± 0.024

Table 4.10: Efficiency of tight electron selection cuts: $\varepsilon_t = \varepsilon_{lump} \cdot \varepsilon_{match}$.

The efficiency of the tight selection cuts is the product of the lumped trigger/track-match significance efficiency (ε_{lump}) and the track-match efficiency (ε_{match}). The results are listed in Table 4.10.

4.3.3 Overall W and Z Selection Efficiencies

As specified above, the selection efficiency for the electron in $W \rightarrow e\nu$ events is given by the product of the loose and tight selection efficiencies (see Equation 4.19). The efficiency is calculated separately for each prescription, and the results are shown

W electron efficiency ε_{ele}^w		
Prescription	CC	EC
1	0.729 ± 0.019	0.687 ± 0.030
2	0.733 ± 0.018	0.681 ± 0.029
3	0.731 ± 0.019	0.696 ± 0.030
4	0.737 ± 0.018	0.682 ± 0.029
5	0.730 ± 0.018	0.691 ± 0.029
6	0.731 ± 0.017	0.690 ± 0.028

Table 4.11: Overall W electron selection efficiency: ε_{ele}^w

in Table 4.11. Prescription 6 (tight tagging cuts, background estimation based on fit) is used for the central value; the systematic error due to background subtraction is taken to be half the maximum difference between different background subtraction prescriptions. Thus, the W electron selection efficiencies for the CC and EC are

$$\varepsilon_{ele}^w(cc) = 0.731 \pm 0.017 \pm 0.004; \quad \varepsilon_{ele}^w(ec) = 0.690 \pm 0.028 \pm 0.008 \quad (4.22)$$

To get the overall W electron selection efficiency, the CC and EC results are combined based on the CC/EC acceptance distribution, listed in Table 4.4:

$$\varepsilon_{ele}^w = 0.719 \pm 0.015 \quad (4.23)$$

where the quoted error combines the statistical and systematic errors above.

The final W selection efficiency is obtained by multiplying the electron selection efficiency by the Level-0 efficiency:

$$\varepsilon_{tot}^w = \varepsilon_{L0} \cdot \varepsilon_{ele}^w = 0.704 \pm 0.017 \quad (4.24)$$

For the Z boson electron selection efficiency, since there are two electrons and the efficiencies are measured separately for the CC and the EC, there are three distinct cases: both electrons in the CC, both electrons in the EC, and one electron in each. The following expressions apply for the three cases:

<i>Z</i> electron efficiency ε_{ele}^z			
Prescription	CC-CC	CC-EC	EC-EC
1	0.748 ± 0.021	0.752 ± 0.020	0.753 ± 0.034
2	0.754 ± 0.020	0.741 ± 0.018	0.726 ± 0.030
3	0.743 ± 0.021	0.766 ± 0.021	0.785 ± 0.037
4	0.752 ± 0.020	0.747 ± 0.018	0.739 ± 0.031
5	0.752 ± 0.021	0.757 ± 0.020	0.761 ± 0.034
6	0.753 ± 0.020	0.749 ± 0.018	0.744 ± 0.031

Table 4.12: Overall *Z* electron selection efficiency: ε_{ele}^z

$$\varepsilon_{ele}^z(cc - cc) = (\varepsilon_\ell^c)^2 \cdot [2\varepsilon_t^c - (\varepsilon_t^c)^2] \quad (4.25)$$

$$\varepsilon_{ele}^z(cc - ec) = \varepsilon_\ell^c \cdot \varepsilon_\ell^e \cdot (\varepsilon_t^c + \varepsilon_t^e - \varepsilon_t^c \cdot \varepsilon_t^e)$$

$$\varepsilon_{ele}^z(ec - ec) = (\varepsilon_\ell^e)^2 \cdot [2\varepsilon_t^e - (\varepsilon_t^e)^2]$$

where ε_ℓ^c and ε_ℓ^e are the loose selection efficiencies for the CC and the EC, and ε_t^c and ε_t^e are the efficiencies of the additional tight selection cuts in the two cryostats. The equations are easy to understand: both electrons must pass the loose selection cuts (hence the two factors of ε_ℓ), but only one of the electrons has to pass the additional tight selection cuts; the subtracted term removes the double-counting of events in which both electrons pass the tight cuts. The *Z* electron selection efficiencies are calculated separately for each background subtraction prescription; the results are shown in Table 4.12.

Using prescription 6 for the central values and extracting the systematic error as described above, the *Z* electron selection efficiencies are

$$\varepsilon_{ele}^z(c - c) = 0.753 \pm 0.020 \pm 0.006 \quad (4.26)$$

$$\varepsilon_{ele}^z(c - e) = 0.749 \pm 0.018 \pm 0.013$$

$$\varepsilon_{ele}^z(e - e) = 0.744 \pm 0.031 \pm 0.030$$

The total Z electron selection efficiency is obtained by combining these results based on the acceptance distributions listed in Table 4.4, with care taken to properly handle correlations in the error calculation:

$$\epsilon_{ele}^z = 0.751 \pm 0.018 \quad (4.27)$$

Finally, the overall Z selection efficiency is obtained by multiplying by the Level-0 efficiency:

$$\epsilon_{tot}^z = \epsilon_{L0} \cdot \epsilon_{ele}^z = 0.736 \pm 0.024 \quad (4.28)$$

4.4 Background

A precise measurement of the W and Z boson cross sections relies upon an accurate knowledge of the background content in the signal data sample. The electron decay modes of the heavy bosons provide a very clear signature, so that even the simple set of cuts outlined above provides a very clean data sample. However, any set of cuts must make a compromise between signal efficiency and background contamination; the cuts are chosen to reduce the background as much as possible while minimizing the loss of signal events. A small amount of background is acceptable in the signal sample, as long as it can be reliably measured.

4.4.1 Background in the $W \rightarrow e\nu$ Sample

The combination of a high p_T electron and large \cancel{E}_T form a very unique signature; nevertheless, there are several sources of background to the $W \rightarrow e\nu$ selection. One main source comes from di-jet events, where one jet fakes an electron, and fluctuations in the energy measurement provide the requisite missing transverse energy. Further background comes from $W \rightarrow \tau\nu$ events with the subsequent decay $\tau \rightarrow e\nu$; these events have identical signatures to the direct $W \rightarrow e\nu$ events; fortunately, the electron p_T and \cancel{E}_T spectra are much softer. A final source of background comes from $Z \rightarrow$

ee and $Z \rightarrow \tau\tau$ events, where the electron is real and the \cancel{E}_T comes from energy mismeasurement.

4.4.1.1 QCD multi-jet background

The largest source of $W \rightarrow e\nu$ background comes from QCD multi-jet events, where one of the jets fakes an electron and the missing transverse energy comes from energy mismeasurement (either an energy fluctuation, or a lot of energy is lost in a detector crack). The quantity of QCD background in the signal sample is measured using collider data [75]; the procedure is outlined below.

The general technique is based on using the \cancel{E}_T spectrum shape to estimate the fraction of signal events due to QCD processes. Two data samples are used: one to determine the \cancel{E}_T shape of the combined signal and background, and one to determine the \cancel{E}_T shape of the background alone.

The signal sample uses the same cuts used to select the $W \rightarrow e\nu$ sample, with the \cancel{E}_T cut removed:

- Event passed ELE_HIGH filter
- One PELC in good fiducial region with $E_T > 25$ GeV
- Calorimeter electron-identification: $\chi_{hm}^2 < 100.$, $f_{iso} < 0.10$, $f_{em} > 0.95$
- Tracking electron-identification: $S_{trk} < 10.(5.)$ in the CC(EC)

All energy corrections used for the $W \rightarrow e\nu$ selection are applied to this sample as well. A total of 12,938 events were selected in the run range 55217-59378, corresponding to trigger versions 6.1-6.5, when the trigger used to select the background sample (described below) was in place. The \cancel{E}_T distribution for these events is shown in Figure 4.5. The large peak at low missing E_T is due to QCD di-jet events; the broader peak at high \cancel{E}_T comes from the $W \rightarrow e\nu$ signal.

In order to measure the QCD contamination in the signal sample, an independent sample of events is needed to measure the shape of the di-jet events. The electron

isolation variable is used to obtain a sample of background electrons; by making an anti-isolation cut (that is, by requiring the electron to be non-isolated), true electrons are excluded from the sample. The background event selection is based on the ELE_MEDIUM filter, which does not apply an isolation cut; this filter was present only in trigger versions 6.1 through 6.5, corresponding to runs 55217 through 59378. The following cuts were used to select the background sample, after the standard energy corrections were applied:

- Event passed ELE_MEDIUM filter
- One PELC in good fiducial region with $E_T > 25$ GeV
- $f_{em} > 0.95$, $f_{iso} > 0.15$

These events contain one jet which fluctuated to give an electromagnetic shower and produce a PELC bank; the isolation fraction is high due to a large amount of hadronic energy surrounding the cluster. There are 5655 events in this sample. The \cancel{E}_T spectrum of this sample, shown in Figure 4.5, reflects the shape of the di-jet background, since isolation and \cancel{E}_T are not correlated. All real $W \rightarrow e\nu$ signal events should be removed by the anti-isolation cut (note that there is no evidence for a peak in the \cancel{E}_T signal region for the background sample); to check this, the analysis was repeated with an anti-isolation cut of $f_{iso} > 0.25$, and the results obtained were consistent with the looser anti-isolation requirement.

The di-jet background is calculated separately for electrons in the CC and the EC, to allow for variation of the QCD background with rapidity (due to either the underlying physics or to variation in detector response). Furthermore, two different isolation cone sizes were used by the ELE_HIGH filter during different periods in the data-taking, $\mathcal{R}_{iso} = 0.4$ and $\mathcal{R}_{iso} = 0.6$; this difference impacts the amount of QCD background, since the Level-2 isolation cut differs somewhat from the offline cut due to different clustering, and in the case of $\mathcal{R}_{iso} = 0.6$, the Level-2 cut was tighter. As a result, the di-jet fraction must be calculated separately for the two trigger conditions.

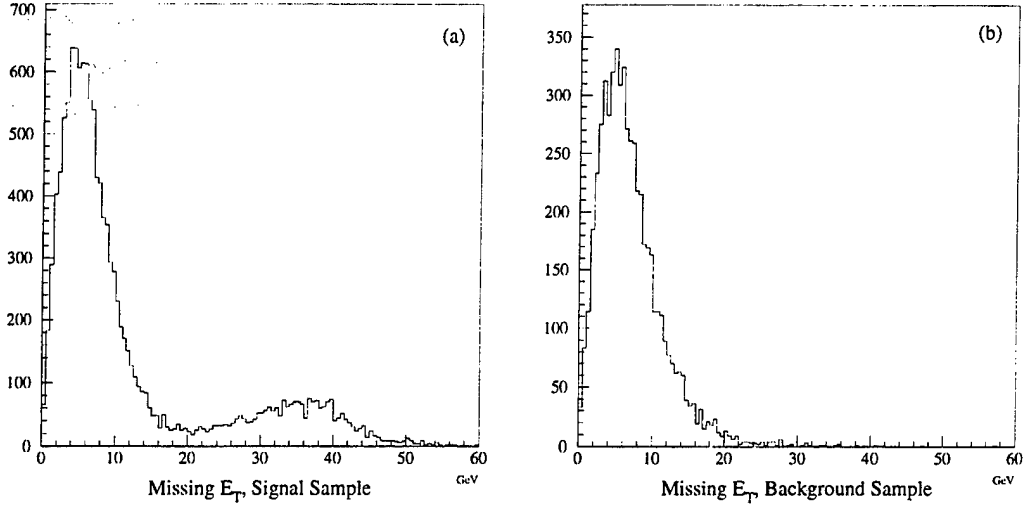


Figure 4.5: \cancel{E}_T spectra for the (a) signal and (b) background event samples

All in all, the signal sample is split into four sub-samples: CC(0.4), CC(0.6), EC(0.4) and EC(0.6); the background sample is just split between CC and EC ‘electrons.’

The actual calculation of the QCD background is straightforward. For each of the four conditions, the appropriate background sample is normalized to the signal sample, using the region 0 - 10 GeV in \cancel{E}_T . The background fraction f_{qcd} is then given by the number of events in the background sample with $\cancel{E}_T > 25$ GeV scaled by the normalization factor f_{norm} divided by the number of events in the signal sample with $\cancel{E}_T > 25$ GeV:

$$f_{qcd} = \frac{N_{bkg}(\cancel{E}_T > 25) \cdot f_{norm}}{N_{sig}(\cancel{E}_T > 25)}; \quad f_{norm} = \frac{N_{sig}(\cancel{E}_T < 10)}{N_{bkg}(\cancel{E}_T < 10)} \quad (4.29)$$

where $N_{sig}(\cancel{E}_T)$ and $N_{bkg}(\cancel{E}_T)$ are the numbers of events in the specified \cancel{E}_T range in the signal and background samples respectively.

The results are summarized in Table 4.13. For the final QCD di-jet fractions, the first error is statistical and the second is the systematic error due to the normalization scheme. The statistical error is totally dominated by the small number of background events in high \cancel{E}_T region. To measure the normalization error, the normalization

	$\mathcal{R}_{iso} = 0.4$		$\mathcal{R}_{iso} = 0.6$	
	CC	EC	CC	EC
$f_{norm} = \frac{N_{sig(<10)}}{N_{bkg(<10)}}$	$\frac{498}{2611} = 0.191$	$\frac{891}{1928} = 0.462$	$\frac{3362}{2611} = 1.288$	$\frac{5440}{1928} = 2.822$
$N_{bkg}(> 25)$	35	9	35	9
$f_{norm} N_{bkg}(> 25)$	6.7	4.2	45.1	25.4
$N_{sig}(> 25)$	213	98	1580	639
$f_{qcd} \pm \sigma_{stat}$	3.1 ± 0.5	4.2 ± 1.4	2.8 ± 0.5	4.0 ± 1.3
$\pm \sigma_{syst} (\%)$	± 0.1	± 0.2	± 0.1	± 0.1

Table 4.13: Summary of the W QCD di-jet background calculation for the four different conditions (two isolation cone sizes, CC and EC calculated separately).

factor was calculated for two other intervals in \cancel{E}_T , 0 - 5 GeV and 0 - 15 GeV. The systematic error was taken to be the largest difference between any two of the three calculated normalization factors; the small error reflects the good agreement in the shape of the signal and background distributions in the normalization region. As expected, there is less QCD background with $\mathcal{R}_{iso} = 0.6$, since that cut is tighter.

In order to obtain an overall QCD background fraction for the W sample, the four numbers are combined, using the relative luminosity fractions to combine the values for the different cone sizes, then using the actual data distribution to combine the CC and EC results. The amount of data taken using the two isolation cone sizes was nearly equal, with 50.4% of the data taken with $\mathcal{R}_{iso} = 0.6$ and 49.6% taken with $\mathcal{R}_{iso} = 0.4$. Then 70.5% (7,284/10,338) of the W candidates had the electron in the CC while the remaining 29.5% (3,054/10,338) of the events had the signal electron in the EC. Applying these weights leads to an overall QCD di-jet fraction of

$$f_{qcd}^w = 3.3 \pm 0.5\%. \quad (4.30)$$

It should be noted that this is expressed as a fraction of the $W \rightarrow e\nu$ signal candidates (including background), not as a fraction of the real W 's in the sample.

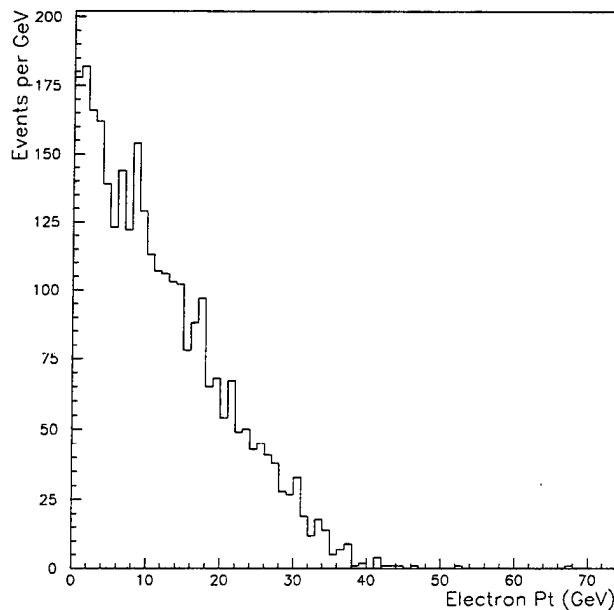


Figure 4.6: Electron p_T distribution for $W \rightarrow \tau \rightarrow e$ events

4.4.1.2 $W \rightarrow \tau \nu$ contamination

Another source of background comes from $W \rightarrow \tau \nu$ events, with the subsequent decay $\tau \rightarrow e \nu$. These events have the same signature as the $W \rightarrow e \nu$ signal events, a real electron and significant \cancel{E}_T . Fortunately, the electron p_T spectrum from these events is much softer, since the electron comes from the secondary decay of the τ , as can be seen in Figure 4.6 [76]. Instead of the Jacobian peak at $M_W/2$, the distribution peaks at low momenta; due to the 25 GeV E_T cut on the electron, this leads to a greatly reduced kinematic acceptance for these events. The amount of $W \rightarrow \tau \nu$ contamination is further reduced by the $\tau \rightarrow e \nu$ branching ratio of roughly 17% [33].

Since the event signatures are identical, the amount of background is determined by the relative acceptances, modified by the probability of the secondary $\tau \rightarrow e \nu$ decay. Assuming the W decays equally into electrons and taus,

$$f_{\tau}^w = \text{Br}(\tau \rightarrow e \nu) \cdot \frac{\mathcal{A}_W^{\tau}}{\mathcal{A}_W^e} \quad (4.31)$$

where $\text{Br}(\tau \rightarrow e\nu)$ is the branching ratio, and \mathcal{A}_W^τ and \mathcal{A}_W^e are the $W \rightarrow \tau\nu \rightarrow e\nu\nu$ and $W \rightarrow e\nu$ acceptances respectively. The calculation of \mathcal{A}_W^e has been described earlier in this chapter; \mathcal{A}_W^τ is calculated in the same way. Taking $\text{Br}(\tau \rightarrow e\nu) = 17\%$ leads to the result

$$f_\tau^w = 1.9 \pm 0.1\% \quad (4.32)$$

where the error is dominated by the Monte Carlo statistics. Note that this is a fraction of true $W \rightarrow e\nu$ events, not a fraction of the candidate sample.

4.4.1.3 $Z \rightarrow ee$ and $Z \rightarrow \tau\tau$ faking $W \rightarrow e\nu$

If one of the Z decay electrons enters a detector crack, there is a good chance it will not be reconstructed as an electron; furthermore there is a good chance that the energy will be mismeasured. Under these conditions, $Z \rightarrow ee$ events form a background to the $W \rightarrow e\nu$ sample, since the final state is the same: one high- p_T electron and a lot of missing transverse energy. It is very difficult to get a handle on this background only based on data, so Monte Carlo data are used to estimate the amount of background.

This study uses data processed by DØGEANT [77], which performs the full detector simulation needed to accurately model the detector response to electrons in badly instrumented regions, like the CC cracks or the inter-cryostat region. A total of 10,000 $Z \rightarrow ee$ events and 6,000 $W \rightarrow e\nu$ events were generated and passed through DØGEANT. The two samples were then passed through the standard reconstruction, and the W selection cuts were applied to each sample; 200 of the Z events passed the cuts, while 1888 of the W events passed the cuts. The contamination is then simply the production ratio times the ratio of the DØGEANT-based acceptances:

$$f_z^w = \frac{\sigma(p\bar{p} \rightarrow Z \rightarrow ee)}{\sigma(p\bar{p} \rightarrow W \rightarrow e\nu)} \cdot \frac{A_{Z \rightarrow W}}{A_W} = \frac{\sigma(p\bar{p} \rightarrow Z \rightarrow ee)}{\sigma(p\bar{p} \rightarrow W \rightarrow e\nu)} \cdot \frac{\frac{200}{10,000}}{\frac{1888}{6000}} \quad (4.33)$$

where $A_{Z \rightarrow W}$ and A_W are the fractions of Z and W events that pass the W selection cuts respectively.

The production ratio $\sigma(p\bar{p} \rightarrow Z \rightarrow ee)/\sigma(p\bar{p} \rightarrow W \rightarrow e\nu)$ is taken to be 0.1, which is close to both experimental values and results of theoretical calculations; a 10% error is assigned to this quantity. The calculation was performed with and without making the standard \cancel{E}_T corrections; the error due to the \cancel{E}_T corrections is taken to be the difference between the two results. Finally, including the statistical error, the contamination in the W sample is found to be

$$f_z^w = 0.6 \pm 0.1\% \quad (4.34)$$

Like the tau background, this is a fraction of real W bosons, not of the candidate sample.

The process $Z \rightarrow \tau\tau$ with at least one subsequent $\tau \rightarrow e\nu$ decay can also contribute to the W background. The electrons from the τ decay have the same soft p_T spectrum as in the $W \rightarrow \tau \rightarrow e$ events. Taking into account the soft electron and the additional $\tau \rightarrow e\nu$ branching ratio factor compared to the $Z \rightarrow ee$ background, this background source is negligible, and can safely be ignored.

4.4.2 Background in the $Z \rightarrow ee$ Sample

The requirement of two clean, high- p_T electrons in the Z selection forms a unique signature; nevertheless, there are sources of background. The primary source of background comes from QCD multi-jet events, where jets fluctuate to fake electrons. Drell-Yan events (where two real electrons are produced via a virtual photon) provide another source of background. Another source of two real electrons is the process $Z \rightarrow \tau\tau \rightarrow ee\nu\nu$.

4.4.2.1 QCD Background

QCD processes form the primary background to the $Z \rightarrow ee$ sample. There are two sources: di-jet events, where both jets fake electrons, and direct photon events, where the photon satisfies the cuts for one of the electrons and the other electron is

really a jet. The invariant mass shape of the Z sample is used to measure the amount of QCD background present, since the falling invariant mass spectrum of the QCD processes differs greatly from the invariant mass peak at M_Z due to the true $Z \rightarrow ee$ events. A good understanding of the shape of each sample (di-jet, direct photon and signal) is necessary to perform this analysis.

The invariant mass shape of the di-jet events is measured using events selected from the JET_MIN trigger [78]. Offline, the events were required to have two jets with $E_T > 25$ GeV in the fiducial region of the detector used for this analysis. The spectrum is shown in Figure 4.7. The sample was normalized based on the luminosity in the Z sample and the electron-fake rates measured for the specific selection cuts. A two-parameter exponential fit to the distribution was performed in the mass range 65 - 250 GeV [79]:

$$N_{di-jet}(m) = e^{0.776-0.0237m} = 2.17e^{-0.0237m} \quad (4.35)$$

This fit is shown, superimposed over the data, in Figure 4.7.

The direct photon invariant mass spectrum has been measured and parametrized by the DØ direct photon group [80]. The spectrum is shown in Figure 4.8; it is normalized to the Z sample luminosity, using a nominal jet-fake rate of 0.1%. The superimposed fit is exponential:

$$N_{\gamma-jet}(m) = e^{0.736-0.0345m} = 2.09e^{-0.0345m} \quad (4.36)$$

The PYTHIA event generator [81] was used to generate the full $p\bar{p} \rightarrow Z/\gamma \rightarrow ee$ mass spectrum, which contains the Drell-Yan and interference term contributions as well as the pure Z term. Detector resolution and QED radiation effects were applied to the sample, and then the appropriate kinematic and fiducial cuts were applied. The resultant mass distribution, $N_{Z/\gamma}(m)$, is shown in Figure 4.9.

In order to determine the amount of QCD background in the Z sample, a fit is performed to the sum of the mass shapes of the signal and background. The invariant mass distribution of the data $N_{data}(m)$ is expressed as the sum of the signal

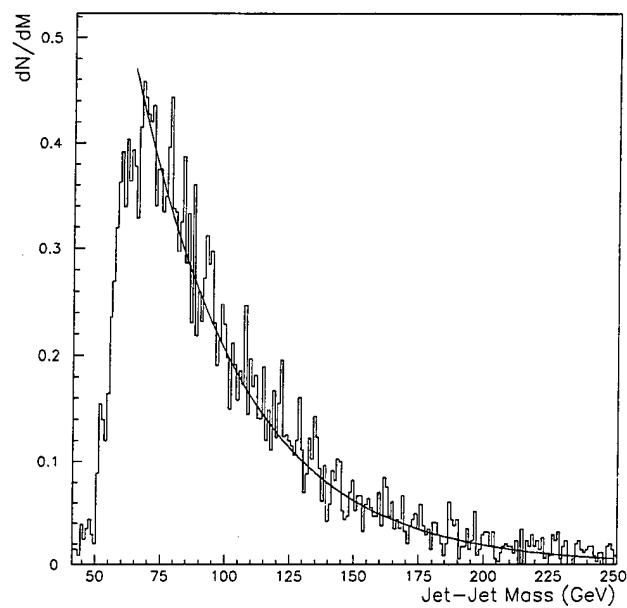


Figure 4.7: QCD di-jet invariant mass spectrum, with exponential fit superimposed.

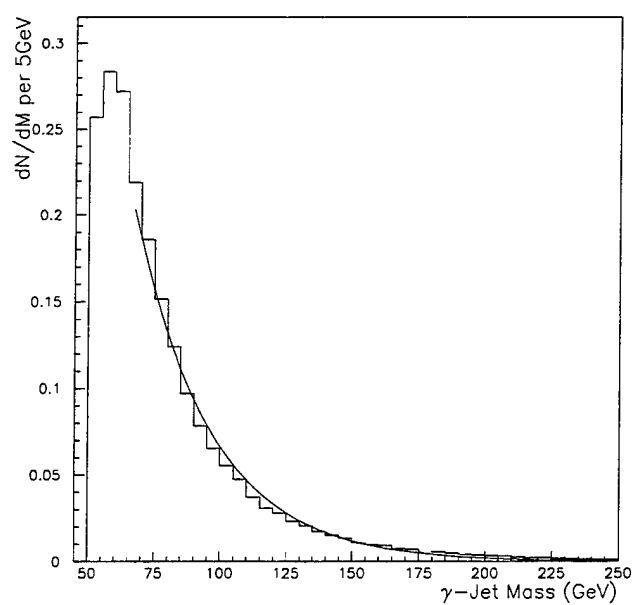


Figure 4.8: The QCD direct photon invariant mass spectrum, with exponential fit superimposed.

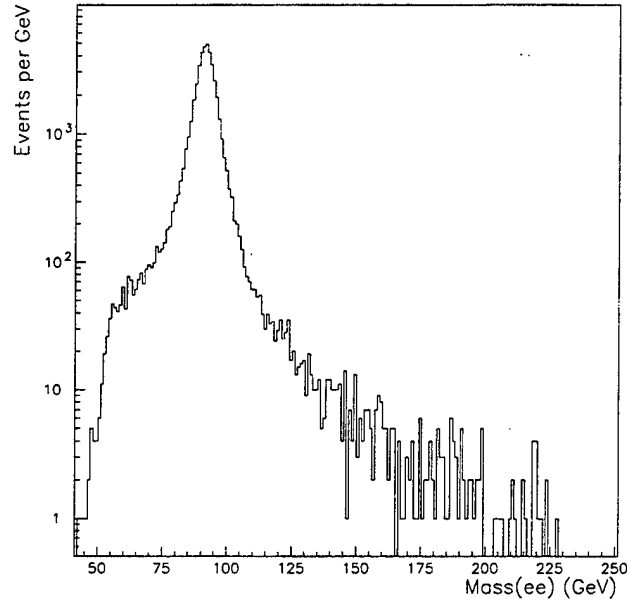


Figure 4.9: Z/γ invariant mass distribution.

and background distributions:

$$N_{data}(m) = c_1 \cdot N_{Z/\gamma}(m) + c_2 \cdot N_{bkg}(m) \quad (4.37)$$

where c_1 and c_2 are the normalization factors of the signal and background respectively. The total number of data events (integrated over invariant mass) is known, as is the integral of $N_{Z/\gamma}(m)$ and $N_{bkg}(m)$; integrating both sides of Equation 4.37 leads to

$$N_{data}^{tot} = c_1 \cdot N_{Z/\gamma}^{tot} + c_2 \cdot N_{bkg}^{tot} \quad (4.38)$$

This equation is used to solve for c_1 in terms of c_2 and known quantities; inserting this back into Equation 4.37 gives

$$N_{data}(m) = \frac{N_{data}^{tot} - c_2 \cdot N_{bkg}^{tot}}{N_{Z/\gamma}^{tot}} \cdot N_{Z/\gamma}(m) + c_2 \cdot N_{bkg}(m) \quad (4.39)$$

There is only one parameter, c_2 , to determine in the fit. A maximum likelihood fit is performed to determine this parameter.

I. $f_{bkg}(m) = f_{di-jet}(m)$	
Mass Fitting Range	c_2
61.2 - 121.2 GeV	3.75 ± 1.00
71.2 - 121.2 GeV	3.70 ± 1.20
II. $f_{bkg}(m) = f_{di-jet}(m) + f_{\gamma-jet}(m)$	
Mass Fitting Range	c_2
71.2 - 121.2 GeV	2.75 ± 1.00
71.2 - 111.2 GeV	2.25 ± 1.06
75.2 - 121.2 GeV	1.38 ± 1.06
77.2 - 121.2 GeV	1.75 ± 1.13

Table 4.14: Summary of fit results for $Z \rightarrow ee$ QCD background

First, the background was taken to be only QCD di-jets, so $N_{bkg}(m) = N_{di-jet}(m)$. The results of the fit for two different fitting ranges are shown in Part I of Table 4.14. If the normalization procedures used in determining the background shape were correct, then the value of c_2 would be close to 1. In this case, however, the fitted value is several sigma away from the expected result, indicating either poor normalization, or that there is additional background to be taken into account.

Next, the shape of the background is taken to be the sum of the measured di-jet and direct photon background shapes: $N_{bkg}(m) = N_{di-jet}(m) + N_{\gamma-jet}(m)$. The results of the fit are shown in Part II of Table 4.14 for several ranges in invariant mass. The results still suggest that the background normalization is too low, but considering the error in the fit and the errors associated with the background normalization (such as the errors in the electron-fake rate and in the di-jet cross section), the agreement is reasonable.

The fitted value for c_2 varies significantly with the fitting range, due to fluctuations in the data sample at the edges of the selected ranges. For the actual calculation of the amount of QCD background, the following nominal value is chosen:

$$c_2 = 2.00 \pm 1.00 \quad (4.40)$$

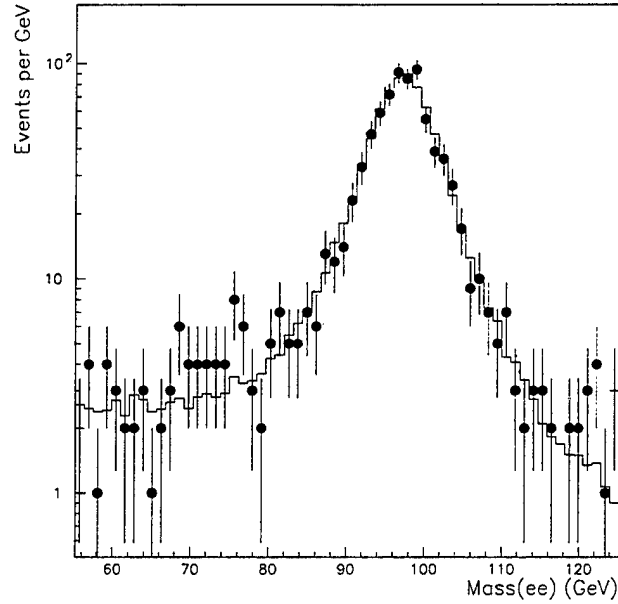


Figure 4.10: Comparison of $Z \rightarrow ee$ data (points) with Monte Carlo plus predicted background (histogram), with $c_2 = 2.00$.

Based on this value, the Z data are compared to the sum of the Monte Carlo signal and predicted background in Figure 4.10; the agreement is good, with a χ^2 per degree of freedom of 0.9. Integrating the background over the 75 - 105 GeV invariant mass window used for the signal and multiplying by c_2 , the QCD background fraction is found to be

$$f_{qcd}^z = 2.8 \pm 1.4\% \quad (4.41)$$

By construction, this is the fraction of the signal candidates, not of real Z boson events.

4.4.2.2 Drell-Yan

The same two-electron final state used to identify the Z events can be produced by the Drell-Yan process, $p\bar{p} \rightarrow \gamma^* \rightarrow ee$; there is also a contribution from the $Z - \gamma$ interference term. In order to measure the pure $Z \rightarrow ee$ cross section, the data sample must be corrected for the effect of this background.

The signatures for the Drell-Yan and true $Z \rightarrow ee$ events are identical, so it is necessary to estimate the background using Monte Carlo techniques. Two 100,000 event samples were generated with the PYTHIA generator: one using the full $Z - \gamma$ matrix elements (including interference), and one using only the pure Z matrix element. Each sample was generated with a lower q^2 limit of 50 GeV; the generated samples correspond to cross sections of 15.76 nb for the full sample and 14.74 nb for the Z only sample. For each sample, the z vertex and the electron energies were smeared, then all kinematic and fiducial cuts were applied. To determine the Drell-Yan fraction f_{d-y}^z (really the non-pure Z fraction), the ratio of cross sections inside the 75 - 105 GeV invariant mass window is calculated:

$$1 + f_{d-y}^z = \frac{|\sigma(p\bar{p} \rightarrow Z/\gamma \rightarrow ee)|_{75-105}}{|\sigma(p\bar{p} \rightarrow Z \rightarrow ee)|_{75-105}} \quad (4.42)$$

After all kinematic and fiducial cuts are applied to the smeared samples, there are 35,270 remaining events in the mass window from the full sample, while there are 37,218 remaining pure Z events. Thus,

$$1 + f_{d-y}^z = \frac{(35,270/100,000) \cdot 15.76 \text{ nb}}{(37,218/100,000) \cdot 14.74 \text{ nb}} = 1.013 \quad (4.43)$$

The statistical error associated with this result is negligible. To determine a systematic error due to the generator used, the calculation was repeated using ISAJET [82], and the results were consistent. The results were calculated using different combinations of kinematic and fiducial cuts, and the variation was small. Finally, the Drell-Yan fraction is measured to be

$$f_{d-y}^z = 1.3 \pm 0.1\% \quad (4.44)$$

This is expressed as a fraction of real Z bosons, not a fraction of the signal sample.

Another potential source of background is the Drell-Yan production of taus: $p\bar{p} \rightarrow \gamma^* \rightarrow \tau\tau$. This background is negligible, because of the two electronic branching ratio factors, and the soft spectrum of the decay electrons from taus.

4.4.2.3 $Z \rightarrow \tau\tau$

Another potential background source comes from the process $Z \rightarrow \tau\tau$, where both taus subsequently decay into electrons. The Z decays into taus at the same rate as into electrons; however, the soft p_t spectrum of the decay electrons and the additional factors of the $\tau \rightarrow e\nu$ branching ratio make this background negligible. To test this, 900 $Z \rightarrow \tau\tau \rightarrow ee$ events were generated and passed through detector simulation. Only one event from this sample survived the kinematic cuts and fell within the invariant mass window. Taking into account the two 17% branching ratio factors, the acceptance for $Z \rightarrow \tau\tau \rightarrow ee$ is negligible, and this source of background can safely be ignored.

Chapter 5

Luminosity

One of the most important parts of any cross section measurement is the determination of the integrated luminosity, a measure of how many $p\bar{p}$ interactions went into the data sample used for the analysis. It is essential that this quantity is measured as accurately as possible, since any error is transferred directly to the cross section measurement itself. To calculate the luminosity, two inputs are needed: the total number of $p\bar{p}$ interactions used in the analysis, and the total $p\bar{p}$ cross section visible to the triggering system. Care must be taken to properly account for any dead time, and careful data handling and bookkeeping is essential.

5.1 Instantaneous Luminosity

Hard-core, inelastic $p\bar{p}$ collisions are detected with high efficiency by the Level- \emptyset trigger. The measured instantaneous luminosity is directly proportional to the firing rate $R_{L\emptyset}$ of the Level- \emptyset system:

$$\mathcal{L}_m = \frac{R_{L\emptyset}}{\sigma_{L\emptyset}} \quad (5.1)$$

where $\sigma_{L\emptyset}$ is the $p\bar{p}$ cross section visible to the Level- \emptyset system (known as the Level- \emptyset monitor constant) which is described below. For a given crossing, the Level- \emptyset system

can either fire or not fire; there is no distinction made between a single-interaction beam crossing and a crossing which contains multiple interactions. As a result, the direct proportionality breaks down at high luminosity, where there is an appreciable chance for such multiple interactions.

5.1.1 Multiple Interaction Correction

Poisson statistics can be used to determine a correction scheme to handle multiple interactions. At a given luminosity, the average number of interactions per crossing is given by [83]

$$\bar{n} = \mathcal{L} \cdot \tau \cdot \sigma_{L\emptyset} \quad (5.2)$$

where τ is the time between beam crossings ($\tau = 3.5 \mu\text{s}$ at the Tevatron) and \mathcal{L} is the true instantaneous luminosity. The measured number of interactions per crossing ignoring multiple interactions is $1 - p(0)$, where $p(0)$ is the Poisson probability of having zero interactions in a crossing. The ratio of actual luminosity to measured luminosity is given by the ratio of the average number of events per crossing:

$$\frac{\mathcal{L}}{\mathcal{L}_m} = \frac{\bar{n}}{1 - p(0)} = \frac{\bar{n}}{1 - e^{-\bar{n}}} \quad (5.3)$$

Incorporating the expressions given above for \bar{n} and \mathcal{L}_m and doing a bit of algebra leads to

$$\mathcal{L} = \frac{-\ln(1 - R_{L\emptyset} \cdot \tau)}{\sigma_{L\emptyset} \cdot \tau} \quad (5.4)$$

During collider running at the Tevatron, there are six bunches each of protons and antiprotons, so for a given interaction point there are six distinct $p\bar{p}$ bunch-pairs. In general, the different bunches are not equally populated, so the multiple interaction probability can be different for different bunch-pairs. To deal with this situation, the Level- \emptyset rate is recorded separately for each of the six bunches, so the correction can be applied independently.

5.1.2 The Level-Ø Monitor Constant $\sigma_{L\emptyset}$

In order to calculate the luminosity, it is necessary to know the total $p\bar{p}$ cross section subtended by the Level-Ø system. The total cross section can be separated into elastic and inelastic processes:

$$\sigma_{tot} = \sigma_{el} + \sigma_{inel} \quad (5.5)$$

Furthermore, the inelastic part can be broken down into hard-core, single-diffractive and double-diffractive processes:

$$\sigma_{inel} = \sigma_{HC} + \sigma_{SD} + \sigma_{DD} \quad (5.6)$$

In $p\bar{p}$ single-diffraction dissociation, either the p or the \bar{p} is transformed by a low-momentum-transfer vacuum-exchange into an excited nucleon state, which then decays into a shower of particles surrounding the beam-pipe. In double-diffraction processes, both the p and the \bar{p} produce showers around the beam-pipe. The hard-core scattering processes, which involve large momentum transfer and are highly inelastic, produce the events that form the basis of the physics interest in $p\bar{p}$ collider physics. The Level-Ø trigger is designed to be very efficient at detecting beam crossings containing hard-core inelastic collisions; diffractive and elastic scattering events rarely form a coincidence. The Level-Ø luminosity constant $\sigma_{L\emptyset}$ is obtained by applying the measured efficiencies and acceptances of the Level-Ø system to the various components of the total $p\bar{p}$ cross section at $\sqrt{s} = 1.8$ TeV.

The total $p\bar{p}$ cross section $\sigma_{p\bar{p}}$ has been measured independently by Fermilab experiments E710 [84] and CDF [85]; DØ forms a ‘world average’ of these two measurements. The cross sections reported by the two experiments are significantly different, so some care was taken in combining them. In particular, the χ^2 of the probability that the two combined values are the same within errors is calculated, and the errors on the combined cross sections are scaled by χ [83]. The total $p\bar{p}$ cross sections are summarized in Table 5.1.

	CDF	E710	Combined	Error Scale	Final Average
σ_{el}	19.70 mb	16.6 mb	19.0 mb	1.7	19.02 mb
Error	0.85	1.6	0.8		1.28
σ_{inel}	60.33 mb	55.5 mb	58.9 mb	1.85	58.94 mb
Error	1.40	2.2	1.2		2.19
σ_{SD}	9.46 mb	11.7 mb	9.5 mb	1.0	9.54 mb
Error	0.44	2.3	0.4		0.43

Table 5.1: Total elastic, inelastic and single diffractive cross sections at $\sqrt{s} = 1.8$ TeV. The Error Scale is defined in the text.

The final component that is needed is the double-diffractive cross section σ_{DD} . This quantity is not measured, but rather derived from the elastic cross section σ_{el} and the single-diffractive cross section σ_{SD} . Based on the idea of factorization (see Figure 5.1), the following assumption is made:

$$\frac{\sigma_{DD}}{\sigma_{SD}} \approx \frac{\sigma_{SD}}{\sigma_{el}} \quad (5.7)$$

The single-diffractive cross section listed in Table 5.1 contains equal contributions from either the p or \bar{p} diffracting; in calculating the double diffractive cross section, only half of the total single-diffractive cross section should be used. This leads to the following expression for the double-diffractive cross section:

$$\sigma_{DD} = \frac{\sigma_{SD}^2}{4\sigma_{el}} \quad (5.8)$$

The calculation of the double-diffractive cross section is summarized in Table 5.2. A 10 % systematic error is added to the final average to account for the factorization assumption.

The part of the inelastic cross section that is relevant to the physics processes being studied is the hard-core component σ_{HC} , which is just the total inelastic cross section with the diffractive parts subtracted out:

$$\sigma_{HC} = \sigma_{inel} - \sigma_{SD} - \sigma_{DD} \quad (5.9)$$

	CDF	E710	Combined	Factorization Error	Final Average
σ_{DD}	1.14 mb	2.1 mb	1.15 mb		1.15 mb
Error	0.12	0.8	0.12	0.115 mb	0.17

Table 5.2: Double-diffractive cross section calculation.

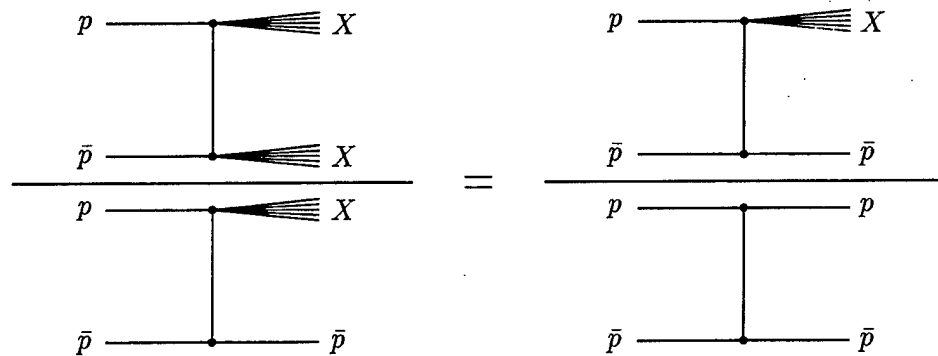


Figure 5.1: A schematic diagram illustrating the assumption that $\sigma_{DD}/\sigma_{SD} = \sigma_{SD}/\sigma_{el}$, based on the idea of factorization (essentially, the p vertex is independent of the \bar{p} vertex).

Using the numbers from the tables above leads to the value $\sigma_{HC} = 48.25 \pm 2.23$ mb.

In order to use the above inelastic cross sections to calculate the Level-Ø luminosity constant, it is necessary to determine the acceptance of the Level-Ø system for each type of inelastic event, as well as measure the overall efficiency of the system, given that charged particles pass through both the north and south counter arrays. The luminosity constant is calculated as follows:

$$\sigma_{LØ} = \epsilon_{LØ}(\mathcal{A}_{SD}\sigma_{SD} + \mathcal{A}_{DD}\sigma_{DD} + \mathcal{A}_{HC}\sigma_{HC}) \quad (5.10)$$

where $\epsilon_{LØ}$ is the overall efficiency of the trigger counters (given both counter arrays are hit by charged particles), and \mathcal{A}_{SD} , \mathcal{A}_{DD} and \mathcal{A}_{HC} are the acceptances of the Level-Ø system for single-diffractive, double-diffractive and hard-core events respectively (the acceptance gives the fraction of a particular event type which have charged particles pass through both counter arrays).

The Level-Ø efficiency $\epsilon_{LØ}$ is determined using data collected by triggering on random beam crossings (zero-bias data). Events with no in-time hits on either end are used to measure the pedestal of the Level-Ø signals. To study the efficiency for one end, events are selected using in-time hits on the opposite end; the pedestal is subtracted, and the remaining fraction of events that have a good fast z signal is taken to be the efficiency for that end. The overall Level-Ø efficiency is the product of the efficiencies for the two ends; the result is $\epsilon_{LØ} = 0.95 \pm 0.02$.

The acceptances for the inelastic $p\bar{p}$ processes are studied using two independent Monte Carlo generators, MBR [86] and DTUJET [87]. The MBR generator is based on CDF multiplicity studies, while DTUJET is based on the dual parton model. Each generator can generate single-diffractive, double-diffractive and hard-core events; a 1000 event data sample of each event type was generated using both generators (for a total of six data samples). A full detector simulation (DØGEANT) was applied to each sample, then they were run through the standard reconstruction software. The measured acceptance was the fraction of events in each sample with a charged particle passing through both Level-Ø counter arrays. The two generators agree fairly

	MBR	DTUJET	Combined
\mathcal{A}_{SD}	$20.5 \pm 1.3 \%$	$9.7 \pm 0.9 \%$	$15.1 \pm 0.8 \pm 5.4 \%$
\mathcal{A}_{DD}	68.5 ± 1.5	74.7 ± 1.6	$71.6 \pm 1.1 \pm 3.1$
\mathcal{A}_{HC}	95.2 ± 0.7	99.0 ± 0.7	$97.1 \pm 0.5 \pm 1.9$

Table 5.3: Level-0 Acceptances

well with each other; cross-checks against zero-bias data also show good agreement. Results from the two generators are averaged to get the final acceptances; a systematic error of half the difference between the results from the two generators is applied to the result. The acceptances are summarized in Table 5.3.

Plugging all the numbers into equation 5.10, the Level-0 luminosity constant σ_{L0} is calculated to be 46.7 ± 2.5 mb. Roughly 95 % of that cross section is due to hard-core processes; the remainder is due to diffractive processes. The calculation of σ_{L0} is summarized in Table 5.4.

	$\mathcal{A}_{SD}\sigma_{SD}$	$\mathcal{A}_{DD}\sigma_{DD}$	$\mathcal{A}_{HC}\sigma_{HC}$	$\sum \mathcal{A}\sigma$	ϵ_{L0}	σ_{L0}
Value	1.44 mb	0.82 mb	46.85 mb	49.11 mb	0.95	46.65 mb
Error	0.53	0.094	2.39	2.45	0.02	2.53

Table 5.4: Calculation of σ_{L0}

5.2 Integrated Luminosity

In order to determine the total luminosity used in the cross section analysis, the instantaneous luminosity \mathcal{L} must be integrated over the live running time used to collect the data. The information needed to calculate \mathcal{L} is stored periodically; the period is chosen to be small enough so that \mathcal{L} does not vary significantly, thus avoiding

problems related to nonlinearity at high luminosities.

An important aspect of calculating the integrated luminosity is correctly determining the fraction of crossings for which the detector is "live." There are many sources of dead time, such as main ring activity, Level-2 trigger saturation (where there are no Level-2 nodes available to process an event), front-end busy (which means that the front-end digitizing electronics is not ready to process data from the detector), or a prescale (where only a certain fraction of events are given the chance to pass a given trigger condition). In general, a physics run has several different triggers; each trigger can have different live-times, and enough data has to be stored in order to calculate each of those live-times separately.

5.2.1 Storing Luminosity Information

The instantaneous luminosity can be determined just by looking at the firing rate of the Level-0 system on the fly. In order to calculate the integrated luminosity, the Level-0 information must be stored periodically, so that the instantaneous luminosity can be integrated over the running period. To facilitate the integration, the period is chosen to be short enough so that \mathcal{L} does not change appreciably, and the integration becomes a simple sum:

$$\int \mathcal{L} dt = \sum_{i=1}^n \bar{\mathcal{L}}_i \cdot \Delta t_i \quad (5.11)$$

where $\bar{\mathcal{L}}_i$ is the average instantaneous luminosity for the i^{th} time period, Δt_i is the time period between the i^{th} and $i+1^{th}$ reading, and the sum goes over the period of live data-taking.

The Level-0 rates are tallied in scalers contained within the Level-1 trigger framework. Separate counts are kept for each of the six $p\bar{p}$ bunch-pairs, to allow for unequal bunch population. Level-1 scalers also keep track of the number of bunch crossings that are vetoed due to main ring activity, the inability of the data acquisition system to accept another event (front-end busy, Level-2 busy, etc.), or other dead-time sources not directly related to the physics requirements of the Level-1 triggers. Fi-

nally, Level-1 scalers also keep track of the prescales applied to each of the Level-1 specific trigger bits (the scaler associated with a given trigger bit is only incremented for an otherwise live crossing where the bit has been disabled due to a prescale).

The Level-1 scaler information, along with some other relevant information from the accelerator and the data acquisition systems, is read out and stored roughly once per minute by the Luminosity Database Server, a program that runs in the background on the online computer system. This program provides the information to online monitoring systems, as well as storing the information in a database once every ten minutes (which is a short time period compared to the typical lifetime of a store, which can be on the order of a day). The database contains all the information necessary to calculate the integrated luminosity for a selected Level-1 specific trigger on a run-by-run basis.

5.2.2 Live-Time Determination

Ideally, DØ would be ready to take data from any $p\bar{p}$ crossing within the detector. In reality, however, there are several sources of dead-time, which prevent collecting data at 100 % efficiency.

One of the main sources of inefficiency is the presence of the Main Ring in the coarse hadronic calorimeter. Losses from the beam in the Main Ring cause unacceptable background in the regions of the calorimeter surrounding the Main Ring beam-pipe; therefore, during periods of high main ring losses, the DØ trigger is disabled.

The finite bandwidth of the data acquisition system is another significant source of dead-time. There are a limited number of Level-2 nodes available to process an event that passes the Level-1 requirements; if all the nodes are busy (Level-2 busy), the Level-1 trigger framework is disabled. The Level-1 system is also disabled if the front-end digitizing electronics is not ready to process an event (front-end busy).

One final significant source of dead-time comes from pauses in the run, or time

between runs. The length of a run is limited, in order to keep conditions during the run relatively constant, and because only a limited number (99) of fixed size files can be written by the data acquisition system for a given run. There are often short pauses in a run, usually caused by the need to take care of a hardware problem that compromises the quality of the data. The most common of these problems is a detector high voltage trip.

In order to obtain an accurate integrated luminosity, it is essential to keep careful account of the live-time. In principle, each Level-1 specific trigger bit can have a different live-time, due to different trigger requirements. In practice, however, practical considerations make keeping track of live-time separately for each trigger bit impossible, due to hardware restrictions. Basically, there are not enough Level-1 scaler channels available: for each of the 32 Level-1 trigger bits, six scaler channels (one per bunch-pair) would be necessary. Furthermore, since the trigger conditions are defined at run time, the logic driving the scalers would have to be fully programmable (to the same level as the trigger-decision circuitry itself); at this time, the Level-1 framework does not have such flexibility.

Since it is not possible to treat each trigger bit independently with respect to keeping track of the live-time, it is necessary to give up a bit of generality. In order to make the live-time calculable, it is necessary to demand that all sources of non-physics dead-time affect each Level-1 trigger bit the same. With this condition imposed, it is possible to dedicate one of the Level-1 trigger bits (bit 30) to keeping track of the live-time fraction. This trigger bit is set up so that it is not prescaled, contains no physics conditions (as long as the detector is ready to take data for a given collision, it will fire), and never generates an actual Level-1 trigger. The signal from bit 30 ANDed with the output of the Level-0 system gives the number of live crossings containing at least one detected interaction. This number, scaled by the Level-0 luminosity constant σ_{L0} , gives the integrated luminosity for a given time period, in the absence of multiple interaction corrections.

It is often desirable (and necessary) to balance the available data acquisition band-

width between the different Level-1 specific triggers (that is, choose the important physics triggers that should get most of the bandwidth). The requirement of symmetry between the triggers precludes making several classes of Level-2 nodes (dedicating more nodes to the important triggers), or reading out only a subset of the front-end crates for some triggers (in order to reduce the bandwidth necessary to read out an event). All Level-2 nodes (excluding SHADOW nodes, which are often used for Level-2 testing, and do not generate a Level-2 busy) must be available to all Level-1 trigger bits. Furthermore, the front-end busy signal must affect all Level-1 triggers the same, so the same set of crates must be read out for all trigger bits during data-taking. As a result, load balancing between Level-1 trigger bits must be accomplished either through threshold adjustment, or by using a fixed prescale. Scalers for each Level-1 trigger bit count how many events make it through the applied prescale; by comparing the counter for each physics specific trigger to the counter for the special trigger bit 30 (which is unprescaled), the actual applied prescale can be calculated (and used when calculating the integrated luminosity). Note that the prescale is assumed to be independent of bunch (only one scaler is used for each specific trigger, instead of six).

The physics Level-1 triggers are based on either calorimeter or muon data (or both), which is available (in some form) in time to make a trigger decision in the short time available between crossings. Some specific triggers make further requirements, not based on that physics data, such as requiring the Level-0 system to indicate only one vertex, or that there be no main ring activity at the time of the crossing. In general, these requirements are not common to all the physics triggers; in order to properly calculate the integrated luminosity for triggers making such requirements, it is necessary to use scalers to keep track of the live-time losses due to the imposed conditions, on a per-bunch basis. The scaler totals, ANDed with the Level-0 output and the special trigger bit 30, gives the correction to be applied to the appropriate physics triggers.

All of the scaler values are stored in the luminosity database by the Luminosity Server every ten minutes. With all the scaler information available, it is possible to

do all the appropriate corrections, including the correction for multiple interactions.

5.2.3 Performing the Integration

The integral quoted previously (Equation 5.11) must be modified to include the live-time calculation. The total integrated luminosity recorded by the DØ detector for a given ten minute time period is given by the number of live crossings, divided by the monitor constant. The calculation is done separately for each bunch:

$$\Delta \mathcal{L}_b^i = \int_{t_i}^{t_{i+1}} \mathcal{L} dt = \frac{N_{L\emptyset}^{live}(i, b)}{\sigma_{L\emptyset}} \quad (5.12)$$

where

$$N_{L\emptyset}^{live}(i, b) = N_{L\emptyset}^{raw}(i, b) \otimes N_{live}(i) \quad (5.13)$$

and $b = (1, \dots, 6)$ is the bunch-pair index, i is the time period index, $N_{L\emptyset}^{live}(i, b)$ is the number of live crossings for bunch b in time period i , $N_{L\emptyset}^{raw}(i, b)$ is the total number of crossings which pass Level-Ø and $N_{live}(i)$ is the total number of live crossings for time period i . The product $N_{L\emptyset}^{raw}(i, b) \otimes N_{live}(i)$ gives the number of crossings where the detector was live *and* the Level-Ø system fired for bunch b ; the symbol \otimes is used here to indicate a logical AND instead of an arithmetic multiplication.

Several corrections must be applied to the above calculation. First of all, the luminosity has to be corrected for multiple interactions, separately for each time period (note that the full rate out of Level-Ø is used when calculating the multiples correction factor, not the rate convoluted with the live signal). For specific physics triggers, corrections for non-physics terms are also applied separately for each time period. Finally, the correction for prescaling is applied; this is assumed to be luminosity and bunch independent, so it is applied after the sum over time periods and bunches has been performed. For a given specific trigger T , the total integrated luminosity for a run can be expressed as follows [88]:

$$\int_{run} \mathcal{L}(T) dt = \left(\sum_{i,b} \frac{N_{L\emptyset}^{live}(i, b)}{\sigma_{L\emptyset}} \cdot M(i, b) \cdot NP(i, b, T) \right) \cdot P(T) \quad (5.14)$$

where $M(i, b)$ is the multiple interaction correction factor, $NP(i, b, T)$ is the correction for non-physics conditions appropriate to trigger T , and $P(T)$ is the prescale correction (which can include both Level-1 and Level-2 prescales).

5.2.4 Alternative: Minimum-bias and Zero-bias events

An alternative approach to calculating the integrated luminosity for a run is to count the number of minimum-bias events taken, and use the known minimum-bias cross section to calculate the luminosity of the run. A minimum-bias event just requires a good fast z signal from Level-0; needless to say, a large prescale is applied to the minimum-bias trigger in order to keep the bandwidth used for these events small. In order to handle the correction for multiple interactions, a Poisson distribution is assumed for the number of interactions, and zero-bias events (events with no trigger requirements at all, not even a good Level-0 signal) are taken, which makes it possible to calculate the probability that there are zero interactions in a crossing.

The integrated luminosity for a run is just the total number of interactions (including multiples) divided by the luminosity constant. The total number of interactions is the total number of crossings times the average number of interactions per crossing. Furthermore, the total number of crossings is just the live-time for the run times the crossing frequency. In summary:

$$\int_{run} \mathcal{L} dt = \frac{f \cdot \overline{N} \cdot t_{live}}{\sigma_{L0}} \quad (5.15)$$

where f is the crossing frequency ($= 286275 \text{ sec}^{-1}$) and $\sigma_{L0} = 46.7 \text{ mb}$ is the Level-0 luminosity constant described above.

Assuming Poisson statistics, the average number of interactions can be calculated from the probability for zero interactions:

$$\overline{N} = -\ln(\text{Prob}(0)) \quad (5.16)$$

The probability for zero interactions in a crossing is the complement of the probability of there being at least one interaction in a crossing, which is calculable using the

number of minimum bias and zero-bias events, and their associated prescales:

$$\text{Prob}(0) = 1 - \frac{N_{MB} \cdot P_{MB}}{N_{ZB} \cdot P_{ZB}} \quad (5.17)$$

where N_{MB} and N_{ZB} are the number of minimum bias and zero-bias events collected for the run respectively, and P_{MB} and P_{ZB} are the associated prescales (Level-1 and Level-2 combined).

The zero-bias events are used to determine the total live-time for the run. The number of live crossings is just $N_{ZB} \cdot P_{ZB}$; dividing by the crossing frequency gives the live-time:

$$t_{live} = \frac{N_{ZB} \cdot P_{ZB}}{f} \quad (5.18)$$

Combining everything leads to the following expression for the integrated luminosity for a run:

$$\int_{run} \mathcal{L} dt = \frac{-N_{ZB} \cdot P_{ZB} \cdot \ln(1 - \frac{N_{MB} \cdot P_{MB}}{N_{ZB} \cdot P_{ZB}})}{\sigma_{L\bar{L}}} \quad (5.19)$$

Since the minimum-bias and zero-bias events are of very little physics interest, they are prescaled very heavily so that very little of the available bandwidth is used. As a result, the integrated luminosity calculation based on these events has a large statistical error, especially for short runs. For a large set of runs, the statistical error becomes acceptably small, and this method is used as a valuable check of the luminosity calculated using the Level-1 scalers (and for runs where the scaler information is not available for various reasons, the luminosity based on the minimum bias events is used as the primary measure).

5.3 Luminosity Bookkeeping

The luminosity database is populated by the Luminosity Server, and contains the raw information needed to calculate the integrated luminosity for each run. This database is not very practical for physics analysis, however. In order to simplify the determination of the integrated luminosity for physics analyses, the raw luminosity

information is processed, and made available in a more useful location, the production database. For a given run, this database contains information describing the run-time conditions, as well as a record of what data processing has been done. Information from this database can be easily accessed in a form directly useful for analysis.

5.3.1 Production Database

For a given run, a lot of information is stored in the production database: the total number of events, luminosity information, trigger and filter information, the time of the run, and much more. In addition, the database contains a record of all of the data files available for the run, including the RAW data as written during data-taking, STANDARD output files (STAs) and Data Summary Tapes (DSTs) produced by the first-pass reconstruction of the data, as well as other files produced by later streaming or filtering of the data. For each of the files associated with a run, the production database stores the number of events, as well as a history of how the file was produced (a trace back to the original RAW data files).

For each run, the production database stores the integrated luminosity, calculated using the Level-1 scaler information, as well as with the number of minimum bias and zero-bias events. In addition, the production database stores all the necessary corrections to the luminosity; these include corrections for multiple interactions, main ring veto, central vertex cut and single interaction cut. The prescale factors are stored along with the trigger and filter information. The luminosity is corrected for multiple interactions before it is stored in the database; all the other corrections are trigger or filter dependent, and must be applied separately.

The data for each run are split into many separate files or partitions, to aid in the handling and processing of the data. The integrated luminosity for each RAW data file is calculated based on the number of events in the partition and the total luminosity of the run:

$$\mathcal{L}_i = \mathcal{L}_{run} \cdot \frac{n_i}{n_{run}} \quad (5.20)$$

where n_i is the number of events in partition i , n_{run} is the total number of events in the run, and \mathcal{L}_i and \mathcal{L}_{run} are the partition and total integrated luminosities, respectively. The number of events in each RAW data partition is stored in the database; this allows the luminosity to be calculated for all the other types of files recorded in the database, since they can be traced back to the corresponding RAW data files. Note that the data from a single partition of RAW data is never split into separate files by the reconstruction, streaming or filtering processes.

Processing and handling all the $D\bar{O}$ data is a huge and complicated task. As a result, events can be lost (perhaps due to a crash in the reconstruction program), as well as whole partitions. The corresponding luminosity is lost for use in physics analysis; it is necessary to be able to calculate how much luminosity is lost due to such bookkeeping problems. This is easily done using the same principle outlined above for calculating luminosities for the individual partitions – the fraction of the run luminosity that is lost is equal to the fraction of the total events that are lost:

$$\frac{\mathcal{L}_{lost}}{\mathcal{L}_{run}} = \frac{n_{lost}}{n_{run}} \quad (5.21)$$

In practice, the files used for the analysis are known, and the trick is to determine what fraction of the events of a run are included. The total luminosity used is then

$$\mathcal{L}_{tot} = \sum_{runs} \mathcal{L}_i \cdot \frac{n_{used}^i}{n_{run}^i} \quad (5.22)$$

where the index i runs over all the runs used in the analysis, and \mathcal{L}_i includes all corrections appropriate for the trigger used in the analysis. Using the file information in the production database, it is easy to determine n_{used} for any given run (given the list of files used from that run).

5.4 Integrated Luminosity of the Data Samples

The W and Z event samples were selected from the ELF-WZ stream, which was filtered by hand using only loose kinematic cuts to identify W or Z candidates in the

electron channel. The ELF_WZ stream was selected from the DST files produced by the reprocessing of all the Run 1A data with version 11 of the standard reconstruction program RECO. In order to calculate the luminosity used for the W and Z cross section data samples, the DST file list used for the ELF_WZ streaming was used as an input to the luminosity utilities.

As outlined in the previous chapter, both the W and Z selection is based on the same Level-2 filter (and hence the same Level-1 trigger): ELE_HIGH. For the most part, this filter was not prescaled, although there were a few isolated runs where a prescale was applied, so determining the prescale correction was necessary. Furthermore, ELE_HIGH was disabled during main ring activity, so a correction for the main ring veto had to be applied.

The list of DST files used for the ELF_WZ streaming was used as an input for the luminosity utilities; for each file, the utility returned both the scaler-based luminosity and the luminosity based on the number of minimum-bias and zero-bias events. For the ELE_HIGH filter, these luminosities must be corrected for the Main Ring veto, and for an occasional non-unity Level-1 or Level-2 prescale. The correction for the Main Ring veto is extracted from the production database, and is calculated based on Level-1 scaler information. For some runs, the scaler information is unavailable, due mainly to computer problems at end-run time; for those runs, a nominal correction of 0.92 was used. The Level-1 prescale factor is also obtained from the Level-1 scaler information; if the scaler information is not available, then the prescale requested in the trigger setup for the run is used [89]. The requested Level-2 prescale is used for the correction factor, since there are no Level-2 scalers available to calculate the actual applied prescale. For nearly all of Run 1A, ELE_HIGH ran without a prescale, so the prescale correction factor is very close to one.

A total of 1071 different runs are included in the ELF_WZ stream; 874 of these are used for the cross section analysis. A total of 42,928 DST files were used as input to the ELF_WZ streaming; 5,539 of these files are from runs unused for the cross section analysis, leaving 37,389 files to be included in the luminosity calculation. Each of

	ELF_WZ Sample	Cross Section Sample
Number of Runs	1071	874
Number of DST files:		
Level-1 Scaler lum used	37,298	33,913
Minimum bias lum used	5,491	3,368
Zero Luminosity	139	108
Total number of DST files	42,928	37,389
Raw Integrated Luminosity	14.89 pb ⁻¹	13.89 pb ⁻¹
Correction Factors:		
Main Ring Veto	0.935	0.935
Level-1 Prescale	0.993	0.992
Level-2 Prescale	0.991	0.990
Total Correction Factor	0.920	0.918
Corrected Luminosity	13.69 pb ⁻¹	12.76 pb ⁻¹
Error (due to $\sigma_{L\emptyset}$)	± 0.73	± 0.68

Table 5.5: Integrated Luminosity Results, using the filter ELE_HIGH

these DST files corresponds to a single run partition, and represents a very small chunk of luminosity. The file luminosities had the appropriate corrections applied, and then the numbers were summed to get a total integrated luminosity for the cross section sample. The error on the result is solely due to the 5.4 % error on the Level- \emptyset luminosity constant $\sigma_{L\emptyset}$; the error due to bookkeeping is negligible in comparison. The luminosity results for the filter ELE_HIGH are summarized in Table 5.5; the integrated luminosity for the cross section sample is measured to be:

$$\int \mathcal{L} dt = 12.76 \pm 0.68 \text{ pb}^{-1} \quad (5.23)$$

The Level-1 scaler-based luminosity was used whenever possible for the DST file luminosities; if the Level-1 scaler information was unavailable, the luminosity based on minimum-bias event counts was used. A small fraction (about 0.3 %) of the files had either no luminosity available from the database, or the database indicated a zero

luminosity. Many of these files did indeed have no luminosity – they represented the last partition of the run, and happened to contain no events. The total luminosity contained in these files is very small (much smaller than the error due to the luminosity constant), and was ignored. In addition, the Level-1 scaler luminosity and minimum-bias luminosities were compared for all files which had both pieces of information; averaging over a sample of 37,200 files, the luminosity based on the Level-1 scaler information is about 2.4 % greater than the luminosity based on the minimum-bias events. Since minimum-bias luminosities are used for less than 10 % of the files used in the cross section sample, the error due to the difference between the two luminosity measurements is negligible compared to the overall luminosity error.

Chapter 6

Results and Conclusion

All of the information necessary to calculate the $p\bar{p} \rightarrow W \rightarrow e\nu$ and $p\bar{p} \rightarrow Z \rightarrow ee$ cross sections has now been presented. The results for the cross section times branching ratio are calculated, and compared with theoretical predictions. Conclusions that can be drawn based on this comparison are discussed. Finally, the future prospects based on a larger data sample are also discussed.

6.1 Cross Section Calculations

It is now straightforward to calculate the W and Z cross sections, since all of the necessary information has been presented, including the number of signal events, the estimated background, the selection efficiencies, the acceptances, and finally the integrated luminosity. These calculations are described below.

6.1.1 Calculation of $\sigma \cdot Br(p\bar{p} \rightarrow W \rightarrow e\nu)$

The following equation is used to calculate the cross section for W production times the branching ratio for electronic decay:

$$\sigma \cdot Br(p\bar{p} \rightarrow W \rightarrow e\nu) \cdot (1 + f_{\tau}^w + f_z^w) = \frac{N_{sig}^w \cdot (1 - f_{qcd}^w)}{\mathcal{A}_w \cdot \varepsilon_w \cdot \int \mathcal{L} dt} \quad (6.1)$$

where f_τ^w , f_z^w and f_{qcd}^w are the background fractions, N_{sig}^w is the number of signal candidate events, \mathcal{A}_w is the total acceptance, ε_w is the total selection efficiency and $\int \mathcal{L} dt$ is the integrated luminosity. Note the different treatment of the background fractions; the QCD di-jet background is measured and expressed as a fraction of the signal sample, while the background from $W \rightarrow \tau$ events and $Z \rightarrow ee$ events faking W bosons is determined as a fraction of the number of real $W \rightarrow e\nu$ events in the sample. The total background can be expressed as follows:

$$f_{bkg}^w = 1 - \frac{1 - f_{qcd}^w}{1 + f_\tau^w + f_z^w} = f_{qcd}^w + f_\tau^{w'} + f_z^{w'} \quad (6.2)$$

where $f_\tau^{w'}$ and $f_z^{w'}$ are now fractions of N_{sig}^w . Using the fact that $N_w = N_{sig}^w(1 - f_{bkg}^w)$, it is easy to show that

$$f_\tau^{w'} = f_\tau^w(1 - f_{bkg}^w) = f_\tau^w \cdot \frac{1 - f_{qcd}^w}{1 + f_\tau^w + f_z^w} \quad (6.3)$$

$$f_z^{w'} = f_z^w(1 - f_{bkg}^w) = f_z^w \cdot \frac{1 - f_{qcd}^w}{1 + f_\tau^w + f_z^w} \quad (6.4)$$

Using the combined background fraction, the cross section expression is somewhat simplified:

$$\sigma \cdot Br(p\bar{p} \rightarrow W \rightarrow e\nu) = \frac{N_{sig}^w \cdot (1 - f_{bkg}^w)}{\mathcal{A}_w \cdot \varepsilon_w \cdot \int \mathcal{L} dt} \quad (6.5)$$

The quantities needed for the cross section calculation are summarized in Table 6.1. Using these numbers, the total (CC and EC combined) cross section times branching ratio is

$$\sigma \cdot Br(p\bar{p} \rightarrow W \rightarrow e\nu) = 2.36 \pm 0.02 \text{ (stat)} \pm 0.07 \text{ (syst)} \pm 0.13 \text{ (lum) nb.} \quad (6.6)$$

The error due to the luminosity uncertainty is separated out since it is clearly dominant. Even ignoring the luminosity error, the systematic error clearly dominates the measurement, so it is not statistics-limited. However, additional statistics in the diagnostic sample used to measure the efficiencies would significantly lower the systematic error.

	CC	EC	Total
N_{sig}^w	7,284	3,054	10,338
Backgrounds(% of N_{sig}^w ; see text):			
QCD Multijet (f_{qcd}^w)	2.95 ± 0.51	4.10 ± 1.36	3.29 ± 0.54
$W \rightarrow \tau\nu$ ($f_{\tau}^{w'}$; see Eqn 6.3)	1.80 ± 0.09	1.78 ± 0.37	1.79 ± 0.13
$Z \rightarrow ee$ ($f_z^{w'}$; see Eqn 6.4)	0.57 ± 0.09	0.56 ± 0.09	0.57 ± 0.09
Total (f_{bkg}^w ; see Eqn 6.2)	5.32 ± 0.51	6.44 ± 1.38	5.65 ± 0.55
Acceptance \mathcal{A}_w (%)	31.88 ± 0.47	14.13 ± 0.29	46.01 ± 0.60
Efficiency ε_w (%)	71.6 ± 1.9	67.6 ± 2.9	70.4 ± 1.7
$\int \mathcal{L} dt$ (pb ⁻¹)	12.76 ± 0.68		

Table 6.1: Summary of quantities needed to calculate the $W \rightarrow e\nu$ cross section. Note that there are no separate measurements of the CC and EC $Z \rightarrow ee$ background, so the overall value of f_z^w is used for each of the cryostats; the value of $f_z^{w'}$ (measured as a fraction of the number of signal events instead of as a fraction of the estimated number of true W bosons) differs slightly for the two cryostats since the total background is different (see text).

As a consistency check, $\sigma \cdot Br(p\bar{p} \rightarrow W \rightarrow e\nu)$ can be calculated separately for the CC and the EC:

$$\text{CC : } \sigma \cdot Br(p\bar{p} \rightarrow W \rightarrow e\nu) = 2.37 \pm 0.03 \pm 0.06 \text{ nb} \quad (6.7)$$

$$\text{EC : } \sigma \cdot Br(p\bar{p} \rightarrow W \rightarrow e\nu) = 2.34 \pm 0.05 \pm 0.11 \text{ nb} \quad (6.8)$$

where the first errors are statistical and the second are the uncorrelated systematic errors; errors from the common luminosity, acceptance and Level-0 efficiency measurements have been dropped, since they do not affect the comparison. The agreement is excellent, which adds confidence that the quantities measured for the separate cryostats are correct.

6.1.2 Calculation of $\sigma \cdot Br(p\bar{p} \rightarrow Z \rightarrow ee)$

The following equation is used to calculate the $Z \rightarrow ee$ cross section times branching ratio:

$$\sigma \cdot Br(p\bar{p} \rightarrow Z \rightarrow ee) \cdot (1 + f_{d-y}^z) = \frac{N_{sig}^z \cdot (1 - f_{qcd}^z)}{\mathcal{A}_z \cdot \varepsilon_z \cdot \int \mathcal{L} dt} \quad (6.9)$$

where f_{d-y}^z and f_{qcd}^z are the Drell-Yan and QCD di-jet background fractions respectively, N_{sig}^z is the number of candidate $Z \rightarrow ee$ events, and ε_z , \mathcal{A}_z and $\int \mathcal{L} dt$ are the overall selection efficiency, acceptance and integrated luminosity respectively.

Once again, the overall background as well as the Drell-Yan background can be expressed as a fraction of the number of candidate events N_{sig}^z :

$$f_{bkg}^z = 1 - \frac{1 - f_{qcd}^z}{1 + f_{d-y}^z} = f_{qcd}^z + f_{d-y}^{z'} \quad (6.10)$$

$$f_{d-y}^{z'} = f_{d-y}^z (1 - f_{bkg}^z) = f_{d-y}^z \cdot \frac{1 - f_{qcd}^z}{1 + f_{d-y}^z} \quad (6.11)$$

Using the combined background fraction f_{bkg}^z , the cross section can be expressed as:

$$\sigma \cdot Br(p\bar{p} \rightarrow Z \rightarrow ee) = \frac{N_{sig}^z \cdot (1 - f_{bkg}^z)}{\mathcal{A}_z \cdot \varepsilon_z \cdot \int \mathcal{L} dt} \quad (6.12)$$

The quantities needed for the calculation of the $Z \rightarrow ee$ cross section times branching ratio are summarized in Table 6.2. The $Z \rightarrow ee$ cross section times branching ratio based on the entire data set is

$$\sigma \cdot Br(p\bar{p} \rightarrow Z \rightarrow ee) = 0.218 \pm 0.008 \text{ (stat)} \pm 0.008 \text{ (syst)} \pm 0.012 \text{ (lum) nb.} \quad (6.13)$$

The error due to the luminosity uncertainty is dominant, although not so strongly as for the W cross section. Also, due to the limited statistics in the signal sample, the statistical error is comparable to the systematic error.

As a consistency check, the cross section times branching ratio can be calculated separately for each cryostat combination:

	CC-CC	CC-EC	EC-EC	Total
N_{sig}^z	402	296	77	775
Backgrounds(% of N_{sig}^z):				
QCD Multijet (f_{qcd}^z)	2.80 ± 1.40			
Drell-Yan ($f_{d-y}^{z'}$)	1.25 ± 0.10			
Total (f_{bkg}^z)	4.05 ± 1.39			
Acceptance \mathcal{A}_z (%)	17.97 ± 0.26	14.71 ± 0.18	3.63 ± 0.15	36.31 ± 0.36
Efficiency ε_z (%)	73.8 ± 2.2	73.4 ± 2.3	72.9 ± 4.3	73.6 ± 2.4
$\int \mathcal{L} dt$ (pb^{-1})	12.76 ± 0.68			

Table 6.2: Summary of quantities needed to calculate $Z \rightarrow ee$ cross section. Note that due to lack of statistics, there are no separate background measurements for the different cryostat combinations.

$$\text{CC} - \text{CC} : \sigma \cdot Br(p\bar{p} \rightarrow Z \rightarrow ee) = 0.228 \pm 0.012 \text{ nb} \quad (6.14)$$

$$\text{CC} - \text{EC} : \sigma \cdot Br(p\bar{p} \rightarrow Z \rightarrow ee) = 0.206 \pm 0.012 \text{ nb} \quad (6.15)$$

$$\text{EC} - \text{EC} : \sigma \cdot Br(p\bar{p} \rightarrow Z \rightarrow ee) = 0.219 \pm 0.025 \text{ nb.} \quad (6.16)$$

Only the statistical errors are shown; the systematic and luminosity are taken to be fully correlated and have been omitted since they do not affect the comparison. This is not entirely true for the systematic errors from the selection efficiencies; however, due to the CC-EC events in the sample, there is no part of the selection efficiency for any one of the three cross section calculations that is wholly uncorrelated with the efficiencies used for both of the other values. The agreement is good, although not quite as good as the W case. One possible source of disagreement comes from the use of the same background fractions for all three fiducial samples. In any case, there is no indication that the measured efficiencies and acceptances are inconsistent.

6.1.3 Statistical Error Calculation

Two comments need to be made about the calculation of the statistical error for the cross sections. First, the statistical error only contains the error due to the statistical variation of the signal sample; the statistical errors involved in determining the efficiencies and backgrounds are included in the systematic error.

Next, the effect of the various backgrounds on the statistical error must be handled with care. The basic question is whether the statistical error on N_{sig} is reduced by the background fraction f_{bkg} . The statistical error on N_{sig} alone is $\sqrt{N_{sig}}$; consider the numerator in the expression for the cross section (Equation 6.5 or Equation 6.12), which gives the predicted number of real W or Z events in the sample (note that the symbol δ is being used here to denote the error, in order to avoid confusion with the symbol σ used to represent the cross section):

$$N_w \text{ or } N_z = (N_{sig} \pm \sqrt{N_{sig}}) \cdot [(1 - f_{bkg}) \pm \delta_{bkg}] \quad (6.17)$$

If this expression is taken purely at face value, the resultant error due to the statistical variation of N_{sig} would be $\sqrt{N_{sig}} \cdot (1 - f_{bkg})$. This naïve approach ignores the fact that the statistical error depends on how the background is calculated; sometimes it is incorrect to reduce the absolute statistical error by the background fraction. In general, background calculations can be assigned to three different classes [90]:

- **Class I:** The background is determined internally, from the signal sample itself. In this case, statistical fluctuations of the number of background events affects the measured background fraction itself, and thus are included in the error on the background fraction, δ_{bkg} . In this case, the statistical error is reduced by the background fraction:

$$\delta_{stat}(I) = \sqrt{N_{sig}} \cdot (1 - f_{bkg}) \quad (6.18)$$

The relative error is $\sqrt{N_{sig}}/N_{sig}$.

- **Class II:** The background is determined externally, based on an independent data sample (possibly Monte Carlo), and subtracted as an absolute instead of a relative contribution:

$$N_w \text{ or } N_z = N_{sig} - N_{bkg} \quad (6.19)$$

In this case, N_{bkg}/N_{sig} represents the expected average background fraction \bar{f}_{bkg} determined from the external set of events. The statistical fluctuations of N_{bkg} within the candidate sample do not manifest themselves in the error on the measured background fraction, and must be included in the overall statistical error. In this case, the overall statistical error is not reduced by the background fraction:

$$\delta_{stat}(\text{II}) = \sqrt{N_{sig}} \quad (6.20)$$

The relative error in this case is $\sqrt{N_{sig}}/[N_{sig} \cdot (1 - f_{bkg})]$.

- **Class III:** The background fraction is determined externally as a fraction of the total signal. This can be a problem, in that it assumes knowledge of what is being measured in the first place, so care must be taken to avoid cheating. There are cases for which this case is valid, however; for example, if the $W \rightarrow \tau\nu$ and $\tau \rightarrow e\nu$ branching ratios are known independently, then the $W \rightarrow \tau\nu$ background in the $W \rightarrow e\nu$ sample falls into this category. In this case, the statistical error is reduced by the background fraction as in Class I (see Equation 6.18), and the relative error is once again $\sqrt{N_{sig}}/N_{sig}$.

In order to properly handle the statistical error, it is necessary to categorize each of the backgrounds into the three possible cases. This can be somewhat difficult, since few of the backgrounds can be cleanly assigned to one category; most involve elements of more than one case. For this analysis, a conservative approach is taken: all backgrounds are assigned to Class II, which gives the largest error, except for those backgrounds which are clearly either purely Class I or Class III.

For the case of the $W \rightarrow e\nu$ backgrounds, all the backgrounds are taken to be Class II, except for the $W \rightarrow \tau\nu$ background, which clearly falls into Class III. The

absolute statistical error on the predicted number of true $W \rightarrow e\nu$ events is then

$$\delta_{stat}(N_w) = \sqrt{N_{sig}^w} \cdot (1 - f_{\tau}^{w'}) \quad (6.21)$$

and the relative error is

$$\frac{\delta_{stat}(N_w)}{N_w} = \frac{\sqrt{N_{sig}^w}}{N_{sig}^w} \cdot \frac{(1 - f_{\tau}^{w'})}{(1 - f_{bkg}^w)} \quad (6.22)$$

For the $Z \rightarrow ee$ cross section, the QCD di-jet background is taken to be Class I, while the Drell-Yan background is considered Class II. The absolute statistical error and the relative error are then

$$\delta_{stat}(N_z) = \sqrt{N_{sig}^z} \cdot (1 - f_{qcd}^z) \quad (6.23)$$

$$\frac{\delta_{stat}(N_z)}{N_z} = \frac{\sqrt{N_{sig}^z}}{N_{sig}^z} \cdot \frac{(1 - f_{qcd}^z)}{(1 - f_{bkg}^z)} \quad (6.24)$$

For this analysis, due to the relatively small amount of background in the samples, there is little difference between calculating the statistical error properly and just taking the naïve approach presented above. The maximum difference in the relative error between taking the naïve approach and using the most conservative method (Class II for all backgrounds) is given by the total background fraction, around 5%. The statistical errors for the cross section measurements are in general small, and in any case are not the dominant error, so the details of the statistical error calculation have no real impact on the overall measurement. Nevertheless, the calculation should be done as correctly as possible.

6.2 Theoretical Calculations

The W and Z boson production cross sections have been calculated using code from Hamberg, Matsuura and Van Neerven [31], which does a complete calculation up to $\mathcal{O}(\alpha_s^2)$. The following values were used for the Standard Model parameters:

$$M_Z = 91.190 \text{ GeV} \quad (6.25)$$

$$M_W = 80.23 \text{ GeV} \quad (6.26)$$

$$\sin^2 \theta_W = 1 - \frac{M_W^2}{M_Z^2} = 0.2259 \quad (6.27)$$

where M_Z comes from LEP measurements [33] and M_W is based on an average of UA2, CDF and DØ data [34].

The calculation was performed for several different parton distribution functions (PDF's), in order to measure the variation of the cross section with PDF choice. The PDF's considered are from the CTEQ and MRS collaborations, using PDFLIB version 5.02 [67]. The CTEQ sets [30] incorporate the high statistics measurement of the structure function $F_2(x, Q^2)$ from the 1993 HERA run [91]. The MRSD0', MRSD'- and MRSS0' sets [69] are based on a global analysis prior to the availability of the HERA data, and the MRSH set is based on the F_2 measurement from the 1992 HERA run [92]. Finally, the most recent MRSA set incorporates the high statistics HERA F_2 measurement, as well as the NA51 Collaboration's measurement of the asymmetry in Drell-Yan production in pp and pn collisions [93] and the measurement of the asymmetry of the W^\pm rapidity distributions by the CDF collaboration [94]. The W and Z boson production cross sections for all the PDF's are summarized in Table 6.3. More information on the selected PDF's can be found in DØ Note 2733 [95].

The reference set for comparison with experiment is taken to be CTEQ2M. The error on the production cross section due to PDF variation is taken to be given by the extreme cross section values obtained with the chosen set of PDF's; the upper extreme is obtained using CTEQ2ML, while the lower extreme is obtained with CTEQ2MS. The errors due to PDF variation are summarized in Table 6.6, along with all the other error sources for the predicted cross section.

Until recently, the error on the theoretically calculated cross sections was so dominated by the variation due to PDF choice that other error sources could be ignored;

PDF(group,set)	σ_W (nb)	σ_Z (nb)	σ_W/σ_Z
MRSS0' (3,29)	22.11	6.63	3.334
MRSD0' (3,30)	22.15	6.68	3.316
MRSD'- (3,31)	21.81	6.56	3.326
MRSH (3,35)	22.04	6.59	3.343
MRSA (3,37)	22.05	6.65	3.316
CTEQ2M (4,24)	22.35	6.71	3.332
CTEQ2MS (4,25)	21.66	6.54	3.312
CTEQ2MF (4,26)	22.59	6.79	3.328
CTEQ2ML (4,27)	23.36	6.96	3.354

Table 6.3: Calculations of the W and Z boson production cross sections and their ratio for several PDF's. All sets are in the $\overline{\text{MS}}$ renormalization scheme. The group and set number given for each PDF identify the set within PDFLIB.

with the improved measurements of the F_2 structure function and the W^\pm asymmetries, the choice of acceptable PDF's has been reduced to the point that other sources of error must be considered. The additional sources of error considered here are the use of next-to-leading order (NLO) PDF's instead of NNLO (which would be appropriate to use in conjunction with the $\mathcal{O}(\alpha_s^2)$ calculation), variation of σ_W and σ_Z due to M_W variation, and finally the uncertainty due to the variation of the renormalization and factorization scales.

While the W and Z boson total production cross sections have been calculated up to $\mathcal{O}(\alpha_s^2)$, the corresponding NNLO PDF's are not yet available. The error on the calculated cross sections due to the use of NLO PDF's has been estimated [96] to be 3% at $\sqrt{s} = 1.8$ TeV.

The error on the measured W boson mass leads to an uncertainty in the value of the W cross section, and to a lesser extent the Z cross section, since $\sin^2 \theta_W$ is varied in conjunction with M_W . The variation on the individual cross sections is small compared to the variation due to PDF choice. The effect of the M_W uncertainty is shown in Table 6.4.

M_W (GeV)	σ_W (nb)	σ_Z (nb)	σ_W/σ_Z
80.05	22.40	6.67	3.358
80.23	22.35	6.71	3.332
80.41	22.30	6.75	3.306

Table 6.4: Calculations of W and Z boson production cross sections and their ratio for values of M_W one standard deviation below and above the world average, using the CTEQ2M PDF.

Scale	σ_W (nb)	σ_Z (nb)	σ_W/σ_Z
$M_V/2$	22.26	6.69	3.328
M_V	22.35	6.71	3.332
$2M_V$	22.42	6.72	3.339

Table 6.5: Calculations of W and Z production cross sections and their ratio for different values of the factorization and renormalization scales. The two scales are taken to be equal and the nominal value of M_W is used; M_V is the mass of the corresponding vector boson. The CTEQ2M PDF is used.

The last error source considered is the variation of the cross sections with factorization and renormalization scales. It is customary to set both scales equal [96]; for the calculation of the cross sections, both scales are set equal to the corresponding boson mass. The variation due to scale variation is estimated by varying the scales by a factor of two in either direction. The effect is shown in Table 6.5; it is small for the individual cross sections.

The effect on the calculated cross sections due to all of the sources of error considered are summarized in Table 6.6. Using CTEQ2M for the central values, the theoretical predictions for the production cross sections and their ratio at $\sqrt{s} = 1.8$ TeV are:

Error Source	$\delta\sigma_W$ (nb)	$\delta\sigma_Z$ (nb)	$\delta(\sigma_W/\sigma_Z)$
PDF Choice	+1.01, -0.69	+0.26, -0.17	+0.022, -0.020
NLO pdf's	$\pm 3\%$ (± 0.67 nb)	$\pm 3\%$ (± 0.20 nb)	± 0.000
M_W	± 0.05	± 0.03	± 0.026
Scale	+0.07, -0.09	+0.017, -0.02	+0.007, -0.004
Total Error	+1.21, -0.97	+0.33, -0.27	+0.034, -0.033

Table 6.6: Summary of estimated errors on the calculated W and Z boson production cross sections and their ratio. The separate errors are added to form a total error assuming no correlation between error sources.

$$\sigma_W \equiv \sigma(\bar{p}p \rightarrow W + X) = 22.4^{+1.2}_{-1.0} \text{ nb} \quad (6.28)$$

$$\sigma_Z \equiv \sigma(\bar{p}p \rightarrow Z + X) = 6.71^{+0.33}_{-0.27} \text{ nb} \quad (6.29)$$

$$\sigma_W/\sigma_Z = 3.33 \pm 0.03 \quad (6.30)$$

In order to compare these theoretical calculations to the experimental measurements, it is necessary to multiply the production cross sections by the appropriate electronic branching ratio. Assuming lepton universality, the precise values that are available for both the W and Z leptonic branching ratios can be used. For the W boson, a higher-order theory calculation [32] gives $Br(W \rightarrow \ell\nu) = 10.84 \pm 0.02\%$. For the Z boson, precise LEP measurements [33] give $Br(Z \rightarrow \ell\ell) = 3.367 \pm 0.006\%$. Applying these branching ratios to the production cross section results give:

$$\sigma_W \cdot Br(W \rightarrow \ell\nu) = 2.42^{+0.13}_{-0.11} \text{ nb} \quad (6.31)$$

$$\sigma_Z \cdot Br(Z \rightarrow \ell\ell) = 0.226^{+0.011}_{-0.009} \text{ nb} \quad (6.32)$$

This prediction is compared to the most recent data at $\sqrt{s} = 1.8$ TeV in Figure 6.1; the results of the current analysis are the left-most points. In Figure 6.2, the W and Z cross sections times branching ratios are plotted as a function of \sqrt{s} , along with the most recent measurements by the CERN SPS and Fermilab Tevatron experiments.

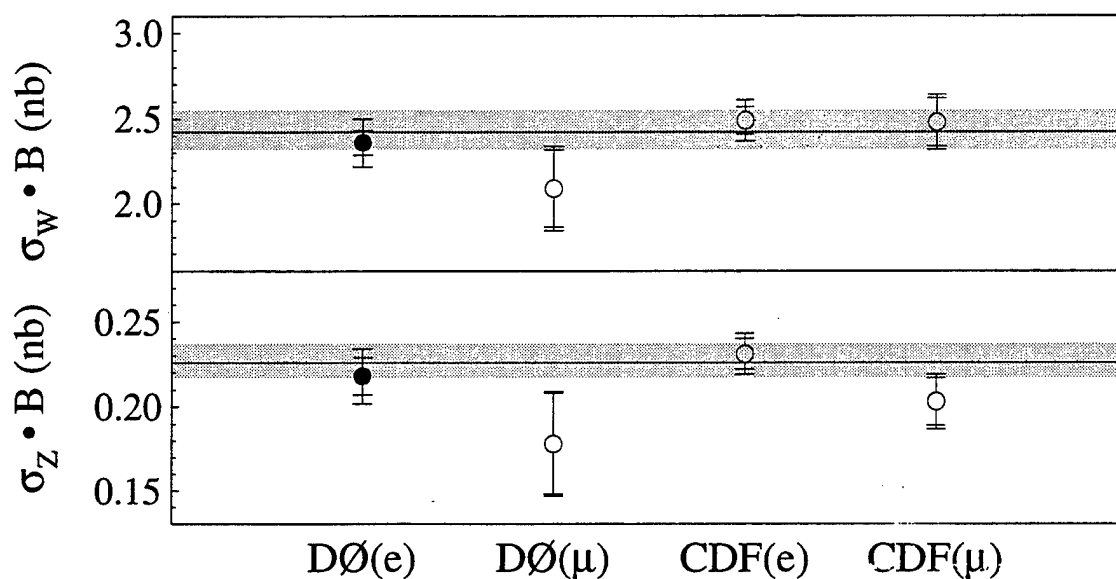


Figure 6.1: Plot of cross section times branching ratio for inclusive W and Z boson production at $\sqrt{s} = 1.8$ TeV. The solid line gives the central value of the theory prediction, and the shaded region indicates the associated error, as described in the text. The left-most points (filled circles) show the results of this analysis; the hollow circles show the most recent results of other Tevatron W and Z boson cross section measurements [97]. The outermost error bars give the total error; the inner tick marks exclude the error due to the luminosity.

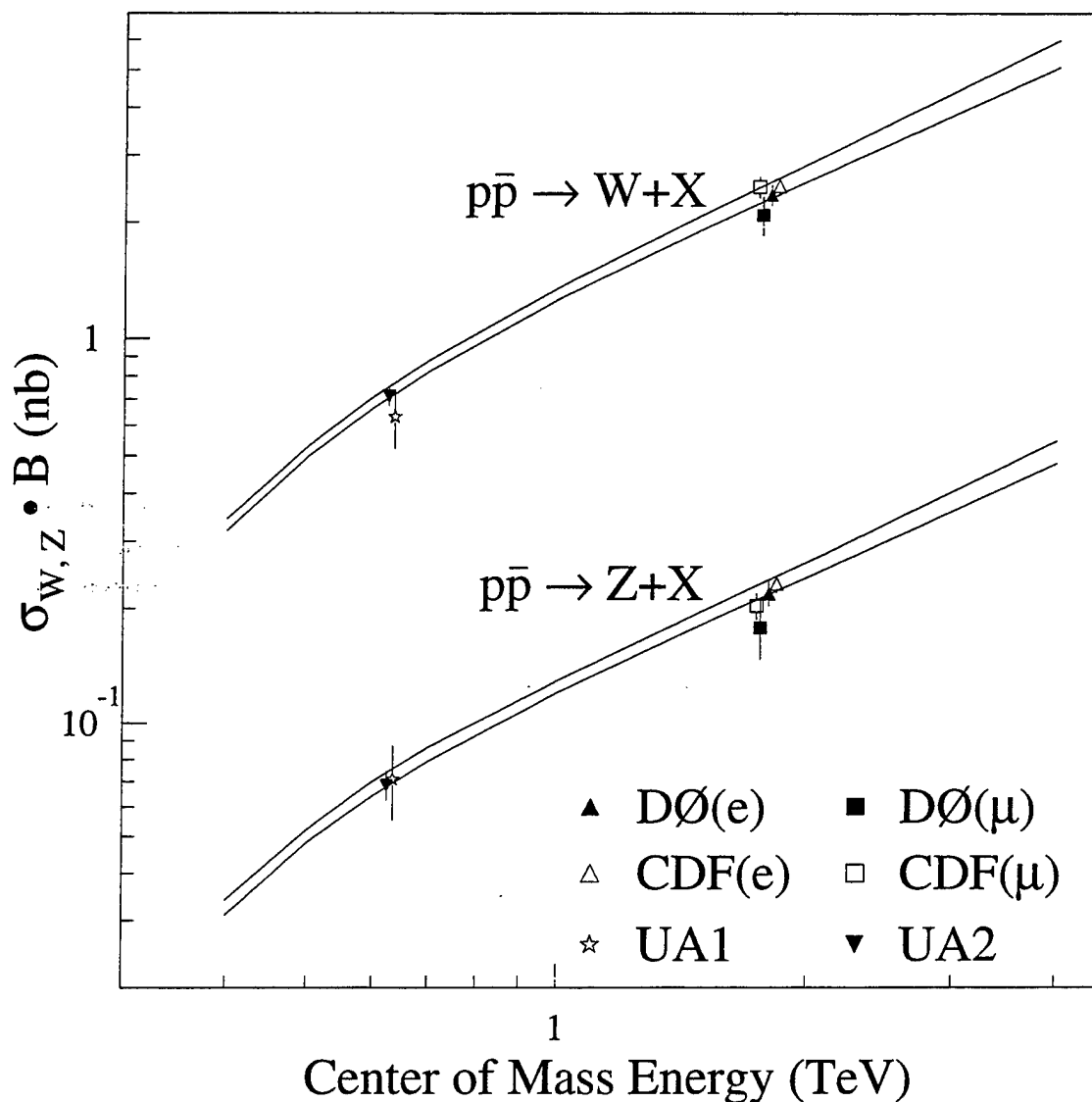


Figure 6.2: Plot of the predicted cross section times branching ratio for inclusive W and Z boson production versus \sqrt{s} (bands), along with the most recent measurements (points) [98][99] [97]. The width of the bands include contributions from PDF and scale variation. Note that the UA2 cross sections have been increased by 4.2% to reflect a change from $\rho = 0.24$ to $\rho = 0.15$ [99].

6.3 Cross Section Ratio

Since the W and Z cross sections are measured with the same data sample, the dominant luminosity error cancels in the ratio. The cross section ratio R is defined as follows:

$$R \equiv \frac{\sigma_w \cdot Br(W \rightarrow e\nu)}{\sigma_z \cdot Br(Z \rightarrow ee)} = \frac{N_w}{N_z} \cdot \frac{\mathcal{A}_z}{\mathcal{A}_w} \cdot \frac{\varepsilon_z}{\varepsilon_w} \quad (6.33)$$

where N_w and N_z are the estimated number of true W and Z bosons with the background removed, and the luminosity cancels completely, by construction. The values necessary to calculate R are summarized in Table 6.7; the result for the electron channel is

$$R = 10.82 \pm 0.41 \text{ (stat)} \pm 0.30 \text{ (syst)}. \quad (6.34)$$

where the statistical error is dominated by the size of the Z boson sample, and the systematic error includes contributions from the background, efficiency and acceptance measurements, but no luminosity error.

The ratio can be used to make an indirect measurement of $\Gamma(W)$, the total decay width of the W boson:

$$\Gamma(W) = \frac{\sigma_w}{\sigma_z} \cdot \frac{\Gamma(W \rightarrow e\nu)}{Br(Z \rightarrow ee)} \cdot \frac{1}{R}. \quad (6.35)$$

Alternatively, the branching ratio $Br(W \rightarrow e\nu)$ can be calculated. The production cross section ratio is taken from the theory calculation described above, using CTEQ2M for the central value; this gives $\sigma_w/\sigma_z = 3.33 \pm 0.03$ including all error sources. Using $Br(Z \rightarrow \ell\ell) = 3.367 \pm 0.006\%$ as given above and $\Gamma(W \rightarrow \ell\nu) = 0.2252 \pm 0.0015$ GeV based on a detailed higher order theoretical calculation [32], the full W boson width is calculated to be

$$\Gamma(W) = 2.06 \pm 0.08 \text{ (stat)} \pm 0.06 \text{ (syst)} \pm 0.01 \text{ (external)} \quad (6.36)$$

where the final error includes all contributions from the external inputs used to calculate $\Gamma(W)$ from R ; note that an anti-correlation of the variation due to δM_w between σ_w/σ_z and $\Gamma(W \rightarrow \ell\nu)$ has been taken into account, which reduces the error due to the external inputs significantly. This result is discussed in more detail elsewhere [76].

Input	Value
N_w	9754 ± 100 (stat) ± 57 (bkg syst)
N_z	744 ± 27 (stat) ± 11 (bkg syst)
$\mathcal{A}_z/\mathcal{A}_w$	0.789 ± 0.010
$\varepsilon_z/\varepsilon_w$	1.045 ± 0.019

Table 6.7: Summary of inputs used to calculate the cross section ratio R .

6.4 Conclusions

As can be seen from Figure 6.1, the agreement between theory and experiment is excellent. The total experimental errors are comparable to the errors on the theory calculations, especially if only the statistical and non-luminosity systematic errors are considered.

The W and Z leptonic branching ratios are well known, so these measurements can potentially shed some light upon the $p\bar{p} \rightarrow W$ and $p\bar{p} \rightarrow Z$ production rates at $\sqrt{s} = 1.8$ TeV. The main uncertainty in the theory calculation comes from the uncertainty in the PDF's; if the cross section measurement is sufficiently precise, then the number of acceptable PDF choices can be reduced. Unfortunately, even if the luminosity error is ignored or significantly reduced, the errors on the current measurement are too large to discount any of the PDF choices considered. However, the good agreement between theory and experiment does add confidence that the set of PDF's used for the theory calculation is reasonable. With the larger data set from Tevatron Run 1B, the statistical and non-luminosity systematic errors will be reduced significantly (see Section 6.5); if the luminosity error can be reduced as well, it should be possible to reduce the number of satisfactory PDF's.

Unfortunately, the prospects for the improvement of the luminosity measurement are unknown, especially since the measurement gets more and more difficult as the instantaneous luminosity increases. With higher luminosity, a larger fraction of cross-

ings contain multiple interactions, and a larger correction must be applied to the luminosity measured by the Level- \emptyset scalers, which register only once per crossing. Some progress has been made towards using more of the information from the individual Level- \emptyset counters so that a smaller correction is necessary, and there is less of a saturation problem [100]. However, the situation will always be worse at the high luminosities typical of Run 1B compared to the relatively low luminosity running during Run 1A, where the majority of the crossings contained one or even zero events.

One solution that has been proposed to handle the determination of the integrated luminosity when there are typically several interaction vertices in each crossing is to use the number of observed $W \rightarrow e\nu$ events. That is, if $\sigma \cdot Br(p\bar{p} \rightarrow W \rightarrow e\nu)$ is known to some precision, then Equation 6.5 can be inverted to give the integrated luminosity:

$$\int \mathcal{L} dt = \frac{N_{sig}^w \cdot (1 - f_{bkg}^w)}{\mathcal{A}_w \cdot \varepsilon_w \cdot [\sigma \cdot Br(p\bar{p} \rightarrow W \rightarrow e\nu)]} \quad (6.37)$$

This approach has some benefits, and several difficulties. No correction would be necessary for multiple interaction crossings, since each interaction in the crossing has a chance of producing a $W \rightarrow e\nu$ event, and the likelihood of multiple W events in the same crossing is negligible. Furthermore, it would be possible to calculate the integrated luminosity for triggers that do not require Level- \emptyset to fire, allowing study of diffractive physics, which is largely excluded by a Level- \emptyset requirement. Perhaps the largest benefit of using the number of $W \rightarrow e\nu$ events as a luminosity monitor is that data from different experiments can be easily compared or combined, without having to worry about the differences between the Level- \emptyset -type systems of the different experiments; of course, the systematics in measuring efficiencies, backgrounds and acceptances still exist, but they are unavoidable, and are (at least for the case of D \emptyset) smaller than the luminosity error. For example, for a combined D \emptyset and CDF $t\bar{t}$ cross section measurement, it would be advantageous to use the observed $W \rightarrow e\nu$ cross sections to provide the normalization between the measured integrated luminosities

of the two experiments.

However, there are serious difficulties associated with using W events as a luminosity monitor. First of all, in order to get a reasonably accurate measurement, there must be a large enough sample of W 's to keep the statistical error down to the desired level. Furthermore, there is the very real probability that the backgrounds and efficiencies vary as a function of instantaneous luminosity, due to the extra minimum-bias events that accompany the signal W event for a multiple interaction crossing. It is in principle possible to measure the backgrounds and efficiencies as a function of instantaneous luminosity, as long as care is taken to use an independent measure of the luminosity so as to avoid a circular argument. A very large diagnostic sample would be required in order to have enough statistics in each luminosity bin to provide the desired measurement accuracy.

6.5 Future Prospects

Since the end of Tevatron Run 1A in May of 1993, roughly 100 pb^{-1} of additional collider data has been recorded during Tevatron Runs 1B and 1C. The measurement of the $W \rightarrow e\nu$ and $Z \rightarrow ee$ cross sections is in progress; due to the size of the data sample, the measurement errors will be reduced significantly compared to the current analysis based on Run 1A. Both the statistical and systematic errors will be reduced, due to the availability of a larger sample of diagnostic events. However, the increase in statistics is not without cost; due to the high luminosities typical of the later running, multiple interaction events become a serious problem, complicating the determination of the efficiencies, backgrounds and even the acceptance.

Estimates for the errors in the cross section measurement based on a 100 pb^{-1} data sample are shown in Table 6.8, compared with the errors of the current measurement; the luminosity errors are shown separately, since they are not expected to decrease. With the increase in statistics, the total non-luminosity error is expected to decrease by roughly a factor of two. Unfortunately, since the luminosity error is not expected

Error Source	$\delta(\sigma_w \cdot B)/\sigma_w \cdot B$ (%)		$\delta(\sigma_z \cdot B)/\sigma_z \cdot B$ (%)	
	Run 1A (12.8 pb ⁻¹)	Runs 1B/1C (100 pb ⁻¹)	Run 1A (12.8 pb ⁻¹)	Runs 1B/1C (100 pb ⁻¹)
Statistical	1.0	0.4	3.6	1.3
Efficiency	2.4	1.0	3.3	1.9
Background	0.6	0.3	1.4	1.0
Acceptance	1.3	1.1	1.0	0.9
Total Non-luminosity	3.0 %	1.6 %	5.2 %	2.7 %
Luminosity	5.4 %	5.4 %	5.4 %	5.4 %
Total	6.2 %	5.6 %	7.5 %	6.0 %

Table 6.8: Comparison of the relative errors on the current Run 1A cross section measurement compared with those expected for a 100 pb⁻¹ data sample, roughly the integrated luminosity recorded by DØ during Tevatron Runs 1B and 1C. The error due to the luminosity measurement is listed separately, since there is no foreseen reduction in that error, and also to underscore the fact that the luminosity uncertainty dominates the cross section error.

to change significantly for the high statistics measurement, the total cross section error will not decrease much.

For these estimates, the analysis is assumed to use the same selection criteria, so the statistical error is expected to decrease as $1/\sqrt{R_{lum}}$, where R_{lum} is the ratio of integrated luminosities. The bulk of the efficiency error is due to the size of the diagnostic $Z \rightarrow ee$ sample; that part of the efficiency error is scaled down by the same factor. The systematic error on the efficiency is assumed to stay the same, with small improvements in the background subtraction systematics expected to offset additional systematics coming from the high luminosity running. The background errors, dominated by the errors on the QCD di-jet background for both the W and Z cross sections, are also statistics-dominated, and are expected to decrease significantly for the larger data sample. Only small improvements are expected for the acceptance; these are unrelated to the size of the data sample, but depend on the improved knowledge of outside factors such as structure functions and the mass of the W

Error Source	$\delta R/R$ (%)	
	Run 1A (12.8 pb ⁻¹)	Runs 1B/1C (100 pb ⁻¹)
Statistical	3.8	1.4
Efficiency	1.9	0.9
Background	1.6	0.8
Acceptance	1.3	1.1
Total	4.7 %	2.1 %

Table 6.9: Comparison of the relative errors on the current Run 1A measurement of the cross section ratio R with those expected for a 100 pb⁻¹ data sample.

boson. These improvements in the knowledge of the acceptance may be counteracted somewhat by the effects of high luminosity running: the large fraction of multiple vertex events causes problems in determining the correct vertex for the W or Z event, which affects the determination of the transverse energy, and therefore can affect the kinematic acceptance.

Since the total error in the absolute cross sections is not expected to decrease significantly, the larger data sample will still not be able to favor a particular set of PDF's at $\sqrt{s} = 1.8$ TeV. However, measurements that do not involve the luminosity will improve significantly. The errors for the measurement of the cross section ratio R are shown in Table 6.9, along with the errors estimated for the 100 pb⁻¹ data sample. Since the luminosity error cancels in the ratio, the total experimental error in R decreases by more than a factor of two, to roughly 2%, which transfers directly to an error in the indirect measurement of $\Gamma(W)$. Note that the total error on the external quantities used to calculate $\Gamma(W)$ is 0.6%, which defines the practical limit on the accuracy of the indirect W width measurement.

The additional data would also of course improve the measurement of the integrated luminosity based on the number of W bosons, if a value for $\sigma_w \cdot Br(W \rightarrow e\nu)$ is assumed or measured elsewhere. The accurate determination of the W -based lumi-

osity would aid in combining results from different experiments. The primary future role of the measurement of the W boson cross section may be use as a luminosity monitor.

Bibliography

- [1] An introduction to Quantum Electrodynamics is given in a set of lectures by Richard Feynman, published in R. Feynman, **Quantum Electrodynamics: A Lecture Note and Reprint Volume**, W. A. Benjamin, Inc., New York, 1962. A good textbook presentation is given in I. J. Aitchison and A. J. Hey, **Gauge Theories in Particle Physics: a Practical Introduction**, Second Edition, Adam Hilger(IOP Publishing, Bristol, England), 1989.
- [2] P. A. M. Dirac, *Proc. R. Soc. London Ser. A* **114**, 243 (1927).
- [3] UA1 Collaboration: G. Arnison *et al.*, *Phys. Lett.* **B122**, 103 (1983). UA2 Collaboration: M. Banner *et al.*, *Phys. Lett.* **B122**, 322 (1983).
- [4] UA1 Collaboration: G. Arnison *et al.*, *Phys. Lett.* **B126**, 393 (1983). UA2 Collaboration: P. Bagnaia *et al.*, *Phys. Lett.* **B129**, 130 (1983).
- [5] C. Quigg, **Gauge Theories of the Strong, Weak, and Electromagnetic Interactions**, Benjamin/Cummings, Menlo Park, CA, 1983.
- [6] The historical material presented is loosely based on information from E. Commins and P. Bucksbaum, **Weak Interactions of leptons and quarks**, Cambridge University Press, 1982.
- [7] W. Pauli, *Proc. VII Solvay Congress, Brussels (1933)*, 324, Gauthier-Villars, Paris, 1933.

- [8] E. Fermi, *Z. Phys.* **88**, 161 (1934).
- [9] C. S. Wu, E. Ambler, R. W. Hayward, D. D. Hopper, and R. P. Hudson, *Phys. Rev.* **105**, 1413 (1957).
- [10] E. Noether, *Nachr. Kgl. Ges. Wiss. Göttingen*, 235 (1918).
- [11] S. L. Glashow, *Nucl. Phys.* **22**, 579 (1961).
- [12] A. Salam, *Nobel Symposium*, No. 8, 367, ed. N. Svartholm, Almquist and Wiksell, Stockholm, 1968.
- [13] S. Weinberg, *Phys. Rev. Lett.* **19**, 1264 (1967).
- [14] M. Gell-Mann, *Phys. Rev.* **92**, 833 (1953); T. Nakano and K. Nishijima, *Prog. Theor. Phys. (Kyoto)* **10**, 581 (1955).
- [15] F. J. Hasert *et al.*, *Phys. Lett.* **B46**, 121,138 (1973); *Nucl. Phys.* **B73**, 1 (1974).
- [16] A. Benvenuti *et al.*, *Phys. Rev. Lett.* **32**, 800 (1974).
- [17] N. Cabibbo, *Phys. Rev. Lett.* **10**, 531 (1963).
- [18] S. Glashow, J. Iliopoulos, and L. Maiani, *Phys. Rev.* **D2**, 1285 (1970).
- [19] J. Augustin *et al.*, *Phys. Rev. Lett.* **33**, 1406 (1974).
- [20] J. Aubert *et al.*, *Phys. Rev. Lett.* **33**, 1404 (1974).
- [21] G. 't'Hooft, *Nucl. Phys.* **B33**, 173 (1971); *Nucl. Phys.* **B35**, 167 (1971).
- [22] M. Perl *et al.*, *Phys. Rev. Lett.* **35**, 1489 (1975).
- [23] S. Herb *et al.*, *Phys. Rev. Lett.* **39**, 252 (1977); W. Innes *et al.*, *Phys. Rev. Lett.* **39**, 1240 (1977).
- [24] DØ Collaboration: S. Abachi *et al.*, *Phys. Rev. Lett.* **74**, 2632 (1995).

- [25] CDF Collaboration: F. Abe *et al.*, *Phys. Rev. Lett.* **74**, 2626 (1995).
- [26] M. Kobayashi and K. Maskawa, *Prog. Theor. Phys.* **49**, 652 (1973).
- [27] Original results on the number of generations (actually the number of light neutrinos) is reported in: ALEPH Collaboration: D. Decamp *et al.*, *Phys. Lett.* **B231**, 509 (1989); DELPHI Collaboration: P. Aarnio *et al.*, *Phys. Lett.* **B231**, 509 (1989); L3 Collaboration: B. Adeva *et al.*, *Phys. Lett.* **B231**, 509 (1989); OPAL Collaboration: M. Akrawy *et al.*, *Phys. Lett.* **B231**, 509 (1989). The most recent combined LEP results can be found in *The LEP Electroweak Working Group*, LEPEWWG/94-01.
- [28] An introduction to resummation in the context of calculating the W and Z boson transverse momentum spectra is given in: P. Arnold and R. Kauffman, *Nucl. Phys.* **B349**, 381 (1991).
- [29] The equations for W and Z boson production and decay are based upon those found in: V. Barger and R. Phillips, *Collider Physics*, Addison-Wesley Publishing Company, 1987; Chapter 8.
- [30] CTEQ Collaboration: J. Botts *et al.*, *Phys. Lett.* **B304**, 159 (1993); now superseded by CTEQ2p: J. Botts *et al.* (unpublished).
- [31] R. Hamberg, W. Van Neerven, and T. Matsuura, *Nucl. Phys.* **B359**, 343 (1991).
- [32] J. Rosner, M. Worah, and T. Takeuchi, *Phys. Rev.* **D49**, 1363 (1994).
- [33] Particle Data Group, L. Montanet *et al.*, *Phys. Rev.* **D50**, 1173 (1994).
- [34] This value for the W boson mass was obtained by combining UA2(1992) data, CDF (1990 and 1993/1994) data, and DØ(1993) data, as detailed in: M. Demarteau *et al.*, DØ Note 2115/CDF Note 2552, 1994 (unpublished).
- [35] DØ Collaboration: S. Abachi *et al.*, *Nucl. Instrum. Methods* **A338**, 185 (1994).

- [36] J. Thompson, FERMILAB-TM-1909 and DØ Note 2367, 1994.
- [37] F. Sauli, CERN Report 77-09 (1977). Reprinted in T. Ferbel, **Experimental Techniques in High Energy Physics**, Addison-Wesley Publishing Company, Inc., 1987.
- [38] A. Clark *et al.*, *Nucl. Instrum. Methods* **A261**, 420 (1987).
- [39] NiCoTin is an alloy made up of 38.8% CO, 19.3% Cr, 15.6% Ni, 13.3% Fe, and 11.4% Mo, manufactured by Microfil Industries SA, Switzerland.
- [40] A. Clark *et al.*, *Nucl. Instrum. Methods* **A315**, 193 (1992).
- [41] A. Clark *et al.*, *Nucl. Instrum. Methods* **A279**, 243 (1989). T. Behnke, Ph.D Thesis, State University of New York at Stonybrook, August 1989 (unpublished).
- [42] J. Thompson, Ph.D Thesis, State University of New York at Stonybrook, February 1994 (unpublished).
- [43] R. Avery *et al.*, *IEEE Trans. Nucl. Sci.* **NS-33**, 573 (1986).
- [44] S. Rajagopalan, Ph.D Thesis, Northwestern University, June 1992 (DØ Note 1433).
- [45] R. Yarema, *IEEE Trans. Nucl. Sci.* **NS-33**, 933 (1986).
- [46] M. Martin, M. Johnson, M. Mayberry, and D. DeGroot, *IEEE Trans. Nucl. Sci.* **NS-34**, 258 (1987).
- [47] D. DeGroot, DØ Note 1013, August 1990 (unpublished).
- [48] C. Fabjan, "Calorimetry in High-Energy Physics," printed in T. Ferbel, **Experimental Techniques in High Energy Physics**, Addison-Wesley Publishing Company, Inc., 1987.

- [49] DØ Collaboration: S. Abachi *et al.*, *Nucl. Instrum. Methods* **A324**, 53 (1993).
DØ Collaboration: H. Aihara *et al.*, *Nucl. Instrum. Methods* **A325**, 393 (1993).
- [50] J. Bantly *et al.*, *IEEE Trans. Nucl. Sci.* **NS-41**, 1274, (1994).
- [51] M. Abolins *et al.*, *IEEE Trans. Nucl. Sci.* **NS-36**, 384, (1989); M. Abolins *et al.*, *Nucl. Instrum. Methods* **A289**, 543 (1990).
- [52] Digital Equipment Corp., Maynard, MA 01754.
- [53] "DØ Software Documentation", ed. by Geoff Manning., DØ internal report, July, 1995.
- [54] M. Goosens *et al.*, CERN Library Program No. Q100 (Nov 1991).
- [55] C. Klopfenstein and M. Strovink, DØ Note 445, September, 1986; D. Schaile, O. Schaile, and J. Schwarz, *Nucl. Instrum. Methods* **A242**, 247 (1986).
- [56] Section 3.9.3 of Reference [53].
- [57] Section 3.10.17 of Reference [53].
- [58] Section 3.13.3 of Reference [53]; S. Youssef, DØ Note 375 (1986) and DØ Note 541 (1987).
- [59] Section 3.13.5 of Reference [53].
- [60] J. Womersley, DØ Note 2106, March, 1994.
- [61] U. Heintz, DØ Note 1758, June 1993.
- [62] Natalie Roe, private communication. A description of QCD_JET_CORRECTION can be found as part of a description of the general CAFIX correction program in Joffe-Minor and Astur, DØ Note 2211, July, 1994.

- [63] P. Arnold and R. Kauffman, *Nucl. Phys.* **B349**, 381 (1991); P. Arnold and M. Reno, *Nucl. Phys.* **B319**, 37 (1989).
- [64] Jie Yang, DØ Note 2317, September, 1994.
- [65] Q. ZHu, Ph.D Thesis, New York University, June 1994 (DØ Note 2160).
- [66] A. Mincer, DØ Note 2050, February 1994.
- [67] H. Plathow-Besch, *PDFLIB: Nucleon, Pion and Photon Parton Density Functions and α_s Calculations User's Manual*, CERN-PPE-1993.08.30. Distributed as DØ Note 1991.
- [68] C. Davies and W. Stirling, *Nucl. Phys.* **B244**, 337 (1984); C. Davies, B. Webber and W. Stirling, *Nucl. Phys.* **B256**, 413 (1985).
- [69] A. Martin, R. Roberts, and W. Stirling, *Phys. Lett.* **B306**, 145 (1993).
- [70] M. Gluck, E. Reya, and A. Vogt, *Z. Phys.* **C53**, 127 (1992).
- [71] Darien Wood, private communication.
- [72] Mike Kelly, private communication.
- [73] Jeff Bantly, private communication.
- [74] Natalie Roe, private communication.
- [75] Natalie Roe, DØ Note 2340, November, 1994.
- [76] Jie Yang, Ph.D thesis, New York University, May, 1995 (unpublished).
- [77] Jonckheere *et al.*, DØ Note 969a, May 1995; J. Womersley, FERMILAB-CONF-92-306 (also DØ Note 1520); F. Carminati *et al.*, *GEANT User's Guide*, CERN Program Library, December, 1991.
- [78] Geary Eppley, private communication.

- [79] J. Yang, DØ Note 2366, November, 1994.
- [80] Bob Madden, private communication.
- [81] T. Sjostrand, *PYTHIA 5.7 and JETSET 7.4 Physics and Manual*, CERN-TH-7112-93, February 1994.
- [82] F. Paige and S. Protopopescu, *ISAJET 5.20: A Monte Carlo Event Generator for pp and $\bar{p}p$ Interactions*, BNL-38034, March 1996.
- [83] J. Bantly *et al.*, Fermilab-TM-1930, April, 1995 (also available as DØ Note 2544).
- [84] N. Amos *et al.*, *Phys. Lett.* **B243**, 158 (1990).
- [85] CDF Collaboration: F. Abe *et al.*, *Phys. Rev.* **D50**, 5518, 5535, 5550 (1994).
- [86] CDF Collaboration: F. Abe *et al.*, *Phys. Rev.* **D50**, 5550 (1994), Appendix B.
- [87] P. Aurenche *et al.*, *Phys. Rev.* **D45**, 92 (1992); F. Bopp *et al.*, *Z. Phys.* **C51**, 99 (1991).
- [88] N. Amos *et al.*, DØ Note 2031, January, 1994.
- [89] Jerry Blazey, private communication.
- [90] Darien Wood, private communication.
- [91] H1 Collaboration: K. Müller, *Proc. of 29th Rencontre de Moriond*, March, 1994.
ZEUS Collaboration: G. Wolf, *Proc. of International Workshop on Deep Inelastic Scattering, Eilat, Israel*, February, 1994; M. Roco, *Proc. of 29th Rencontre de Moriond*, March, 1994.
- [92] H1 Collaboration: I. Abt *et al.*, *Nucl. Phys.* **B407**, 515 (1993); ZEUS Collaboration: M. Derrick *et al.*, *Phys. Lett.* **B316**, 412 (1993).
- [93] NA51 Collaboration: A. Baldit *et al.*, *Phys. Lett.* **B332**, 244 (1994).

- [94] CDF Collaboration: A. Bodek, *Proc. of International Workshop on Deep Inelastic Scattering, Eilat, Israel*, February, 1994.
- [95] P. Grudberg, S. Lami, and D. Wood, DØ Note 2733, July, 1995.
- [96] W. Van Neerven and E. Zijlstra, *Nucl. Phys.* **B382**, 11 (1992).
- [97] CDF Collaboration: F. Abe *et al.*, *Phys. Rev.* **D44**, 29 (1991); CDF Collaboration: F. Abe *et al.*, *Phys. Rev. Lett.* **69**, 28 (1992).
- [98] UA1 Collaboration: C. Albajar *et al.*, *Phys. Lett.* **B198**, 271 (1987).
- [99] UA2 Collaboration: J. Alitti *et al.*, *Phys. Lett.* **B276**, 365 (1992).
- [100] Jeff Bantly, private communication.

M98052836



Report Number (14) LBNL--40763

Publ. Date (11) 1997 01

Sponsor Code (18) DOE/ER, XF

JC Category (19) UC-414, DOE/ER

DOE